

Strukturelle Dynamik von photosensitiven Proteinen

Inaugural-Dissertation

zur

Erlangung des Doktorgrades der
Mathematisch-Naturwissenschaftlichen Fakultät
der Heinrich-Heine-Universität Düsseldorf

vorgelegt von

Friedrich Schotte

aus Köln

Jülich

2000

Gedruckt mit Genehmigung der Mathematisch-Naturwissenschaftlichen Fakultät der
Heinrich-Heine-Universität Düsseldorf

Referent: Prof. Dr. Georg Büldt
Koreferenten: Prof. Dr. Ronald Frahm
Dr. Michael Wulff

Tag der mündlichen Prüfung: 12. Juli 2000

Contents

| | | |
|----------|--|-----------|
| 1 | Summary..... | 5 |
| 2 | Introduction..... | 7 |
| 3 | Photoactive Proteins..... | 8 |
| 3.1 | Myoglobin | 8 |
| 3.2 | Photoactive Yellow Protein | 12 |
| 3.3 | Bacteriorhodopsin..... | 17 |
| 4 | Laboratory and Experimental Apparatus..... | 21 |
| 4.1 | The ESRF..... | 21 |
| 4.2 | The ID9 Beamline | 25 |
| 4.3 | X-ray Sources..... | 27 |
| 3.4 | X-ray Optics | 31 |
| 4.4 | X-ray Chopper..... | 40 |
| 4.5 | X-ray Image Intensifier..... | 48 |
| 4.6 | Femtosecond Laser System..... | 52 |
| 5 | Experiments and Results..... | 54 |
| 5.1 | Instrumentation..... | 54 |
| 5.1.1 | On-line Microspectrometer | 54 |
| 5.1.2 | Femtosecond Spectrometer for Single Crystals | 57 |
| 5.1.3 | Laser to X-ray Timing Electronics | 63 |
| 5.2 | Experiments on Photosensitive Proteins..... | 71 |
| 5.2.1 | Myoglobin | 71 |
| 5.2.2 | Photoactive Yellow Protein..... | 81 |
| 5.2.3 | Bacteriorhodopsin Purple Membrane | 85 |
| 6 | Discussion..... | 96 |
| 6.1 | Instrumentation..... | 96 |
| 6.2 | Experiments on Photosensitive Proteins..... | 96 |
| 6.2.1 | Myoglobin | 96 |
| 6.2.2 | Photoactive Yellow Protein..... | 97 |
| 6.2.3 | Bacteriorhodopsin | 100 |

| | | |
|-----------|---------------------------------------|------------|
| 7 | Outlook | 101 |
| 7.1 | Future Experiments..... | 101 |
| 7.2 | X-ray Free Electron Lasers | 101 |
| 8 | Acknowledgements | 103 |
| 9 | Appendix..... | 105 |
| 9.1 | Calorimetric Power Measurements | 105 |
| 9.2 | Glossary | 107 |
| 9.3 | List of publications | 109 |
| 9.4 | Conference Contributions | 111 |
| 10 | Index..... | 112 |
| 11 | References | 114 |

Zusammenfassung

Die vorgelegte Dissertation beschreibt die Anwendung von intensiver, gepulster Röntgenstrahlung eines Synchrotrons zur Untersuchung biochemischer Reaktionen, die durch Licht ausgelöst werden. Die Arbeit enthält Beiträge zur Instrumentation einer Beamline und Experimente an den Proteinen Myoglobin, Photoactive Yellow Protein (PYP) und Bacteriorhodopsin.

Die instrumentelle Arbeit führte zu einer Verbesserung der Zeitauflösung für gepulste Laue-Beugungsexperimente von 10 ns auf 100 ps. Mein Beitrag bestand in der Integration von drei wesentlichen neuen Komponenten, einem Femtosekunden-Lasersystem, einem schnellen Röntgen-Chopper und einem Wärmelast-Shutter in die Beamline. Für Pump-Prob-Experimente mit Laser- und Röntgenstrahl erlaubt die Apparatur die Zeitverzögerung computergesteuert mit Picosekunden-Präzision einzustellen. Zum Nachweis der Lichtanregung der Proben habe ich ein mikrosekunden-zeitaufgelöstes Spektrometer mit Mikrofokussierung gebaut, das den Anregungsgrad der Probe vor dem Experiment und in-situ messen kann. Im Rahmen einer externen Kollaboration habe ich ein femtosekunden-zeitaufgelöstes Spektrometer aufgebaut. Es wurde gebaut, um die Frage zu beantworten, ob Proteinkristalle mit fokussierten Femtosekunden-Laserpulsen angeregt werden können, ohne Schaden zu nehmen, und die optimalen Anregungsbedingungen dafür herauszufinden.

Die Laseranregungs-Studien haben im Fall von Myoglobin gezeigt, daß ein Proteinkristall mit Femtosekunden-Laserpulsen angeregt werden kann, ohne die kristalline Ordnung zu stören oder irreversible photochemische Veränderungen zu bewirken. Laue-Beugungsexperimente mit 100 ps Zeitauflösung an CO-beladenen Myoglobin zeigen strukturelle Dynamik, die mit früheren Nanosekunden-Messungen übereinstimmt, allerdings keinen klaren Hinweis gibt auf die Lage des CO-Moleküls nach der Photodissoziation. An PYP zeigt ein nanosekunden-zeitaufgelöstes Laue-Experiment ein frühes Intermediat des Photozyklus mit einem photoisomerisierten Chromophor aber wenig strukturellen Änderung im Protein. Laue-Beugungs-Experimente an PYP mit 100 ps Zeitauflösung wurden technisch erfolgreich durchgeführt und mehrfach wiederholt,

haben aber noch zu keinen strukturellen Ergebnissen geführt. Im Fall von Bacteriorhodopsin wurde zeitaufgelöste Pulverbeugung mit einem monochromatischen Röntgenstrahl gemessen, wobei Tausende von Beugungsbildern auf dem Detektor akkumuliert wurden. Auf diese Weise habe ich eine millisekunden-zeitaufgelöste Differenzkarte vom Wildtyp-M-Zustand erhalten. Die Experimente an Myoglobin und PYP wurden in Zusammenarbeit mit externen Arbeitsgruppen durchgeführt.

1 Summary

The thesis presented here describes the application of intense, pulsed X-rays from a synchrotron to the investigation of biochemical reactions triggered by light. The work includes contributions to the instrumentation of a beamline and experiments with the proteins myoglobin, the photoactive yellow protein (PYP) and bacteriorhodopsin.

The instrumental work led to an improvement of the time resolution for pulsed Laue experiments from 10 ns to 100 ps. My contribution was the integration of three major new components, a femtosecond laser system, a fast X-ray chopper and a heatload x-ray shutter, into the beamline control system. For laser/X-ray pump probe experiments, the time delay can now be tuned under software control with picosecond precision. As a diagnostic to verify the photo-excitation of samples, I constructed a microsecond time-resolved spectrometer with micro-focusing capabilities, which can measure the excitation degree of a sample online or offline. As part of an external collaboration, I contributed to the construction of a femtosecond time-resolved offline spectrometer. It was built to answer the question whether protein crystals can be excited with a focused femtosecond laser to a sufficiently high degree without damage, and to identify the optimal triggering conditions.

The laser triggering studies showed in the case of myoglobin that a protein crystal can be excited with femtosecond laser pulses without disordering the crystalline structure or introducing photochemical damage. 100-ps time resolved Laue diffraction experiments on Myoglobin-CO show structural dynamics compatible with earlier nanosecond experiments, but no clear indication for a CO docking site. A nanosecond time-resolved Laue experiment on PYP showed an early photocycle intermediate, with a photo-isomerized chromophore but little larger rearrangement in the protein. Although technically successful 100-ps time-resolved Laue diffraction experiments on PYP have been repeated several times, they have not yet given structural results. In the case of bacteriorhodopsin purple membrane, time-resolved powder diffraction with a chopped monochromatic X-ray beam was used, accumulating thousands of images on the detector. In this way a millisecond time-resolved electron difference map for the wild-type M state

was obtained. The myoglobin and PYP experiments were collaborations with external workgroups.

2 Introduction

The Laue method is the fastest method to collect diffraction data from crystals. The exposure times are typically 1000 to 10000 times shorter than for monochromatic images. With the unprecedented photon flux from an ESRF beamline, the exposure times could be reduced from the millisecond to the microsecond time domain. This is an important step because the round trip time of the electrons in the synchrotron ring is also in the microsecond range. By taking advantage of the time structure of the synchrotron radiation, this opens opportunities for dynamic studies with up to 100 ps time resolution. An application of this unique time resolution in crystallography is the study of photochemical reactions, in which structural changes in a sample can be synchronously triggered by a light flash. By analogy to a laser-spectroscopic pump-probe experiment, the exciting laser is followed by a time-delayed probe X-ray pulse and the diffraction pattern is recorded on an area detector. The measured time-dependent intensity differences give structure factor changes, which can determine atomic displacements.

3 Photoactive Proteins

3.1 Myoglobin

The biological function of myoglobin is to store oxygen in muscle cells, just as hemoglobin transports oxygen in blood cells. Muscle cells need myoglobin as peak-load buffer when the blood cannot supply oxygen fast enough, for example when the circulation is blocked during muscle contraction. One would not normally refer to myoglobin as a photoactive protein. But one of its less known properties is that when exposed to an intense light flash, it can temporarily release its stored oxygen.

Its structure is very similar to that of the subunits of hemoglobin. Hemoglobin is a tetramer of four myoglobin-like units. Myoglobin is a compact globular molecule with a

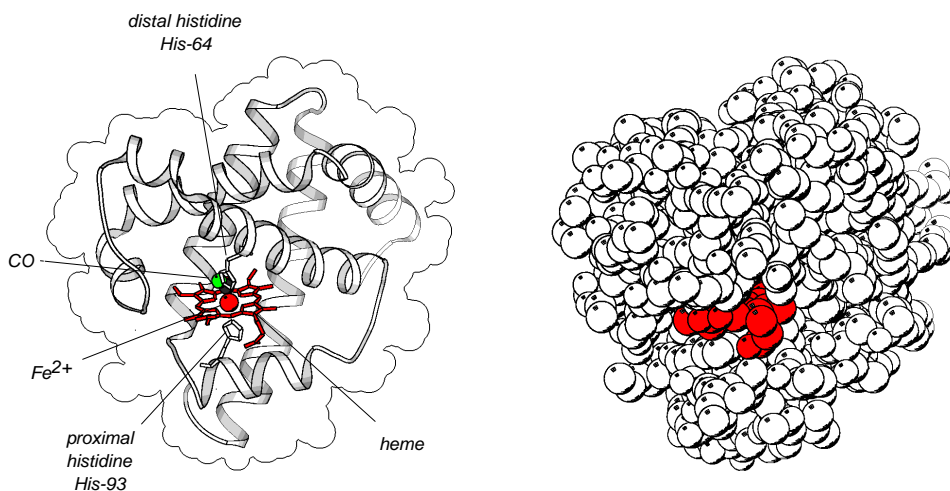


Figure 1: Myoglobin-CO structural model

Left: protein backbone and functional groups. It is the C atom (black) of the CO molecule that is covalently bound by the Fe^{2+} in the center of the heme group. Right: Van-der-Waals radii (without hydrogen). Note that the binding site is buried in the protein. Model by Kuriyan, Karplus & Petsko 1986-87, PDB 1mbc, graphics by Molscript 1.4 © Per Kraulis 1993

molecular weight of 17800 Dalton¹, composed of a single polypeptide chain of 153 amino acids.

The oxygen is bound by a Fe²⁺ atom in the center of a porphyrin ring embedded within the hydrophobic interior of the protein. The porphyrin ring and its iron atom constitute the *heme* group, which is anchored to the protein through a covalent link to a histidine residue (*proximal histidine*). As Figure 1 shows, the binding site is buried in the protein with no obvious opening to the outside. The motivation for doing time-resolved structural studies on myoglobin is to learn more about the pathway of the oxygen entering and escaping than could be guessed based on the static structure and to identify rapid structural changes associated with ligand release and rebinding. The distal histidine is supposed to act as a "door stop" with two stable positions, opening and closing a channel through which the ligand can enter from and escape into the solvent.

The solutions of the 3-dimensional structures of myoglobin by John Kendrew and of hemoglobin by Max Perutz were the first of many great feats of molecular biology. By the end of the 1950s Kendrew's study was largely complete and demonstrated the power of X-ray crystallography. For practical reasons, he chose sperm whale myoglobin for his work because it is stable, crystallizes well and was readily available.

The time-resolved studies are done on CO-ligated myoglobin rather than the natural oxy-myoglobin. One of the reasons for this choice is the inherent instability of the latter. The oxygen tends to oxidize the Fe²⁺ to Fe³⁺ converting it to inactive met-myoglobin. Because the auto-oxidation constant for sperm whale myoglobin is 0.055 h⁻¹ at 37°C [Springer *et al.* 1994], an oxy-myoglobin sample would have to be prepared the day of the experiment. A more important reason for choosing CO over O₂ is the difference in their photolysis efficiency. In oxy-myoglobin rapid geminate recombination ensues after photolysis with most of the oxygen rebinding within 100 ps to its original iron site. Although myoglobin binds CO more strongly than O₂, the rate of CO geminate recombination is far slower. Consequently, the photolysis yield for carbonmonoxy-myoglobin is nearly 100%.

¹ Atomic mass unit, approximately the mass of a hydrogen atom, 1 Da = 1 u = 1.66 · 10⁻²⁷ kg

Myoglobin binds CO 30 times more strongly than oxygen. This relative affinity ought to be compared to the relative affinities of pure *heme* in solution without protein environment, where CO binds to free heme 1500 times more strongly than oxygen. Clearly, the protein environment influences the relative binding affinities of CO and O₂. This relative inhibition is important: given this inhibition, CO produced endogenously by the metabolism of heme poisons only about 1 % of the myoglobin (5 % for smokers).

Time-resolved infrared spectroscopy has provided evidence for an intermediate "docking site" for CO prior to its escape into solution. Then, the CO remains localized within a "B-state" docking site for about 200 ns after which it migrates through the protein and escapes into the surrounding solvent with a time constant of about 3 μ s [Anfinrud 2000]. From there the rebinding is diffusion-controlled, and its time scale depends on the concentration.

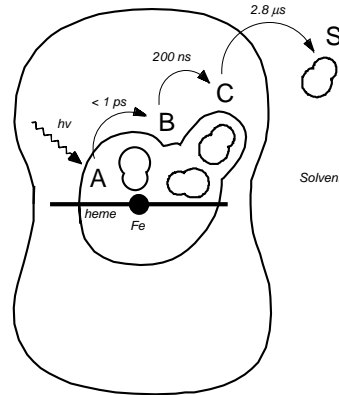


Figure 2: Model for the photolysis of MbCO

After flash photolysis the CO occupies 2 intermediate sites before escaping into the solvent [Anfinrud 2000].

In 1994 the existence of an intermediate site was identified by cryo-crystallography by Ilme Schlichting [Schlichting *et al.* 1994] and the group of Keith Moffat [Teng *et al.* 1994]. At temperatures below 40 K myoglobin loses its flexibility, so that after photolysis, the ligand can no longer escape from the *heme* pocket and remains trapped at a docking site. The results show clearly a docking site in the *heme* pocket with two possibilities for the orientation of the CO, together with a displacement of the iron atom out of the *heme* plane away from the CO (*heme* doming). However, it remains unclear whether the docking site found at low temperature is really the same as an intermediate state under physiological conditions.

For this reason the group of Keith Moffat pursued a time-resolved crystallographic study of the photolysis at room temperature where functional flexibility of the protein is retained, using pulsed Laue diffraction. This work has been performed in collaboration with Michael Wulff at the ESRF [Srajer *et al.* 1996].

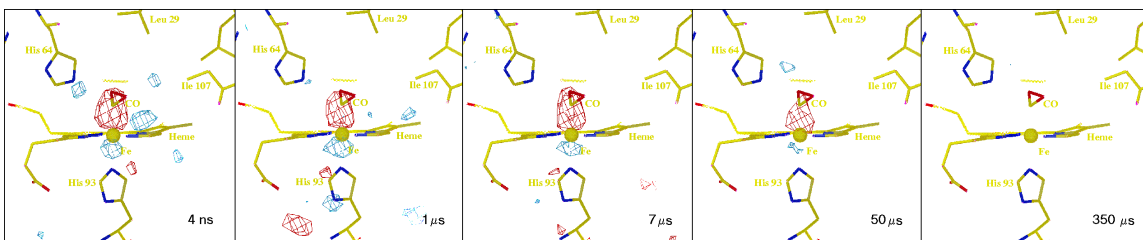


Figure 3: The photolysis and rebinding of the CO ligand in myoglobin

This series of electron difference maps is based on pulsed Laue data collected at the ESRF ID9 beamline [Srajer et al. 1996]. In the 4 ns map, the positive blue features around the red hole left by the CO, could be indicative of a docking sites. Electron density maps calculated by Thomas Ursby, contoured at $+3.5\sigma$ (blue) and -3.5σ (blue).

This study showed again, besides the hole left from the CO escaping, features such as the heme doming and indication of a CO docking site. However, the evidence for intermediate sites is not as clear as from the low temperature studies. The fact that Laue diffraction gives lower resolution data compared to monochromatic crystallography might be one explanation. But the time resolution of this study was limited by the laser pulse duration of 7 ns, which does not match the lifetime of the intermediate states seen by spectroscopy. For this reason it was decided to follow up the project with a faster laser, to exploit the full time-resolution of the ESRF of 100 ps.

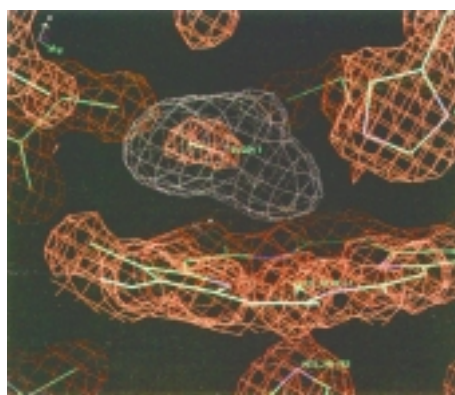


Figure 4: Predicted CO intermediate sites in Myoglobin

Molecular dynamics simulation of the distribution of the CO molecule after photolysis at 300 K [Vitkup et al. 1997].

3.2 Photoactive Yellow Protein

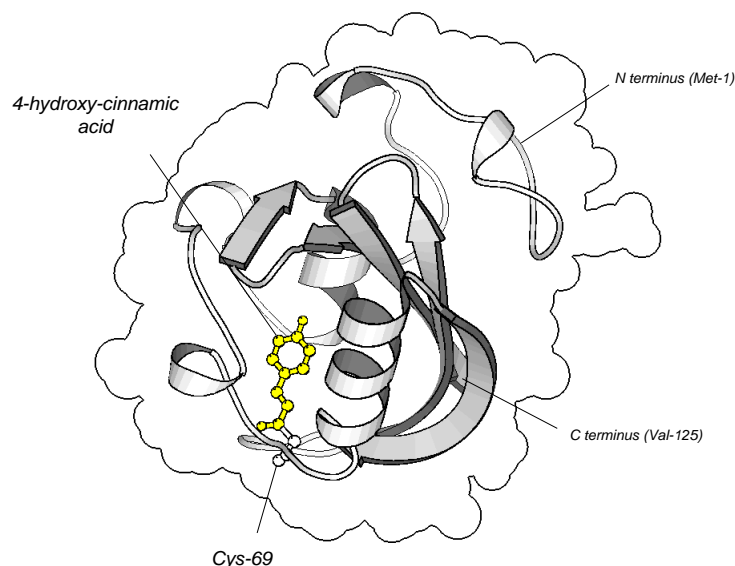


Figure 5: Structure of Photoactive Yellow Protein

Shown is the Protein backbone and the chromophore 4-hydroxy-cinnamic acid attached to Cys-69 and the protein envelope. PDB entry 2PHY [Borgstahl et al. 1995], Molscript 2.1.2 © Per Kraulis, 1998).

The Photoactive Yellow Protein (PYP²) is a photosensitive protein that has been isolated from a purple bacterium called *Ectothiorhodospira halophila*³. This organism lives in salt lakes under extreme conditions, 30% salt concentration, pH 8.5, temperatures up to 50°C and anaerobic environment. It was discovered initially in the *Summer Lake* in Oregon by J.C. Raymond & W. R. Sistrom in 1967 [Raymond & Sistrom 1967], then later in 1978 in the *Wadi Natrun* in Egypt. Their purple color comes from bacteriochlorophyll, enabling them to live on photosynthesis. However in contrast to algae they cannot reduce water but rely on H₂S as a source of hydrogen. This anoxygenic photosynthesis does not lead to the production of O₂ but of elementary sulfur, which is excreted in the form of small spheres sticking to the cell wall (therefore the name *ectothio*-). It was a surprise to T. E. Meyer in 1985 when looking for colored proteins in

² alternative name: Xanthopsin

³ alternative name: *Halorhodospira halophila*

these purple bacteria to discover a yellow protein [Meyer 1985]. In 1990 he also found PYP in two other halophilic purple bacteria, and in 1996 the gene of PYP was found in *Rhodobacter sphaeroides* [Kort *et al.* 1996].

PYP is believed to act as a photoreceptor responsible for the phototaxis of the bacterium *Ectothiorhodospira halophila*. It is attracted by red or infrared light and repelled from blue light. It swims by the use of a flagellum. In the absence of blue light it moves straight most of the time and changes direction only occasionally. The presence of blue light increases the frequency of direction changes. This simple mechanism leads to a net migration away from blue light. The wavelength dependence of the negative phototaxis action spectrum roughly matches the absorption spectrum of PYP [Sprenger *et al.* 1993]. However, direct proof that PYP is the photoreceptor for this response is still missing. For example, a successful experiment has not been conducted showing that a mutant bacterial strain with the gene encoding PYP eliminated does not respond to blue light anymore [Kort 1999] (p. 67-86).

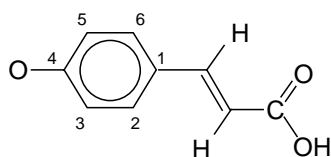


Figure 6: The chromophore of PYP, 4-hydroxy-cinnamic acid.

It is covalently bound to the cysteine-69 residue by a thioester bond.

PYP is a relatively small, water-soluble protein with a single chain of 125 residues and 14,000 Dalton molecular weight. It has a chromophore, called 4-hydroxy-cinnamic acid⁴, covalently bound to the protein, which accounts for its yellow color. The chromophore is buried in the hydrophobic core of the protein with no atom exposed to the solvent. PYP is, like bacteriorhodopsin, a very stable protein. Unlike bacteriorhodopsin, it is easy to crystallize and its crystals are very stable, well ordered and diffract to high resolution.

⁴ alternative name: *para-coumaric acid*

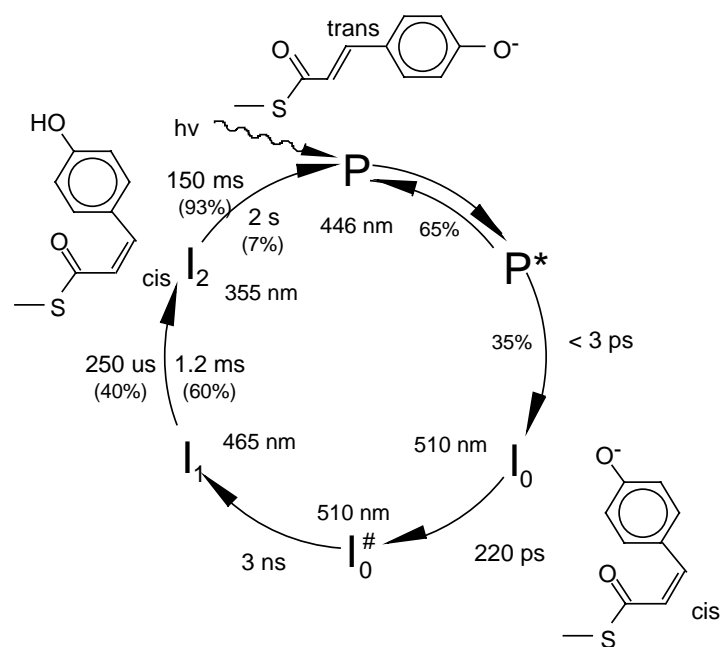


Figure 7: Photocycle of the photoactive yellow protein

In the ground state P the chromophore is in the *trans* conformation; but in the intermediate states starting with I_0 apparently in the *cis* conformation. P stands for PYP, I for intermediate. The wavelength is the center of the absorption band. Alternative nomenclature: $P = pG$ (PYP ground state), $I_1 = pR$ (PYP red shifted), $I_2 = pB$ (PYP blue shifted).

Upon absorption of a photon it undergoes with 35% probability a reversible photocycle with a total length of about one second. Four photocycle intermediates, characterized by their different visible absorption spectra are known. Probably the most long-lived (I_2) state is the signaling state. However, it is not known yet, with which signal-transducing molecule in the cell it interacts.

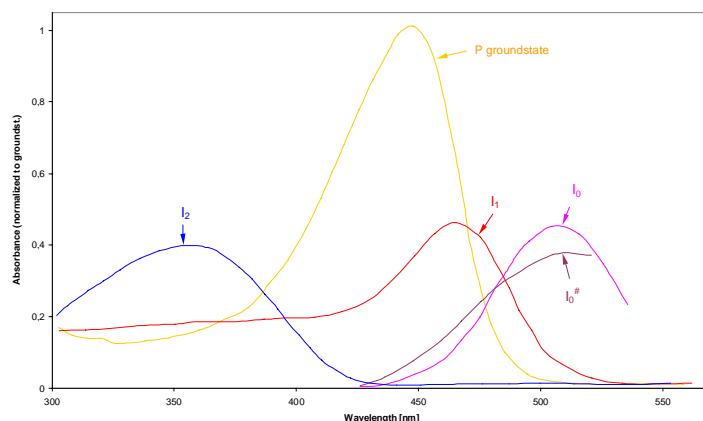


Figure 8: Absorption spectra of PYP photocycle intermediates

The spectra of the P ground state, I_1 and I_2 are taken from Hoff [Hoff *et al.* 1994]; the spectra of I_0 and $I_0^\#$ from Ujj [Ujj *et al.* 1998]

The primary event, which triggers the photocycle, is apparently an ultra-fast photoisomerization about the double bond of the chromophore.

X-ray diffraction studies on PYP photocycle intermediates have already been done by the groups of Keith Moffat and Elizabeth Getzoff in 1993. A 10-ms pulsed Laue experiment at the National Synchrotron Light Source [Genick *et al.* 1997] led to a structure of the I_2 state showing a large-amplitude motion of the aromatic ring of the chromophore (Figure 9). The motivation for continuing the PYP Laue diffraction studies was to extend the time-resolution to the earlier intermediates.

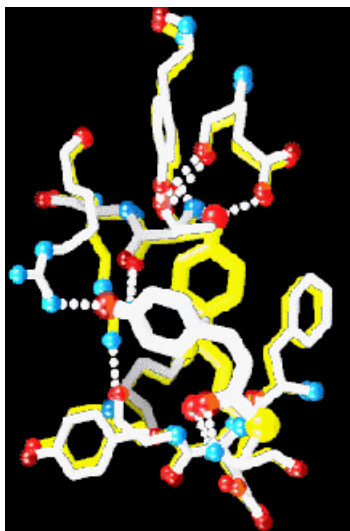


Figure 9: X-ray structure of the I_2 intermediate of PYP

The I_2 structure (white) is superimposed to the ground state structure (yellow). This structure was obtained by pulsed Laue diffraction. In a time window of 2-12 ms after laser excitation the chromophore is found with 50% occupancy in both conformations.

3.3 Bacteriorhodopsin

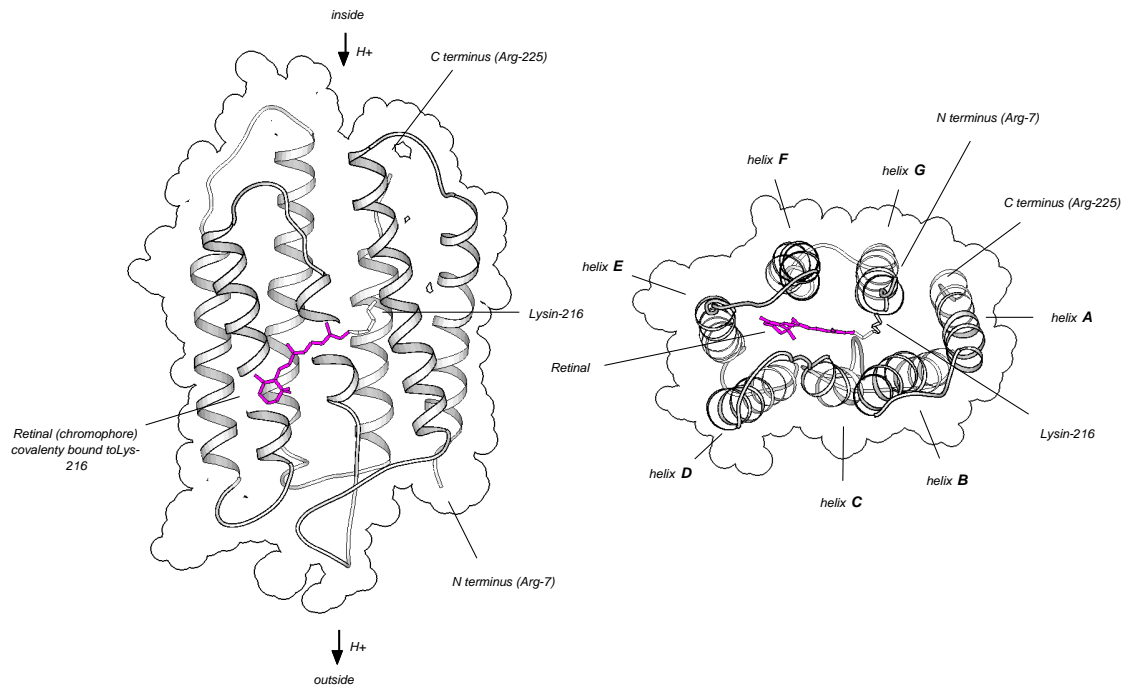


Figure 10: Structural model of Bacteriorhodopsin

The chromophore retinal is embedded between seven membrane-spanning α -helices. Upon absorption of a photon, a proton is transferred from the cytoplasmic to the extracellular side. PDB entry 1QHJ, based on X-ray data [Pebay-Peyroula et al. 1997] [Belrhali et al. 1999].

Bacteriorhodopsin (bR) is a purple, photo-active membrane protein found in the membrane of a photosynthetic bacterium *Halobacterium salinarum*⁵. The protein was discovered in 1971 by Walter Stoeckenius and received its name because it resembles the *rhodopsin* of the retina of the eye in many aspects [Oesterhelt & Stoeckenius 1971].

The biophysics of bacteriorhodopsin has been intensively studied since the beginning of the 1970s. In contrast to *rhodopsin*, it is easy to obtain and to handle, it is very stable and

⁵ Alternative names: *Halobacterium salinarum*, *Halobacterium halobium*.

its photochemical reaction is completely reversible. It can be photo-excited thousands of times without degradation.

Bacteriorhodopsin is a purple-colored protein. Its color comes from a retinal molecule, which is covalently bound to the amino acid chain. Normally retinal is of yellow color. The special environment of the retinal, embedded in the protein matrix shifts its absorption peak from 370 to 570 nm.

The biological function of bacteriorhodopsin is to fuel the bacterium by light. The *Halobacterium salinarium* is not a truly photosynthetic organism. Normally it lives as aerobic bacterium. However, in absence of organic nutrients and oxygen, bacteriorhodopsin allows the bacterium to survive using sunlight. Bacteriorhodopsin acts as a light-driven proton pump. It builds up an electrochemical gradient of up to 180 mV, which is used by another membrane protein, ATP-synthase, to provide the bacterium with ATP.

It is a relatively small protein with 26500 Dalton molecular weight with a single chain of 248 amino acid residues. The chromophore is a retinal molecule, which is covalently bound via a Schiff base to a lysine (residue 216). The protein chain is folded into seven α -helices, which are aligned roughly parallel to each other and span the membrane. The retinal chromophore is sandwiched between the α -helices in the middle of the protein. The retinal is roughly aligned to the membrane plane, at an angle of 23° .

Like most membrane proteins, bacteriorhodopsin is difficult to crystallize. It resisted all attempts to grow suitable crystals for X-ray diffraction from its discovery up to 1993 [Schertler *et al.* 1993] and only in 1996 high resolution data X-ray diffraction was available [Landau & Rosenbusch 1996]. Fortunately, bacteriorhodopsin naturally occurs inside the membrane in a close-packed, ordered form, forming a two-dimensional hexagonal crystal lattice. Such domains or patches of purple membrane have a diameter of typically 1 μm . Making use of the periodic structure, Richard Henderson was able to establish a low resolution model of the bR structure by 2D electron crystallography on single membrane patches [Henderson *et al.* 1986]. Low-resolution X-ray powder diffraction studies were also done on thick layers of purple membrane patches, deposited in an aligned way on a smooth substrate.

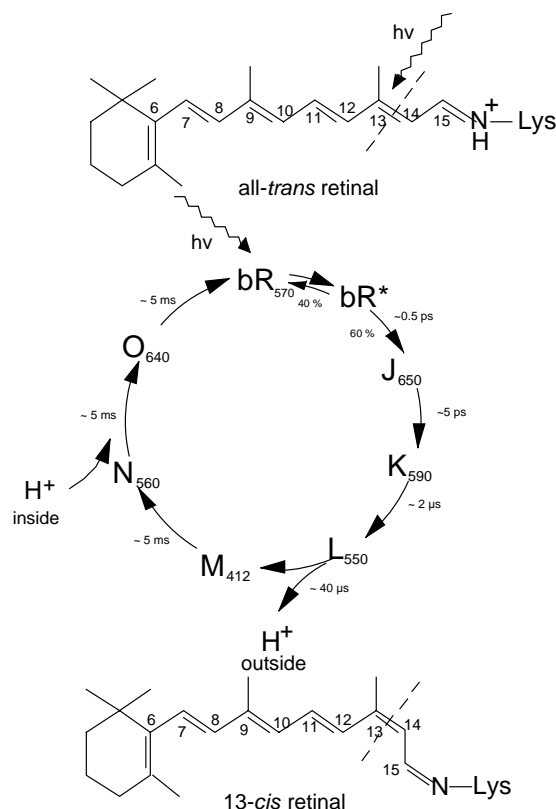


Figure 11: The photocycle of bacteriorhodopsin

The subscript numbers indicate the wavelength of the absorption maximum in nm. The intermediate life times are given for pH 7 at 20 °C.

Upon absorption of a photon, a bacteriorhodopsin molecule undergoes a reversible photocycle of intermediate states with lifetimes of femtoseconds to milliseconds. The overall photocycle takes about 5 ms at room temperature and pH 7. The first step that is triggered by the absorption of a photon is a *trans*-to-*cis* isomerization of one of the double bonds of the retinal molecule (*bR*^{*} → *J*). It is believed that the retinal acts like a lever arm, forcing the protein to rearrange around the new conformation of the retinal. Thus, it performs its biological function which results ultimately in a release of a proton at the extracellular side (*L* → *L*), followed by an uptake at the other end (*N* → *O*). With a final relaxation of the protein, the retinal re-isomerizes to the *all-trans* conformation (*O* state). The classification of the photocycle into the six intermediates *J*, *K*, *L*, *M*, *N* and *O* is based on visible absorption spectroscopy. These spectra do not reveal much

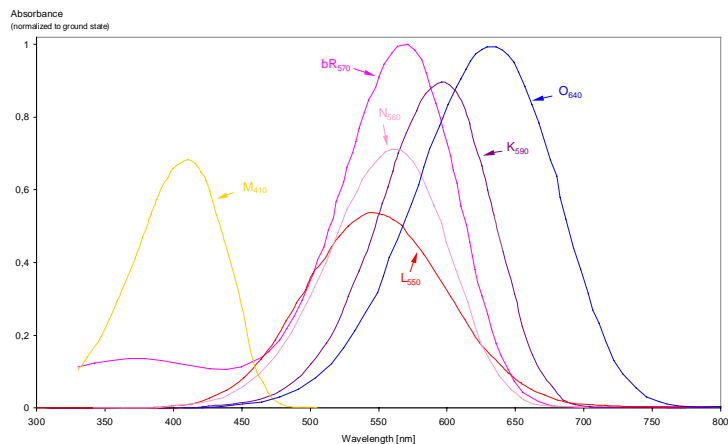


Figure 12: Absorption spectra of the Photocycle Intermediates

The intermediate spectra are calculated based on deconvolution and scaling of time-resolved difference spectra [Chizhov et al. 1996].

information about structural dynamics of the protein, since the absorption of the retinal is sensitive only to its closest protein environment. Infrared absorption spectroscopy suggests that there are actually additional intermediates such as KL, M₁, M₂, O₁, O₂ [Ebrey 1992].

4 Laboratory and Experimental Apparatus

4.1 The ESRF

The European Synchrotron Radiation Facility is a research institute founded by twelve European countries in 1988. The task of the ESRF is to produce synchrotron radiation and to support its use for the scientific communities of the twelve member countries.

The origin of synchrotron radiation has been known for long time. From the Maxwell equations (1873) it follows that an accelerated charge emits radiation. In 1887 Heinrich Hertz verified experimentally this prediction using an open electrical resonance circuit (Hertz dipole). But the radiation emitted from synchrotrons was not observed before 1947: on 24 April 1947 visible radiation was observed for the first time, at the General Electric's 70 MeV synchrotron, emitted tangentially from the circular electron beam [Koch 1983]. At this time synchrotron radiation was considered a detrimental effect which limits the achievable electron energy in an accelerator ring. It was not until the 1960's that scientists began to realize that synchrotron radiation has remarkable and useful features making it a tool of research itself: its wide range of wavelengths from microwaves to hard X-rays, tight collimation and high power density.

The ESRF is the first machine of the so-called *third generation*. The machine is optimized for the production of hard X-rays by insertion devices with small divergence, small source size, long lifetime and stability of the stored electron beam.

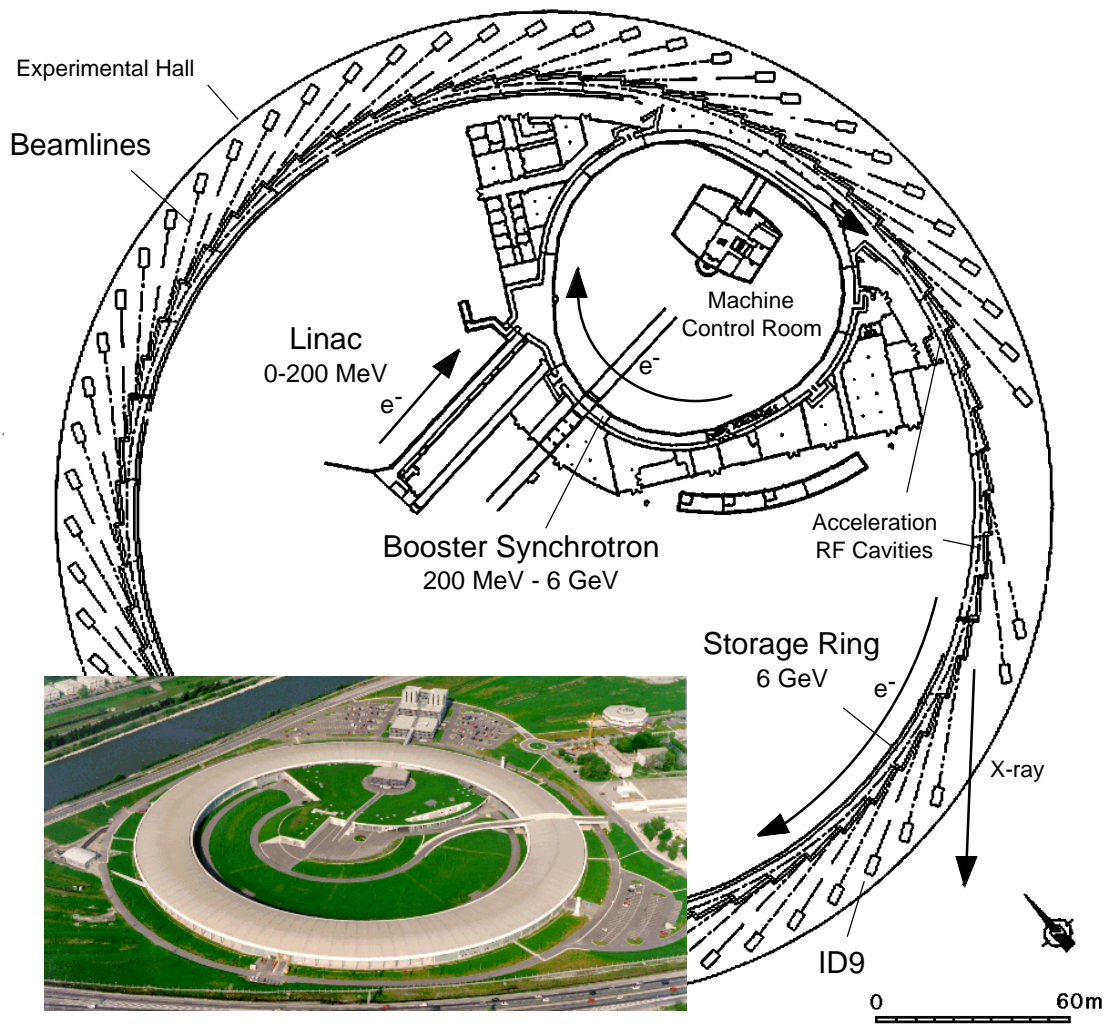


Figure 13: The European Synchrotron Radiation Facility, Grenoble, France

The ESRF storage ring has a circumference of 850 m and consists of 32 straight sections and 32 bending magnets in which the electron beam is deflected by 11.25° . Synchrotron radiation is always generated at the bending magnets and at the straight sections when they are equipped with insertion devices. As of 1999, 34 beamlines are operational, 22 insertion device and 12 bending magnet beamlines.

The electrons circulate in the storage ring at a kinetic energy of 6 GeV. The electrons lose 6 MeV per round trip due to generation of synchrotron radiation, mostly in the bending magnets, only about 20% typically in the insertion devices. To keep the

electrons at constant energy, six radiofrequency (RF) accelerators are integrated into the ring. For stability reasons these provide an acceleration potential larger than actually needed, up to 12 MV. But an electron takes up only as much energy as it needed to maintain its orbit. Since the electrical field is an AC field the acceleration gradient seen by an electron passing through the RF cavity depends on its phase. An electron below nominal energy would be deflected stronger at the bending magnets, run with a shorter radius, complete its orbit faster and pass the cavity the second time at an earlier phase where the gradient is stronger. The electron and would then be brought back to the nominal energy [Mills 1983].

The radiofrequency accelerators are powered by two klystrons, which require an electrical power of about 5 MW. About two thirds of the electrical power consumed by the ESRF site is used for the operation of the synchrotron. With a stored current of 200 mA the synchrotron generates about 1.2 MW of X-rays. However, most X-rays end in water-cooled copper absorbers, which form the outer wall of the vacuum chamber up of the bending magnet sections. The bending magnet beamlines can use only a very small fraction of the radiation because of the high divergence of the radiation fan.

Normally, the synchrotron is operated non-stop, delivering radiation 24 hours per day, except for one day per week which is used for maintenance and operation studies. The beam delivery is interrupted only three times per day for about 5 minutes for the refill of the storage ring. During this time the linear accelerator and the booster synchrotron are operated. The linac accelerates the electrons up to 200 MeV and injects them into the booster synchrotron ring. After the injection, the booster synchrotron's ring energy is increased from 200 MeV to 6 GeV by ramping up the magnetic field of its bending magnets. Finally, the beam is transferred to the storage ring at its nominal energy of 6 GeV by a fast *kicker* magnet. This procedure is repeated at 10 Hz until a stored current of 100 to 200 mA is built up. Every time, a new pulse train from the booster synchrotron is injected into the already stored one, packet by packet. At the beginning the two packets run on slightly different orbits, then the generation of synchrotron radiation damps their transverse oscillations within milliseconds and they merge into one.

The fastest time-resolved experiments make use of the time structure of the synchrotron radiation. The electron beam in the storage ring is bunched into packets of 1.5 to 3 cm

length, because the acceleration is provided by an alternating electric field. Only for a time window of 50 to 100 ps does the acceleration gradient in the radio frequency cavities match the round trip loss to within the acceptable limit [Mills 1983]. The radio frequency has been designed to operate on the 992nd harmonic of the orbit frequency. Thus one can fill the ring with up to 992 evenly-spaced bunches of electrons. These bunches are well isolated and electrons do not migrate between neighboring bunches. They do not have to be filled with equal charge. Any filling pattern created at injection time is conserved for the lifetime of the beam. The time structure found in the synchrotron radiation is exactly the same as that one of the electron beam.

The most interesting filling mode for sub-microsecond time-resolved experiments is the single-bunch mode in which only one out of 992 slots is filled. Unfortunately this is not the most popular mode, because only 15 mA of current can be injected and the lifetime of the beam is only 6 hours due to intra-bunch scattering (Touschek effect). In the normal 2/3 filling mode, 200 mA can be injected and the lifetime is 50 hours (Figure 14).

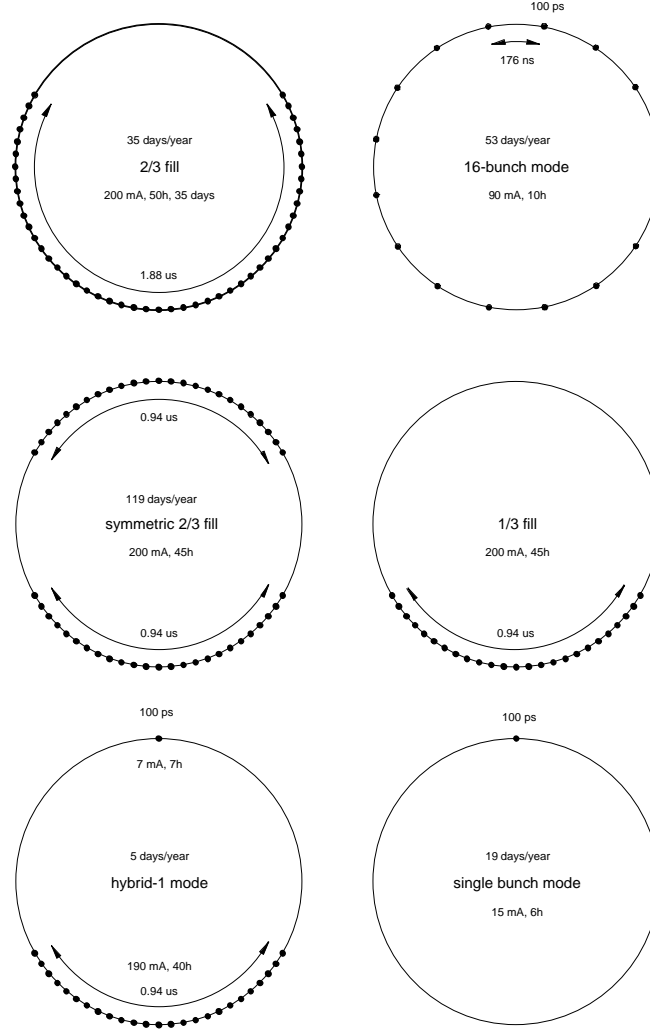


Figure 14: Filling modes of the ESRF

Given is the number of days per year for 1999 beam is delivered in user mode, The indicated figures are the filling current and the beam lifetime τ ($I = I_0 \cdot e^{-t/\tau}$). 1/3 filling mode was no longer scheduled for 1999.

4.2 The ID9 Beamline

The ID9 or white beam station is a dual-purpose beamline, partially dedicated to time-resolved, partially to high-pressure experiments. Its name stands for *insertion device nine*, because its insertion devices, two undulators and a wiggler, are installed in the 9th straight section of the storage ring. Its unique feature is to be able to deliver a focussed white beam, which requires high head load X-ray optics up to the sample. The beamline

was designed and built by Michael Wulff, except for the high-pressure station. The construction started in 1990 and the beamline has been operational since 1994.

The time-resolved and high-pressure experiments use two independent setups, built up in two separate cabins or experimental stations. The operation switches between these two stations about every two months, using equal shares of the available beam time. High-pressure diffraction experiments need X-ray micro-focussing because of the small sample volume. Another option to obtain diffraction data from small samples is to use energy dispersive diffraction, which requires a white beam. For this reason high pressure and Laue diffraction had been pooled together in the startup phase of the ESRF. Although a fully dedicated beamline for high-pressure studies became available in 1997, the sharing of ID9 has been maintained because of the high demand for high-pressure experiments.

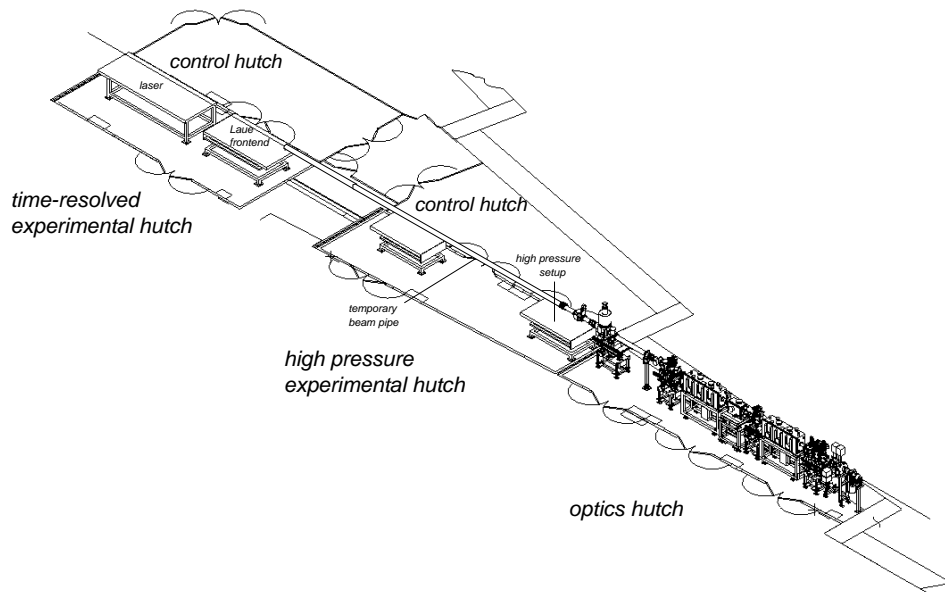


Figure 15: The ID9 beamline

Operation switches between time-resolved and high-pressure experiments in periods of two months. Each setup has its own lead-shielded experimental hut. Both use the X-ray sources and part of the X-ray optics in common. When the time-resolved station is in use, a temporary evacuated beam pipe is inserted.

4.3 X-ray Sources

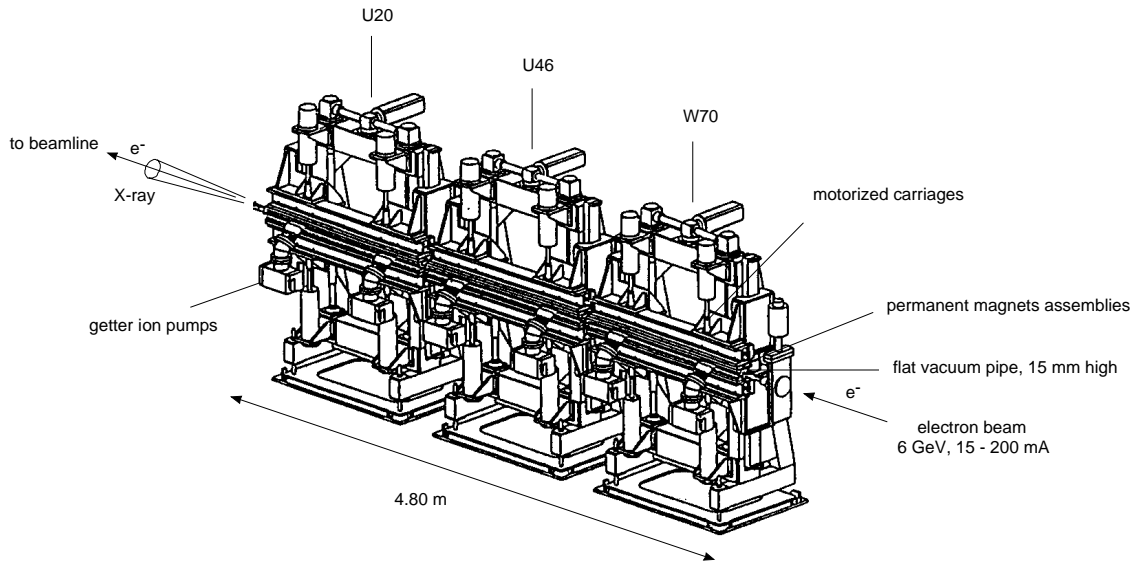


Figure 16: The ID9 straight section equipped with three insertion devices

The X-ray and electrons leave the insertion devices as collinear beams. The electron beam is deflected at the next bending magnet by 11.25° , whereas the X-rays continue straight into the beamline.

The ID9 straight section is equipped with three insertion devices, each taking up 1.60 m of the available 4.80 m. These offer a choice of source spectra for Laue diffraction experiments. The wiggler source offers the broadest spectrum and highest photon flux. It allows recording of the maximum number of reflections per image and minimizes the number of orientations of the crystal needed to obtain a complete data set. The disadvantage of this source is that a large fraction of the diffraction spots recorded will have harmonic contributions and have to be discarded or give less reliable data. Also, the images will be very crowded, so spatial overlaps are likely to occur. This source has been used up to 1997 for Laue diffraction experiments. The use of the U20 undulator will avoid these problems, however at the cost of collecting a larger number of images for a complete data set (typically ~ 100 , compared to 10-20 with the wiggler). The U46 undulator has a broad spectrum similar to the wiggler with about half the photon flux.

However, this spectrum has a rough, spiky structure compared to the smooth spectrum of the wiggler. This makes it more difficult to do a precise wavelength normalization of Laue data. So up to now, this source has not been used for Laue diffraction, except for technical studies.

Table 1: Characteristics of the insertion devices installed at ID9

| | Undulator U20 | Undulator U46 | Wiggler W70 |
|--------------------------|---------------|---------------|-------------|
| Period λ | 20 mm | 46 mm | 70 mm |
| Number of poles | 162 | 71 | 43 |
| Length | 1620 | 1679 | 1575 |
| Gap g | 16.3 mm | 16.3 mm | 20.1 mm |
| Magnetic field B_0 | 0.146 T | 0.360 T | 0.83 T |
| Deflection parameter K | 0.273 | 2.71 | 5.3 |
| Critical Energy E_c | | 15 keV | 20 keV |
| Fundamental E_f | 16.7 keV | 1.62 keV | 0.32 keV |
| Power P_{tot} | 80 W | 1.44 kW | 2.4 kW |

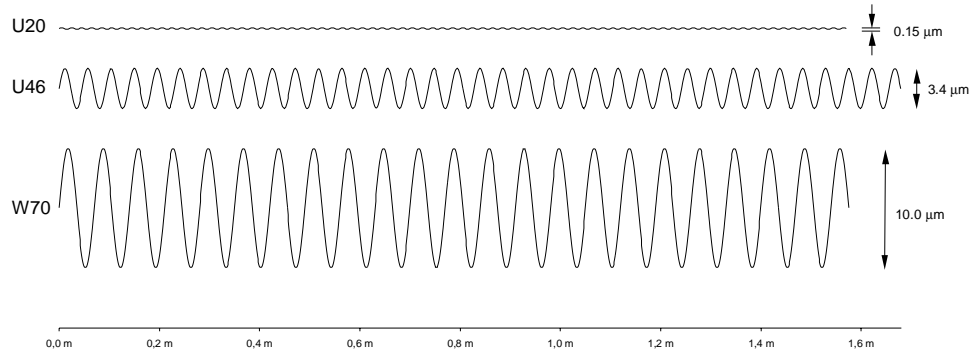


Figure 17: Single electron trajectories in an insertion devices

The individual electrons are forced to a wiggled trajectory in the horizontal plane by the sinusoidal varying magnetic field. The deflection is small compared to the horizontal electron beam diameter of 60 μm .

All insertion devices are built at the ESRF by a central facility, the *insertion device group*, for a cost of typically 600 000 F. They are made with NdFeB permanent magnets, which have a magnetic field of 2.3 T at their surface. These magnets are packed together

with anti-parallel polarity on two 1.6 m long rails mounted on motorized jaws above and below the flat vacuum chamber guiding the electron beam. The X-ray spectrum can be tuned by driving the jaws symmetrically closer to the chamber, altering the gap between the two magnetic arrays. Normally, only a single insertion device is used at a time, while the others are deactivated by opening the gap to the maximum of 300 mm. Due to the close packing, the magnetic fields of the opposite poles cancel out to a large extent. The magnetic B_0 field seen by the electron beam in the center of the vacuum chamber falls off exponentially with the gap:

$$B_0 = B_1 \cdot e^{-\pi g / \lambda} \text{ [Halbach 1981]},$$

where B_1 is the field at the surface of a magnet, g is the gap and λ is the period length of the magnetic array. For time-resolved experiments, usually the minimum gap is used to obtain the highest flux. The minimum gap is limited by the height of the vacuum chamber for the electron beam, which could be reduced from initially 20 mm to 16 mm in 1997. However, the W70 must not be closed to 16-mm gap because of a heat load limit on a vacuum window in the front end, and is limited to a minimum gap of 20.1 mm. When opening the gap of an insertion device, the power goes down exponentially with the gap size, the center of the spectrum shifts to longer wavelength and the harmonics of an undulator shift to short wavelength.

The W70 is an insertion device intermediate between a wiggler and an undulator, designed to deliver a maximum of X-ray power. This power optimum is obtained by choosing the magnetic period as the gap value times π (Wundulator maximum) [Wulff 1992].

The electron beam in the straight section is focused to 60 μm horizontal and 10 μm vertical (as of March 1999). The source point broadening due to the wiggled trajectory of the electron beam in the insertion devices is negligible. It is only 10 μm for the W70, 3.4 μm for the U46 and 0.15 μm for U20 (Figure 17). However, this does not mean that the source size is 60 by 10 μm only. Especially in case of the W70, the effective source size is significantly larger in the horizontal plane. Due to the divergence of the X-ray beam over the 1.6 m length of the insertion device, there is a depth-of-source broadening

seen in the focal spot size [Wulff 1992]. In the case of the W70 the effective source size

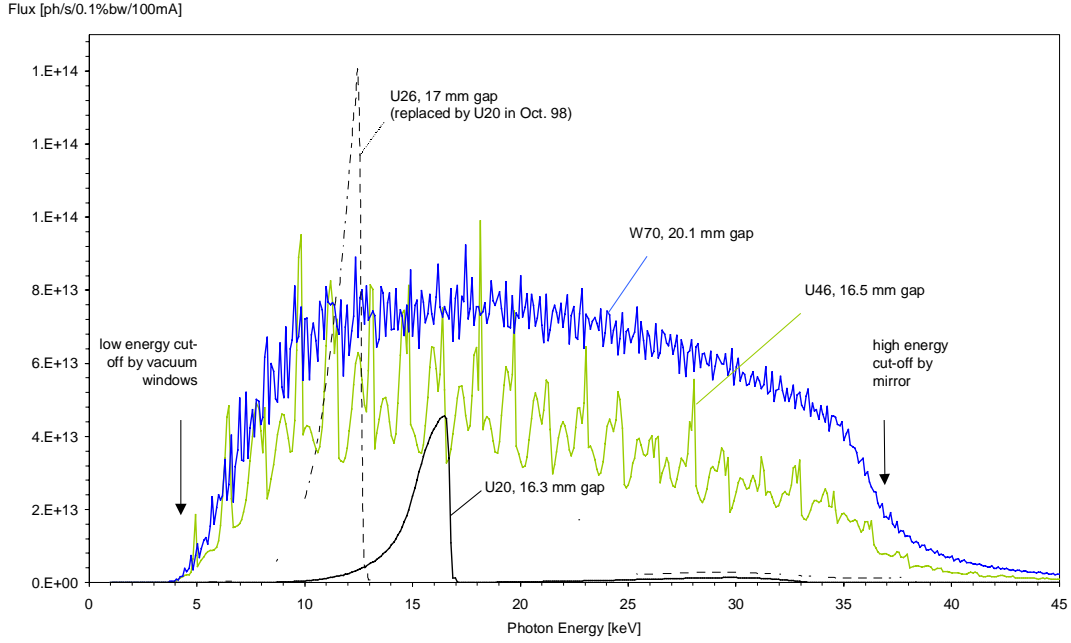


Figure 18: Spectra of the ID9 insertion devices

12.4 keV photon energy corresponds to 1 Å wavelength. Spectra calculated with XOP 1.9 / Xus 1.9, electron beam 6.04 GeV, $60 \times 10 \mu\text{m}^2$, $88 \times 3.8 \mu\text{rad}$ divergence, X-ray acceptance aperture $1.4 \times 24 \text{ mm}^2$ in 27 m distance. The absorption of the windows 0.26 mm carbon and 1.2 mm beryllium, and the reflectivity of the mirror at 2.3 mrad is taken into account.

is broadened from 60 μm to 220 μm .

The power of the sources has been experimentally verified by calorimetric measurements (see appendix, section 9.1). The white beam absorbed by a copper block and its temperature rise as a function of time is measured with a thermocouple. The power is calculated from the known heat capacity of the absorber. The measured values are 50% to 60% of the values one would expect, taking into account collimating apertures, transmission of the vacuum windows and the mirror reflectivity. The discrepancy can probably be attributed to a degradation of the platinum mirror coating, leading to a loss in reflectivity.

3.4 X-ray Optics

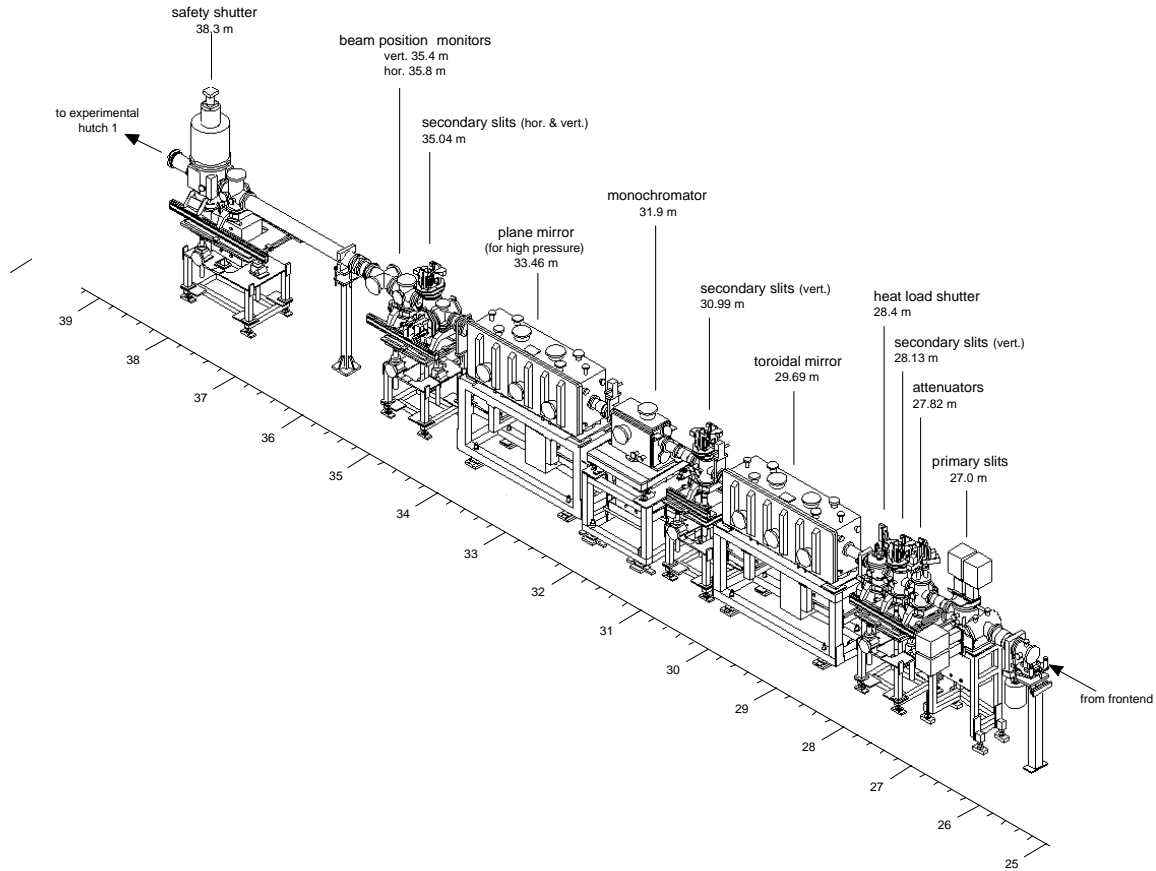


Figure 19: Beamline optics components

The indicated distances refer to the center of the straight section (U46). These components are enclosed in the optics hutch, a lead-shielded cabin separate from the experimental hutches (ESRF drawing no. 23.11.1006).

An X-ray beamline in its simplest form is a vacuum tube, which guides the X-ray beam tube from the electron storage ring tangentially to the experiment. The vacuum is necessary because of the absorption of the X-rays in air (33% per meter at 15 keV). Also, X-rays in air would create ozone, which attacks the optical surfaces. Into this vacuum pipe the optical components are integrated, such as collimating slits, focussing mirrors, shutters and the monochromator. The vacuum has to be of good quality, better than 10^{-6}

mbar, to avoid hydrocarbon contamination, which leads to carbon deposits on surfaces exposed to the X-ray beam.

The ID09 beamline has been designed with high heatload components to be able to deliver a focussed white beam with up to 1 kW of heatload to the experiment.

For a typical pulsed Laue experiment, only a fraction $1 / 300\,000$ of the incoming X-ray flux is contributing to the experiment. So it is important for the shutters to intercept as much as possible of the beam before it enters the experimental hutch in order to avoid problems with radiation background, heatload and ozone production.

Front end

The first section of the beamline, which is inside the 1-m concrete shielding of the storage ring, is called the *front end*. It forms the interface between the machine and the beamline and contains a vacuum window, filters, shutters, shielding, pumping stages and beam diagnostics.

A beryllium window of 0.5 mm thickness separates the beamline vacuum of 10^{-7} mbar from the machine vacuum of 10^{-9} mbar. This window is protected by a 0.26 mm carbon filter. It reduces the heat load by absorbing the soft part of the X-ray spectrum and heats up to 2000 °C.

A remote-controlled shutter allows interventions on the beamline optics while the synchrotron is operating. It consists of two stages, a water-cooled heatload absorber of GlidCop⁶, called *photon absorber*, and a 30-cm lead block, which is not cooled, called *beam shutter*. Its function is to stop the hard γ -rays, which are generated by accidental collisions of the 6-GeV electrons with the residual gas in the storage ring. This radiation called *bremsstrahlung* is (like the synchrotron radiation) strongly collimated in the forward direction and builds up over the full length of the straight section. It has a continuous spectrum ranging up to 6 GeV and even the lead block cannot fully absorb the high-energy part. However, the hardest part of the γ -rays will run through the rest of

⁶ copper strengthened with ultrafine dispersed particles of aluminum oxide

the beamline, including shutters, absorbers and the lead shielded walls, without any further interaction and is not harmful anymore.

Heat load shutter

The heatload shutter is a fast-operating X-ray shutter, which can support the full heatload of the wiggler beam of 1kW. Such a shutter is necessary to protect the microsecond X-ray chopper (p. 40). Because the latter is held in magnetic levitation in vacuum, it cannot be cooled efficiently and could not support more than 10 to 30 W of heatload.

The heatload shutter consists of a water-cooled copper block with a 4 mm high transmission slot. It is integrated into the beamline with flexible vacuum bellows, which allow it to rotate $\pm 7^\circ$ about its horizontal axis. When the slot is in a horizontal position, the X-ray beam is transmitted. When it is inclined at $+7^\circ$ or -7° , the X-ray beam is absorbed. The shallow incidence angle distributes the heatload over a maximum surface.

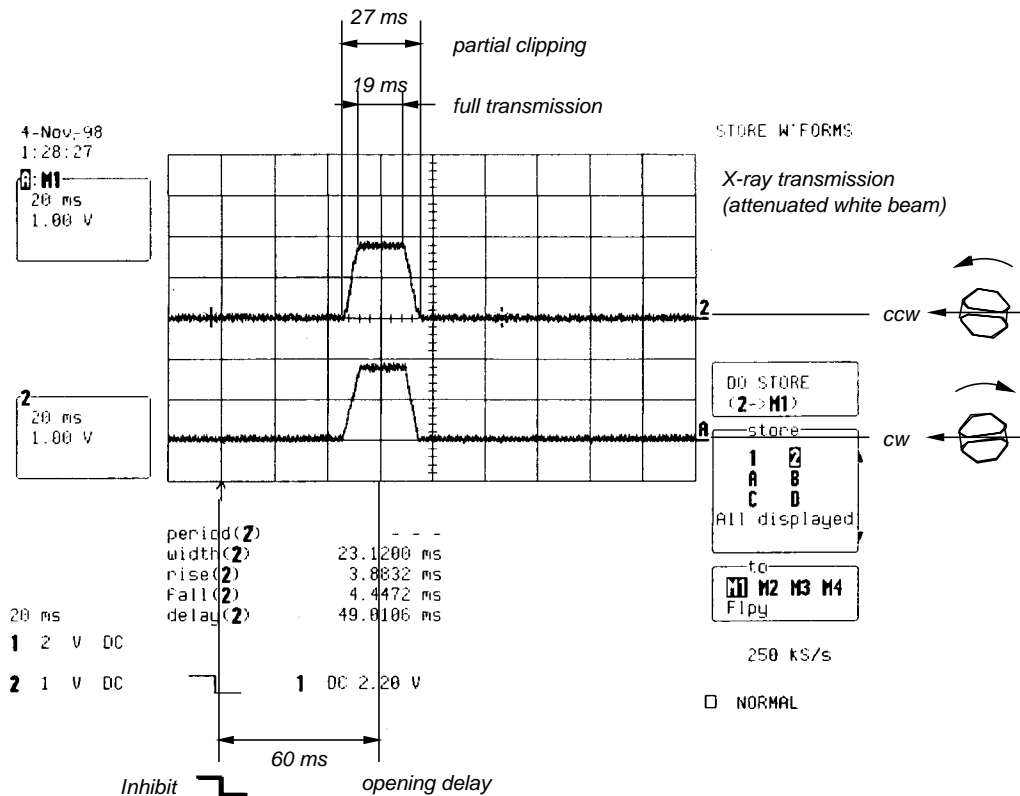


Figure 20: Performance of the heatload shutter

The X-ray transmission signal is recorded with an unbiased Si-PIN diode, a current amplifier with 10^5 V/A and 1 ms rise time filter and storage oscilloscope (LeCroy LC584A).

Toroidal Mirror

An X-ray mirror refocuses the diverging beam in the horizontal and vertical to the sample position, 55.3 m from the source. A toroid is an approximation for an ellipsoid, which would give a perfect point to point imaging. The mirror is polished to a cylindrical shape with 64.5 mm radius. It is supported close to its ends and bends under its own weight to a toroid with a meridional radius of 4.2 km.

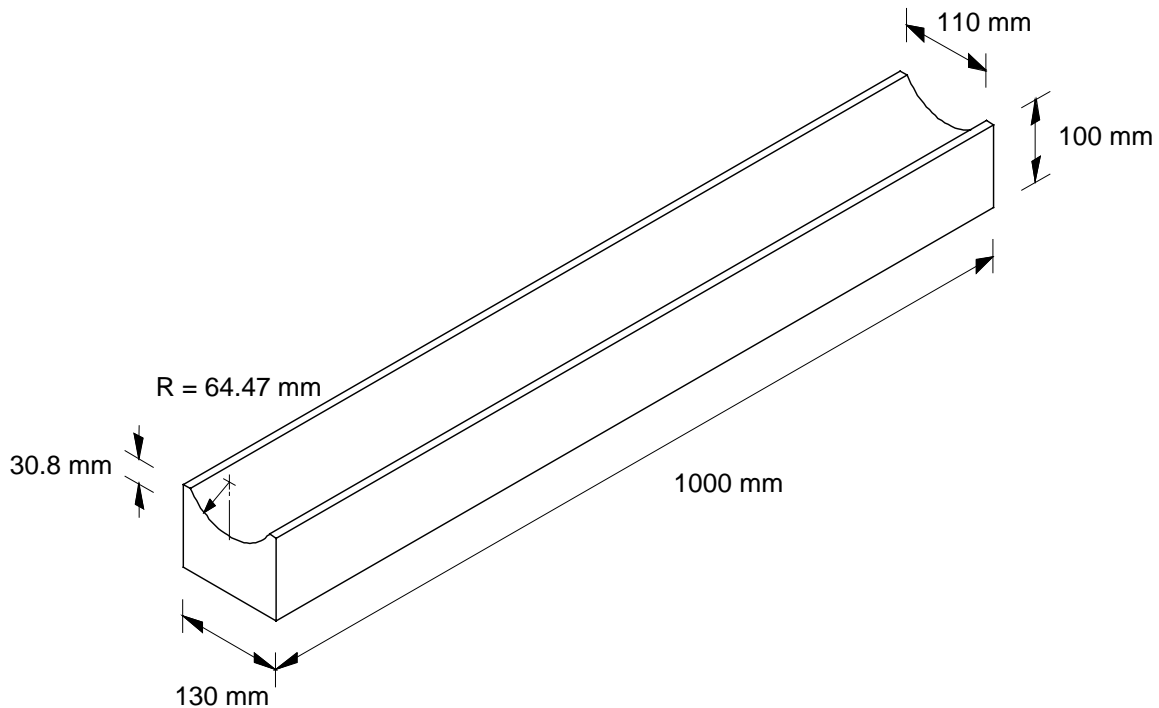


Figure 21: White beam focusing X-ray mirror

The mirror is polished as a cylindrical mirror and bends into toroidal shape in its support; material: graphite, coating: platinum, manufactured by Zeiss, delivered Jan. 1993.

The mirror has been manufactured by Zeiss, Oberkochen, in 1992 for a price of 220000 DM. Its body is made out of sintered graphite. It has a 200- μm coating of silicon carbide as a hard substrate for the polishing process. A 500 Å thick layer of platinum is deposited on to the polished silicon carbide via an intermediate binding layer. The surface

roughness was specified to be better than 3 Å, but Zeiss was able to obtain 1.8 Å. The longitudinal slope error after polishing was in the order of 10 µrad (2.5") RMS.

X-ray mirrors work in grazing incidence. All materials have a refractive index slightly smaller than 1 for X-rays. So at very shallow incidence angles, total external reflection occurs. Theoretically the reflectivity of the mirror should be 96%. However, calorimetric flux measurements and calculation of the power of the insertion devices and absorption of the beamline windows suggest that the reflectivity is only 50% (p. 30).

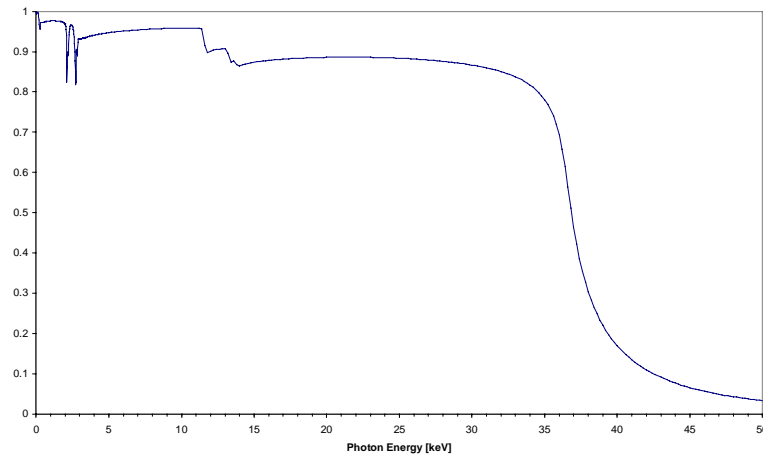


Figure 22: Reflectivity of the toroidal mirror

Theoretical curve for 2.3 mrad incidence angle, surface roughness 1.8 Å.

The fine structure at 2, 3, 11 and 13 keV is due to absorption edges of platinum

(calculated by XOP 1.9 / Xpower 1.0).

The angular acceptance of the mirror is about 24 mm horizontally and 1.4 mm vertically.

The horizontal focusing of the mirror is controlled by the incidence angle. The incidence angle θ for the imaging of a source point in the distance p for the mirror to the distance q is given by the following formula:

$$\theta = \frac{r}{2} \cdot \left(\frac{1}{p} + \frac{1}{q} \right)$$

where r is the sagittal radius of curvature.

To focus the beam in the experimental hutch 2 ($p = 29.69$ m, $q = 24.84$ m) an incidence angle of 2.3 mrad is required. The vertical focusing is controlled by the meridional radius of curvature R of the mirror, where

$$1/R = \theta/2 (1/p + 1/q). \text{ [West \& Padmore 1983]}$$

A piezoelectric actuator pushes up the central part of the mirror to reduce the natural curvature from the gravity sag from 5 km to 11.8 km. Due to limitations of the bending system, the curvature of the end parts of mirror cannot be controlled so well. So normally the outer 40% are masked by the horizontal slits because they would not contribute much to the peak intensity in the focus but rather to the wings of the focal spot.

The mirror is cooled from the long vertical sides by two spring-loaded vertical copper blades, which are water-cooled. Indium-gallium liquid metal improves the thermal contact between the copper and the graphite body. The temperature in the cooling circuit is kept at 30°C to make sure the metal stays liquid (indium-gallium solidifies at 20°C).

Normally, fused silica or Zerodur are the materials of choice for X-ray mirrors for beamlines, where the heatload is taken by the monochromator. These materials could not withstand the white beam because of their low thermal conductivity. The inhomogeneous heatload would deform of the mirror and could eventually make it crack. In 1992, when the mirror was ordered, graphite was the only choice for the material. Zeiss did not have enough experience with silicon. Sintered graphite is not the ideal material for ultra-high

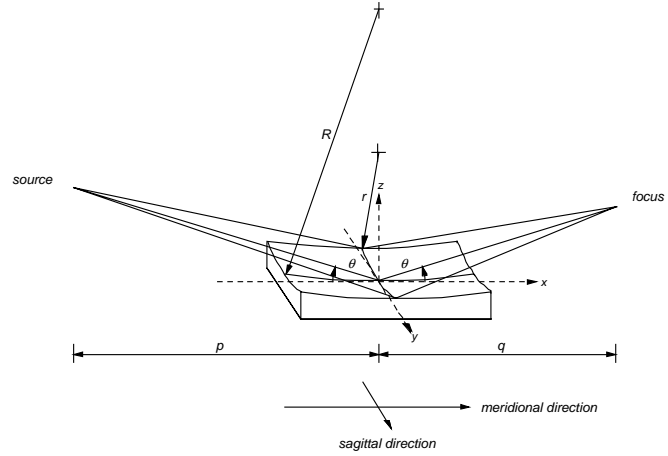


Figure 23: Focusing geometry of a toroid

vacuum. Because of its high internal surface, it acts like a sponge absorbing contaminants, which then slowly out-gas when it heats up. After installation, the mirror had to be heated under vacuum for weeks. Finally, after extra holes had been drilled in the SiC coating to accelerate the out-gassing, a vacuum level suitable for operation could be achieved. Yet, after five years of use, the vacuum level in the mirror chamber is not better than 10^{-6} mbar. Since 1994, toroidal mirrors are been made by Zeiss out of silicon single crystals, e.g. for Andrew Thompson for the D14 beamline. Silicon has a good thermal conductivity and is UHV-compatible. Its stiffness compared to graphite makes the gravity sag less serious and allows better curvature control by bending from the ends.

Monochromator

Although the ID9 beamline was conceived for white beam applications, there is a monochromator, which can be inserted when needed. It is useful for a number of time-resolved experiments that cannot be done with a white X-ray beam, such as time-resolved powder diffraction, X-ray absorption and diffuse scattering of liquids. Also diffraction experiments on single crystals which can be run at high repetition rate or where only one single Bragg reflection is recorded take advantage of the monochromator.

This high-pressure station of the beamline does not make use of this monochromator because it uses a bent-crystal focusing monochromator in 1-m distance from the sample to obtain horizontal micro-focusing.

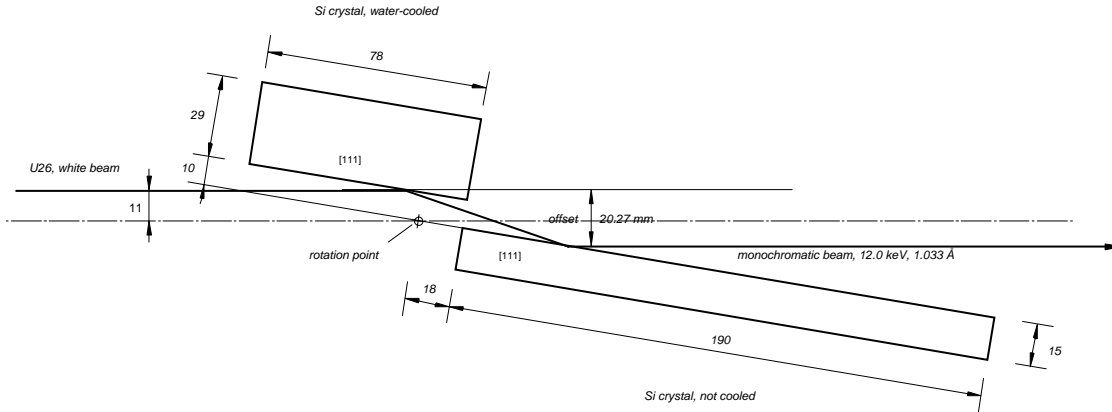


Figure 24: Bragg-Bragg monochromator

The figure shows the configuration used for the bR experiment using the peak flux of the Undulator-26. Installed Jan 1998 (ESRF drawing no. 23.22.1104, March 1998).

The monochromator consists of separate single crystals of silicon, which are cut, so their surface is parallel the (111) lattice plane. A piezoelectric drive (inchworm) fine-adjusts the parallelity of the two crystals. To achieve Bragg reflection on both crystal surfaces, the (111) lattice planes have to be parallel within 4 arc seconds (20 μrad). The monochromator is mounted on a rotation stage with 0.018° resolution. It has got a tuning range from 0.33 to 3.4 \AA (37 to 3.2 keV), limited by the length of the crystals.

The first crystal is water cooled because it absorbs most of the power of the white X-ray beam. The cooling system is designed to avoid a thermal gradient (thermal bump) on along the X-ray beam direction. If the Bragg angle would vary across the foot print of the beam, it could not be matched by the second crystal and part of the reflectivity would be lost. The heat flow on the surface that must be perpendicular to the X-ray beam direction. Thus, the crystal is cooled from the side by two vertical copper plates. The reflecting surface itself is an 8-mm deep and 20 mm wide groove in the crystal. This geometry forces the heat to flow parallel to the surface rather than from the surface to the bulk.

Theoretically, the monochromator should have a band pass of $1.35 \cdot 10^{-4}$ and a reflectivity of 95 %. When used with the undulator U20 one would expect a flux of $8.0 \cdot 10^{12}$ photons/s for 100 mA ring current at a wavelength of 0.75 \AA (16.5 keV). Experimentally, a flux of $3.7 \cdot 10^{12}$ photons/s, normalized to 100 mA, is measured with a calibrated PIN

diode. 40% of this flux can be focussed through a $50 \times 50 \mu\text{m}^2$ pinhole at the sample. In practice, the band pass is determined by the vertical beam divergence (ca. $50 \mu\text{rad}$) rather than the rocking with of the Si (111) reflection, so the monochromaticity should be only $4 \cdot 10^{-3}$ or 7 eV at 16.5 keV.

When the beamline is used in white beam mode, the monochromator is rotated into horizontal position so the beam passes through the gap between the two crystals. The resulting height offset of 20 mm between the white and monochromatic beam is compensated by translating the optical table in the experimental hutch vertically.

4.4 X-ray Chopper

The X-ray chopper is a fast mechanical shutter, which allows it to make use of the high white beam flux to obtain the shortest exposure times for time-resolved studies. It is a titanium disk with a $700\text{-}\mu\text{m}$ transmission channel held in magnetic levitation in vacuum. It is spinning at 900 revolutions per second and is synchronized to the synchrotron with 10 ns precision to take advantage of the time structure and allow clean single bunch extraction.

History

The use of rotating choppers to produce picosecond X-ray pulses from synchrotron sources had been demonstrated already in 1989 by LeGrand and Schildkamp at the CHESS synchrotron [LeGrand *et al.* 1989]. They used a titanium disk spinning at 447 Hz, shooting the X-ray beam through a $600\text{-}\mu\text{m}$ channel along its diameter, slightly offset from the rotation axis. With an opening window equal to the round trip time of the storage ring ($2.56 \mu\text{s}$) and only one electron packet stored they were able to obtain a single pulse Laue diffraction image from a lysozyme crystal.

Thanks to collaboration with the group of Keith Moffat from the University of Chicago, this device was on loan to the ESRF from 1994 to 1997. With a channel height of $650 \mu\text{m}$ this device had a $3.7 \mu\text{s}$ opening window at 445 Hz. This transmission slot is offset from the center to reduce the opening frequency by a factor two. This makes it easier for a mechanical blade shutter downstream of the chopper to transmit only a single pulse.

This disk was spinning in helium, because the frictional heating in air at a speed of 180 m/s would have been excessive. The housing of the chopper had no windows. It was flushed with helium at small flow, escaping through two 1-mm pinholes. The rotor axis was held by ball bearings, which would have to be exchanged after a few days of continuous operation. Although the rotor was driven by an electronically-commuted synchronous motor with quartz-stabilized clock, its phase jitter was too high for clean single pulse separation and predictable X-ray to laser timing. There would have been a 30% chance to transmit two pulses rather than one and there would have been an uncertainty of several synchrotron round trips ($2.82\text{ }\mu\text{s}$) in the arrival of the X-ray pulse relative to a laser trigger for the experiment. When installed at the ESRF, the chopper was synchronized by monitoring the phase of the rotor and triggering the experiment when the arrival time of the X-ray pulse was predicted to be centered within the mechanical opening position [Bourgeois *et al.* 1996]. This solution was implemented by Claude Pradervand (University of Chicago) by a VME card counting the time difference between a pick-up signal from the rotor indicating the opening position and the next single bunch time marker from the synchrotron. When found within a certain tolerance it would open the millisecond shutter for the next following opening of the chopper 2.2 ms later and trigger the laser for the sample excitation.

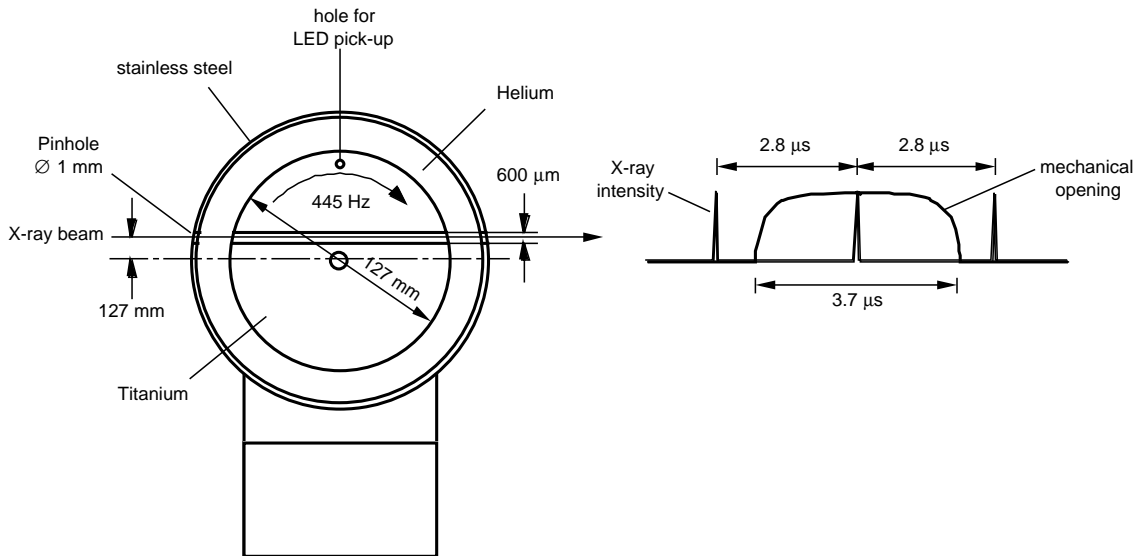


Figure 25: Prototype X-ray chopper by Wilfried Schildkamp

This device was developed at CHESS and later at the University of Chicago and was used on ID9 on loan from 1994 to 1997 [LeGrand et al. 1989].

The Jülich Chopper

The development of the chopper was a collaboration project between the ESRF and the *Forschungszentrum Jülich*. The *Institut für Grenzflächenforschung und Vakuumphysik* had already many years of experience with high-speed choppers when the project started in 1994. They had built neutron choppers for time-of-flight diffractometers for the Institut-Laue-Langevin in Grenoble, the Hahn-Meitner-Institut in Berlin and the National Institute of Standard and Technology's research reactor near Washington DC. Such a neutron chopper consists of seven synchronized Aluminum disks, coated with Gadolinium, rotating at 333 Hz, which act as a velocity filter for thermal neutrons.

The project was initiated in 1994 and followed by Dominique Bourgeois from the ESRF. Lin Zhang at the ESRF made an initial design study and stress analysis for the rotor. In Jülich, the mechanical engineering was done by Berndt Lindenau, the synchronization electronics by Jürgen Rübiger. The system was delivered and installed at the ESRF in September 1997. The total cost of the project was 371 600 DM.

For the construction of the chopper magnetic bearing technology had been employed, as it is used for turbo-molecular pumps. In fact the rotor shaft is the shaft of a Leybold

Turbovac 340M pump, which was developed by the same group in Jülich. Magnetic bearings have the advantage that they allow a body to rotate around its axis of inertia rather than around its geometrical axis. The deviation between these axes may be up to 0.2 mm. So the balancing is not so critical as with a mechanical bearing.

The magnetic bearing consists of a stack of permanent magnetic rings interlaced with iron rings. The iron rings that are attached to the rotor shaft. They are in an unstable equilibrium between the magnet rings and would collide within a fraction of a second. However, an electronic position control system immediately detects any deviation from the equilibrium and counteracts the movement with the force from a magnetic coil. In practice, the magnetic stacks would not collide if the electronic feed-back system is switched off. The rotor is retained by an auxiliary ball bearing after 0.15 mm of displacement.

For the X-ray chopper a triangle turned out to be the optimal shape. The transmission channel is on the edge of one side. The design minimizes the amount of material beyond the channel. With a circular disk, a channel would be a weak point where the outside segment could be torn off by the centrifugal forces (ca. 40 tons). In its cross section it is shaped like a muscle for better stress distribution, with ca. 25 mm at the hub and 7 mm at the outside. The function of the other two triangular sides is to balance the missing segment.

For equilibrium, it would have been sufficient to cut away just two identical segments opposite to each other. However, with the bar-shaped design, which was pursued up to Feb. 1997, the rotation would become unstable at a resonance of the magnetic bearing at 610 Hz. This was traced back to the unequal transverse inertia of the bar rotor. For a triangle the inertia for all transverse axes is the same.

The transmission channel is actually half-open. A 2.2-mm deep groove is milled into one of the sides of the triangle, covered with two 28-mm long "roofs" at both ends but left open in the center (see Figure 26). The adding of the roofs reduces the opening time by a factor 2 compared to open groove, because the beam is clipped symmetrically from two sides.

The additional material would not have been necessary for X-ray absorption and the opening time is only determined by the channel height at the entry and exit.

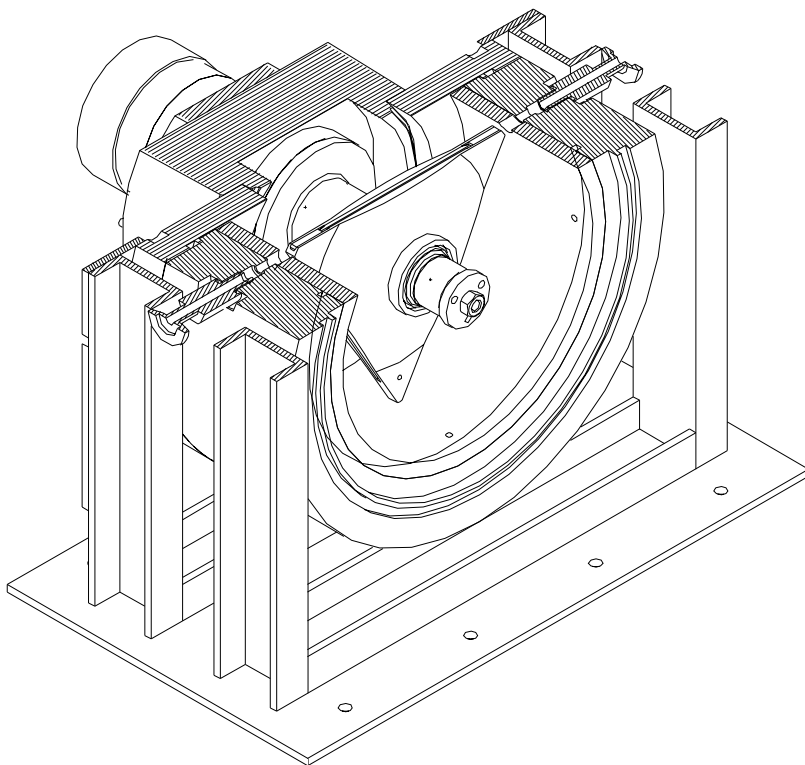


Figure 26: X-ray chopper (bunch selector) by Forschungszentrum Jülich

A triangular titanium disk rotates at 900 Hz in a vacuum and transmits the horizontal X-ray beam through a 800 μm slot once per turn. (Drawing by Michèle Soulier, ESRF, 1995).

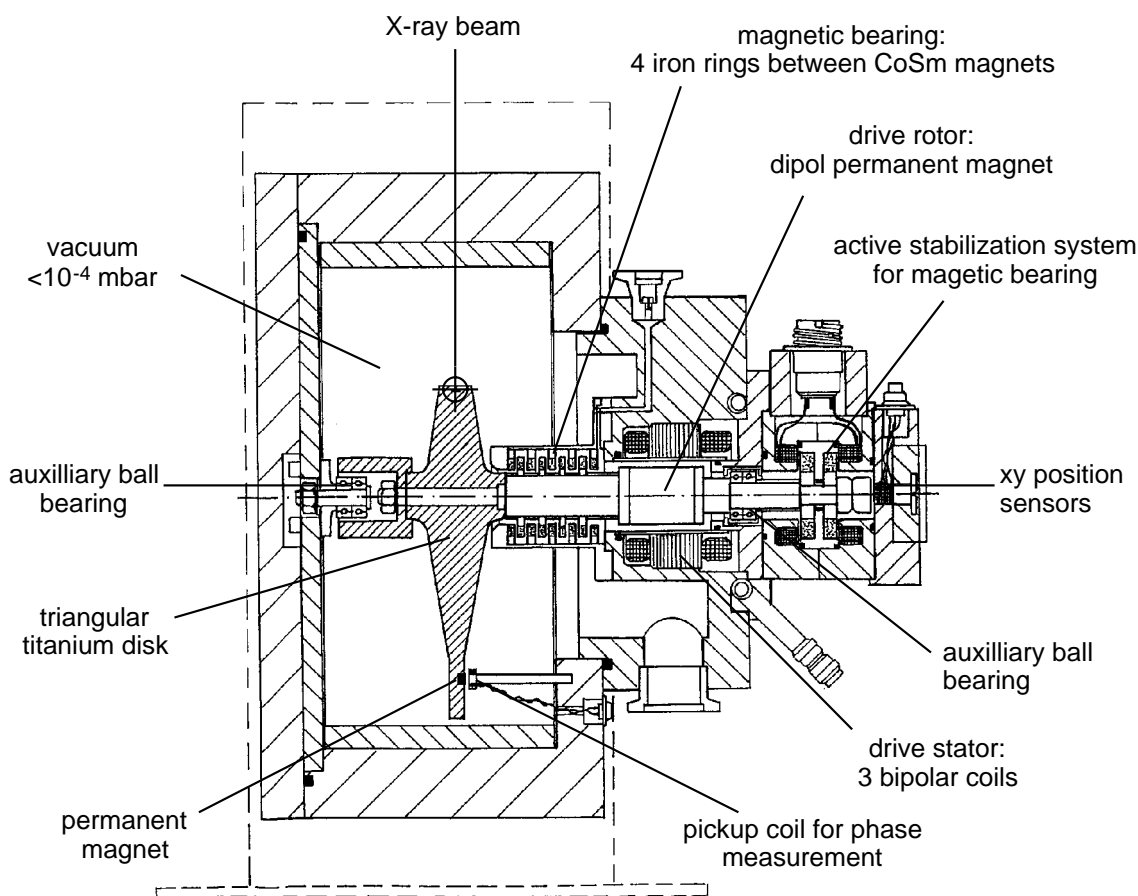


Figure 27: Cross section of the chopper:

The larger part of the drive and stabilization system is taken from a Leybold Turbovac 340 M pump. The turbine has been replaced by the chopper disk

The chopper is contained in a very solid vacuum vessel (10 mm Al + 30 mm stainless steel) to make sure that in case of a breakage of the chopper no fragments can penetrate to the outside. This makes the device very heavy (70 kg), but it also ensures good X-ray shielding. It helps to keep the background radiation in the experimental hutch low, since the X-ray flux sent into the chopper is 400 times higher than the flux sent to the sample. The interior of the house is black anodized for better absorption of thermal radiation, and the rotor is coated with black paint for better emission of thermal radiation (except the surface exposed to the X-rays). The temperature of the rotor must not exceed 50 °C. The maximum acceptable heatload on the rotor is in the order of 10 to 30 W.

The rotation of the chopper is synchronized to the synchrotron, using the 396th sub-harmonic of the round trip time of an electron bunch, with a precision of better than 10 ns. (This corresponds to 12 arc sec. or 6 μm at the end of the channel.) The opening window of the channel at 900 Hz is 1.46 μs .

The phase-locking of the chopper is done by a microprocessor controlled drive. Its actual phase is determined by a with 44 MHz resolution.

The controller consists of a 16-bit microcontroller, responsible for the phase adjustment of the rotor and damping of oscillations, and a field-programmable logic device (FPLD) responsible for the phase measurement and the electronic commutation of the 3-phase motor. The microcontroller (Siemens 80C166, 40 MHz) runs a program from two 32 Kbytes EPROMs. It also communicates with the external control program over the serial port and function keys on the front panels. It periodically reads out the sensors and updates of the LCD display. The FPLD (Xylinx XC4010) is initialized from a 128 kbit and a 64 kbit PROM at startup. The microcontroller communicates with the PCL over sixteen 16-bit-registers which are readable and writable via the external bus of the controller (16 bit data, 8 bit address). The FPLD generates the waveform for the 3-phase motor. The three sinusoidal drive current signals are generated by pulse width modulation at 18 times the revolution frequency (ca. 16 kHz at full speed). During the acceleration phase the frequency of the drive signal is increased in discrete steps. To keep the signal in phase with the rotor the microcontroller continuously updates the waveform. An interrupt driven routine writes a block of 18 new 8-bit values (0-63) to the FPLD at each turn of the rotor.

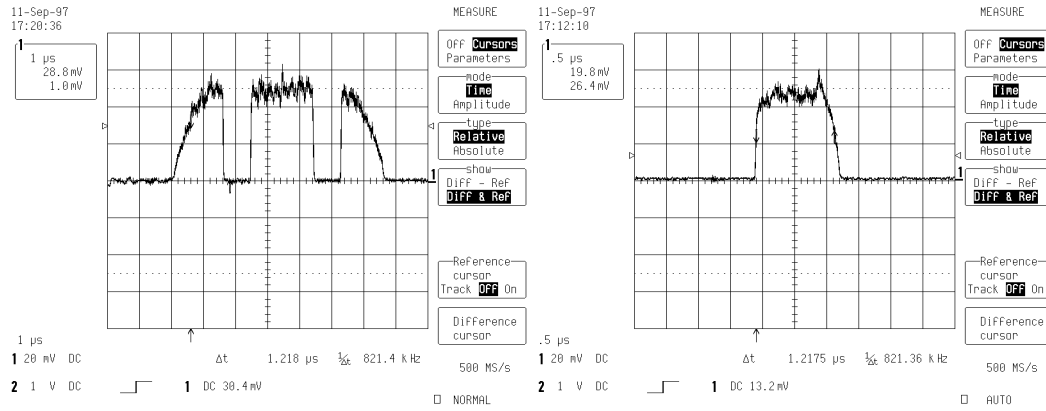


Figure 28: Measurement of the opening window of the chopper

The recorded signal is the X-ray transmission of the chopper channel. The synchrotron is in 2/3 fill mode, delivering $2.0 \mu\text{s}$ pulses with $0.85 \mu\text{s}$ gaps. The $2.0 \mu\text{s}$ pulses show fine structure resulting from the injection procedure.

Left: 200 Hz rotation frequency, baseline of opening window expected $6.62 \mu\text{s}$, measured $6.55 \mu\text{s}$, right: 896.57 Hz rotation frequency, baseline of opening window expected $1.48 \mu\text{s}$, measured $1.3 \mu\text{s}$. (source: U26, $1 \times 0.75 \text{ mm}^2$, attenuator: 3 mm Al, detector: avalanche photodiode)

4.5 X-ray Image Intensifier

The area detector used at ID9 is a medical X-ray intensifier tube coupled to a slow scan CCD, a system developed at the ESRF by Jean-Pierre Moy [Moy 1994].

An X-ray image intensifier (XRII) is an optical image intensifier made sensitive to hard X-rays by adding a layer of Cesium Iodide (CsI) to the photo-cathode. It is a vacuum tube, which accelerates the photoelectrons and refocuses them on to a phosphor screen, which is excited to luminescence. A diffraction pattern is thus transformed into an optical image.

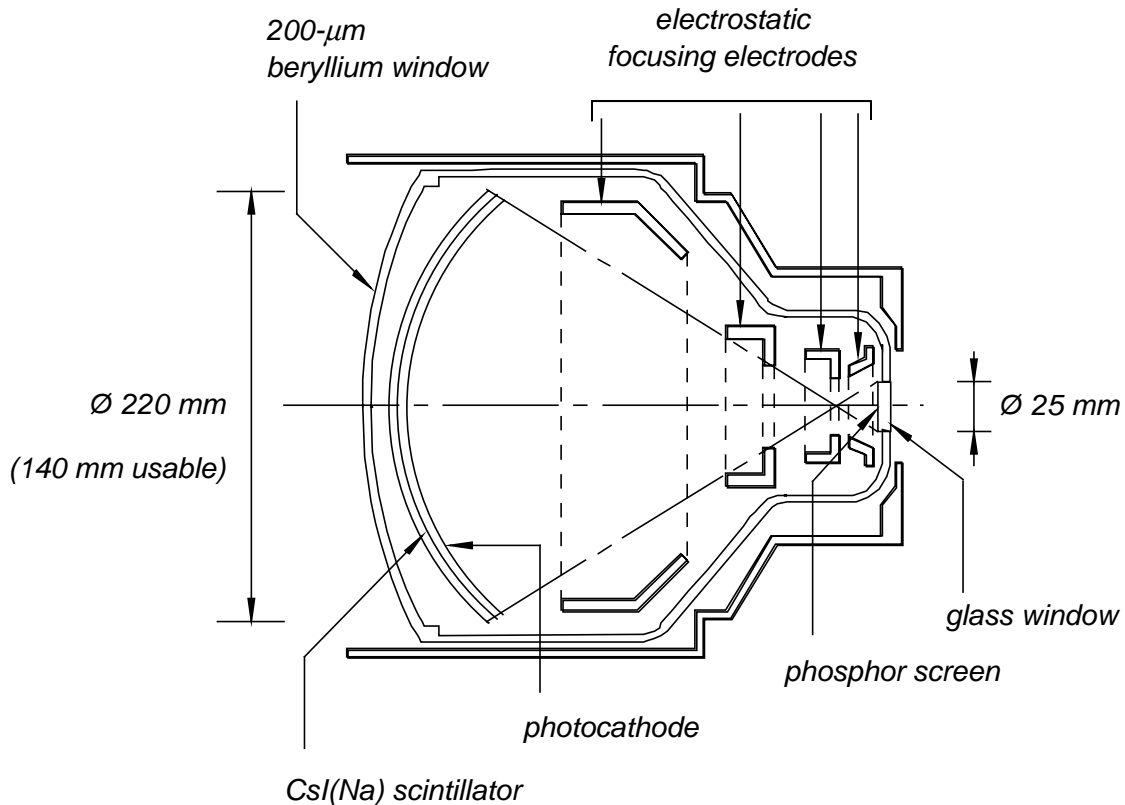


Figure 29: X-ray image intensifier

Model TH 49425 HX by Thomson Tubes Electroniques, Velicy, France

Normally, such X-ray tubes are used for medical applications coupled to a video camera, e.g. for on-line X-ray inspection during operations. Medical imaging is done with X-rays of 50 keV or more. To make the detector usable for crystallography, Thomson TE has

made detectors with beryllium windows rather than aluminum to ensure high efficiency down to 10 keV photon energy. Also this type has a thinner scintillator to improve the resolution.

The entry window is dome-shaped because this is best suited to resist the vacuum force. Behind the window, also dome-shaped, a 220- μm layer of CsI doped with sodium is deposited on a beryllium support. This layer absorbs the X-rays and converts them into blue light peaked around 420 nm. The sodium improves the conversion efficiency. The number of visible photons produced is proportional to the X-ray photon energy, 40 per keV. The scintillation decays with a time constant of 630 ns. The scintillator is coated at the backside with a transparent conducting 1- μm layer of In_2O_3 , on to which a 10 nm thick KCs photo-cathode is deposited. The photoelectrons are accelerated by a gradient of 30 kV towards the phosphor. It is a 1- μm layer of ZnCdS doped with silver (P20) that is covered with a thin aluminum layer to avoid feedback of the photo-cathode. It is excited to green fluorescence by the electrons, at a wavelength of 550 ± 25 nm. The phosphor is imaged by high-quality optics to a slow-scan CCD camera.

The camera is a liquid-nitrogen cooled system with 1242 by 1152 pixels made by Princeton Instruments, USA (model LN/CCD-1242E, 200,000 F) [Princeton-Instruments 1994]. The $27.5 \times 25.9 \text{ mm}^2$ CCD chip is made by *EEV*, England (model 05-30). It has a quantum efficiency of 40%. The pixels are $22.5 \times 22.5 \mu\text{m}^2$ in size, each with a capacity of 200,000 photoelectrons. When the capacity is exceeded the photoelectrons spill over into adjacent pixels in the same column. This effect is often observed around bright diffraction spots, called *blooming*. The CCD chip is cooled by liquid nitrogen to -100°C . At this temperature there is almost no dark current (less than 1 e^- per hour and per pixel), so the detector can accumulate X-rays over long time. The chip is connected via a cold finger to a reservoir of liquid nitrogen with a capacity of 2.5 liters, which has to be refilled every two days. It is not desirable to cool the chip to liquid nitrogen temperature (-198°C), because the detection and readout efficiency of the chip deteriorates below -120°C . Therefore an electric heater stabilizes the temperature at -100°C . The camera consists of a CCD head mounted on the image intensifier and a controller box (ST-138). The head includes the LN_2 dewar and a preamplifier for the chip readout. The controller

contains the power supply, regulates the temperature, generates the clock signals for the readout and digitizes the signal. The image is read out at speed of 150,000 pixels/s and digitized with 16-bit precision. The analog-to-digital converter translates 5 photoelectrons into one count. The digitized data is transmitted via a high-speed serial line (TAXI) to the workstation controlling the beamline. A mechanical shutter in front of the CCD chip closes during the readout to avoid streaking of the image. Although the X-rays are normally off during readout the phosphor has an afterglow which is still seen on the strongest reflections after a few seconds.

A 10-keV X-ray photon absorbed in the scintillator creates about 400 visible photons. 200 of them are absorbed by the photo-cathode and 20 of them create photoelectrons. These are accelerated to 30 keV and then hit the phosphor. About 10% of the 600 keV the electrons deposit in the phosphor are converted into visible light with an average photon energy of 2.3 eV. Of these 25,000 emitted photons the optics with aperture f/1.4 can image about 6%. So about 1500 photons arrive at the CCD, of which 40% are detected, generating 600 photoelectrons. These are converted to a value of 120 AD counts after readout. One of the advantages of the image intensifier is that the gain factor, counts per photon, can be tuned. An adjustable iris in the optical system limits the amount of light collected by the CCD. If single photon detection is desired, it is fully opened. This setting had been used for the very first single bunch experiments. However, normally it is used with the aperture set to f/11, so the gain is about 1.8 AD counts per 10 keV photon to make better use of the available dynamic range of the CCD and ADC.

The detection quantum efficiency of the system is about 90% in the range 10-15 keV photon energy and falls off to about 30% at 30 keV [Moy 1994]. The point-spread function is 300 μm FWHM and 1.5 mm at a 0.1% level [Bourgeois *et al.* 1994].

The intensifier tube is sensitive to magnetic fields. It is protected by an anti-magnetic shielding (Soudupin, Paris, 55,000 F). It is made out of two layers of μ -metal 6 mm apart, which have been annealed in hydrogen atmosphere at 1000°C after machining. The inner one is optimized for highest permeability; the outer one has the highest saturation, but less permeability.

The shape of the entry windows causes a strong pincushion distortion of the image read out from the CCD, which has to be corrected by software in order to be able to index diffraction patterns. The photo cathode has to be spherical because of the requirements of electron optics. Electrostatic optics cannot image a plane surface on to a plane surface. Making the scintillator flat and the exit window curved would be impractical for the optics looking at the image on the exit window.

Calibration

The detector has to be calibrated regularly for spatial distortion and uniformity of response. Even after taking into account the distortion, the same X-ray flux per pixel gives a different reading depending on the position on the detector surface. The CCD itself is very uniform in response ($< 3\%$ non-uniformity). However, the imaging optics makes the intensity fall off from the center to the border of the detector because the effective aperture is smaller for off-axis rays, an effect called *vignetting*. Also the image intensifier is not uniform in response, especially after having suffered from radiation damage. The detector had been accidentally exposed to the direct white beam several times. As a result the glass of the exit window got grown by color centers generated by X-rays. Thus, the sensitivity is reduced in a blurred area of about 5% of the diameter close to the center. The beam also evaporated a small part of the photo-cathode, which leads to an insensitive area. This cannot be corrected for by calibration, but these spots are only a few pixels in diameter, close to or hidden behind the beam-stop.

The distortion correction is done with a calibration mask of copper with regular spaced holes. A scatterer is placed in the X-ray beam at the sample position and the mask is mounted in front of the entry window. The recorded shadow image reveals the pincushion distortion of the detector. An image processing software, FIT2D by Andrew Hammersley, analyzes the grid calibration image and interpolates the distortion between the grid points.

For the uniformity correction a flat field image with uniform illumination is required. There is no easy way to obtain a uniform X-ray illumination on a large enough surface from the tightly collimated synchrotron beam. We used a secondary X-ray fluorescence

source excited by the synchrotron beam. A 1 mm thick strontium-doped glass sample, excited just above its absorption edge at 16.10 keV, creates X-ray fluorescence of 14.2 keV photon energy. Under these conditions the sample shows maximal absorption for the primary beam and minimal for the isotropic fluorescence. Yet the illumination cannot be considered as uniform. The transmitted beam is still so strong that a beam stop has to be placed in front of the detector, the fluorescence is contaminated by a diffuse diffraction ring at the 10% level and falls off to the detector border as $1/r^2$. In practice, this is taken into account by recording the intensity distribution by an image, which is known to have uniform response. The latter is then used to correct the flat field image recorded by the image intensifier.

The X-ray image intensifier is an efficient detector for photon-count limited experiments. However, it needs constant re-calibration, which is time-consuming and remains unsatisfactory especially for polychromatic data. The high point-spread function and restricted useful diameter limit the quality of the data in the case of well-diffracting crystals such as PYP.

4.6 Femtosecond Laser System

The femtosecond laser system consists of three stages. The first is a Ti:Sapphire mode-locked laser producing weak 100 fs pulses of 800 nm at high repetition rate. This is used to seed a Ti:Sapphire chirped pulse amplifier which generates 100 fs pulses of about 0.5 mJ at 900 Hz. It is called a *regenerative amplifier* because it compensates for the reduced repetition rate by an increase in pulse energy, so input and output average power are roughly the same. The third stage is a frequency doubler and optical parametric amplifier (OPA) which can generate 460-760 nm pulses with 20-50 μ J energy.

The whole system had been assembled under the name *Alpha 1000* by *Brazard-Michellin Industries* (BMI) in Paris from October 1996 to January 1997 for 1,500,000 Francs. It was installed first at the ID4 diagnostics station of the ESRF in February 1997 and has been permanently installed at ID9 since November 1998. It is laid out on a 4.25 x 1.5 m² optical table. Key components such as the mode-locked oscillator *Mira*, its pump laser *Verdi* and the synchronization electronics were made by *Coherent*. The regenerative amplifier, frequency doubler and OPA are made of optical components spread out on the

table. Only the two pump lasers and the oscillator are encapsulated. The whole optical table is covered to protect the components against dust. A system of Plexiglas panels and covers forms ten compartments which can be opened individually.

The mode-locking in the Ti:Sapphire oscillator is caused by an increase of the refractive index of as function of the intensity (optical Kerr effect). The slit aperture in the beam stabilizes the mode-locking. For the high peak power of the fs pulses the Ti:Sapphire crystal acts like a weak focusing lens. So the mode-locked beam has a narrower beam waist than the cw beam.

Stretching the pulse before amplification is necessary because the high electric field of a 100 fs pulse would lead to non-linear effects. The pulse would start to self-focus in the Ti:Sapphire crystal or the Pockels cell of the amplifier as its power builds up, eventually exceeding the damage threshold of the material. Once the pulse has left the amplifier and is recompressed to 100 fs, self-focusing is not such a problem, because components working in transmission, such as beam splitters, lenses and non-linear crystals, are designed to be rather thin. However, in the amplifier it is unavoidable to send the pulse 8 to 12 times through 20 mm of Ti:Sapphire.

5 Experiments and Results

5.1 Instrumentation

5.1.1 On-line Microspectrometer

Part of this work was the development of a diagnostic which could in situ, on the X-ray diffractometer, verify the correct photo-triggering of the sample. This is done by measuring the absorption spectrum of the sample after the flash excitation at the same time delay as the X-ray pulse. From the characteristic spectroscopic fingerprint the photocycle state can be checked and the excitation degree estimated.

The setup had been designed with single crystal experiments in mind, but so far has been successfully used only for bacteriorhodopsin purple membrane. For single crystal absorption measurements, a tightly focused measurement beam is necessary. The optical probe beam has to be smaller than the smallest sample diameter, which is in the order of 100 μm for the myoglobin and PYP crystals used.

The design is based on a focusing spectrometer developed by Janos Hajdu in Oxford [Hadfield & Hajdu 1993].

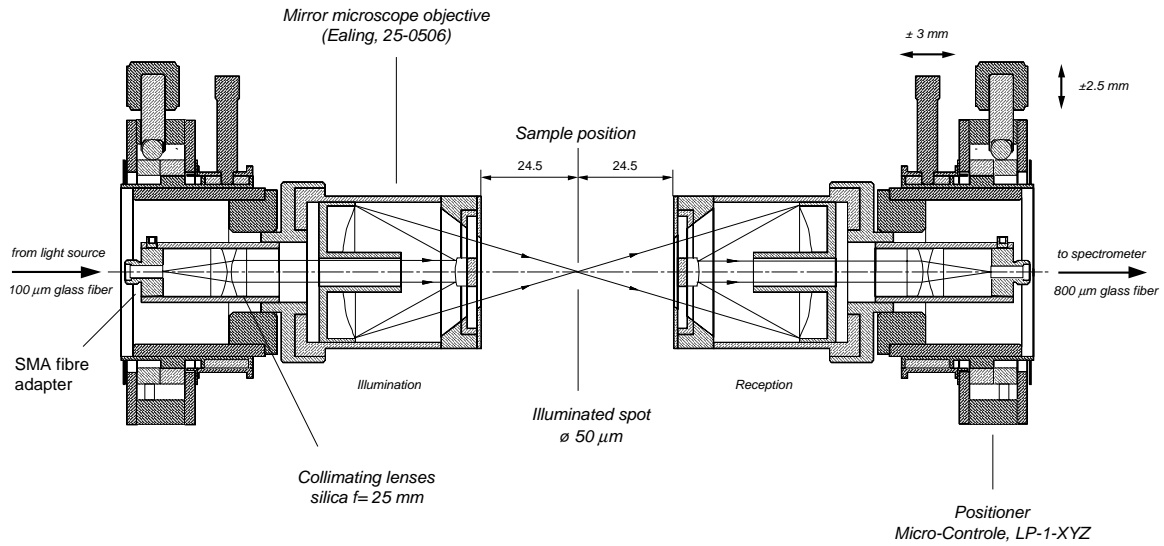


Figure 30: Illumination and pickup optics of microspectrophotometer

Mirror microscope objectives are free of chromatic aberration and allow large working distances at high numerical aperture.

The spectrometer consists of a sample illumination optic, a light source and a spectrograph. The sample illumination optic is a compact, lightweight unit that can be mounted on to an X-ray diffractometer and connected to the light source and spectrograph via optical fibers. It consists of two confocal microscope objectives. The sample position is their common focus. The use of mirror objectives avoids chromatic aberration at the sample point and the necessity of quartz optics to access the UV.

The reflecting microscope objectives are based on a design conceived by the German astronomer Karl Schwarzschild in 1904 for telescopes. It is a combination of a concave and a convex spherical mirror. Their radii have the ratio $(\sqrt{5} + 1)/(\sqrt{5} - 1)$ and they are assembled so their centers of curvature coincide. In this way their spherical aberration cancels out; aspherical surfaces can be avoided. Spherical optics are easier to polish and reach diffraction-limited performance with less effort. Another advantage of reflecting objectives is their long working distance of 24.5 mm.

The only sources of chromatic aberration are the collimation lenses for the optical fiber. These objectives are required to couple the optical fiber efficiently to the objective. The light emerging from the fiber end diverges into a cone of about 25°. Without collimation

the light would overflow the small mirror and only a small fraction could be refocused to the sample. With a focal length of 12.5 mm of the collimator and an effective focal length of 13.35 mm for the objective, the tip of the fiber is imaged at 1:1 scale to the measurement spot.

The time-resolution for kinetic measurements is achieved by using a flash lamp as light source. This source is a high-pressure Xenon lamp made by Oriel (model 6426), operated with up to 0.32 J of discharge energy, generating a white light pulse of 1 to 2 μs duration. It has a smooth spectrum in the visible range extending down to 300 nm in the UV.

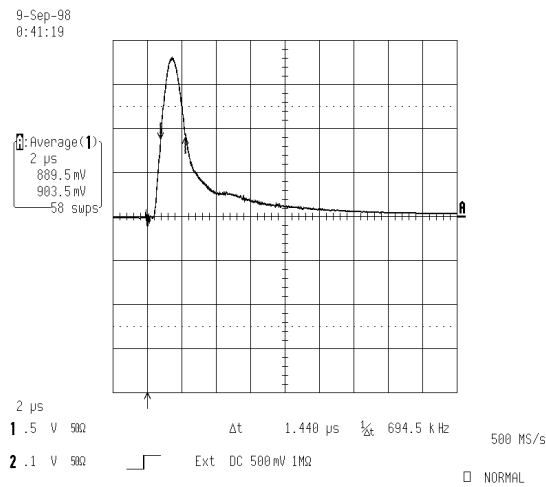


Figure 31: Pulse shape of the flash lamp

The probe light pulse has a duration of 1.4 μs FWHM (Oriel 6426 xenon flash lamp).

5.1.2 Femtosecond Spectrometer for Single Crystals

A time-resolved absorption spectrometer has been set up on the laser optical table. This instrument has been built for the preparation of and as diagnostics for time-resolved X-ray diffraction experiments. It has been designed for single crystals of Myoglobin, Photoactive Yellow Protein or Bacteriorhodopsin in the order of 100 μm in size, but there might be different applications in the future, to small molecule crystals or liquid jets.

It is important to answer the following questions before attempting an X-ray diffraction experiment:

- What is the optimal pump wavelength to get a maximum percentage of excitation of your sample?
- How much pump energy and how many pulses can the sample tolerate without showing damage or irreversible changes?
- What is the degree of photolysis or excitation under the conditions you would choose for the X-ray experiment?

A commonly used approach in laser spectroscopy is to send two time-delayed pulses through the sample, which originate from the same source and thus have a very reliable relative timing. The time delay is established by a mechanical delay line that alters the time of flight of one pulse to the sample.

Many spectrometers for femtosecond studies of proteins exist but they use beam sizes of a few millimeters and have been designed for liquid samples, which are large in volume and low in concentration compared to crystals.

A focusing spectrometer especially suited for small single crystals was designed by Janos Hajdu. However, it uses fiber optics and would not be compatible with fs pulses because of pulse broadening in the fibers and the inability of the fibers to withstand the power levels.

The spectrometer uses a small fraction of the 800 nm output of the Ti:Sapphire amplifier to generate fs white light pulses by a process called continuum generation. The laser beam is focused on to 2-mm thick Sapphire crystal. Due to the high intensity at the focal

point, non-linear processes that take over generate a smooth spectral distribution ranging from above 800 nm down to 460 nm.

The output of the compressor is not optimally compressed. In normal operation, the compressor is tuned to over-compensate the chirp generated by the stretcher. In this way the best performance for the frequency doubler and OPA is achieved. The pulse leaving the compressor has a slight negative chirp and steepens up to a transform-limited pulse by the temporal dispersion of the optics when it reaches the OPA. Unfortunately the compression, which would generate a stable continuum, would not allow operation of the OPA. The solution was to introduce optics which provide additional tunable temporal dispersion upstream of the continuum generation to compress the negatively-chirped pulse. This is done with a set of 5 mm thick zinc selenite (ZnSe) flats with anti-reflective coatings at 800 nm. ZnSe has a strong change of refractive index at this wavelength and introduces a temporal dispersion of 300 fs per cm for a 100 fs transform-limited pulse.

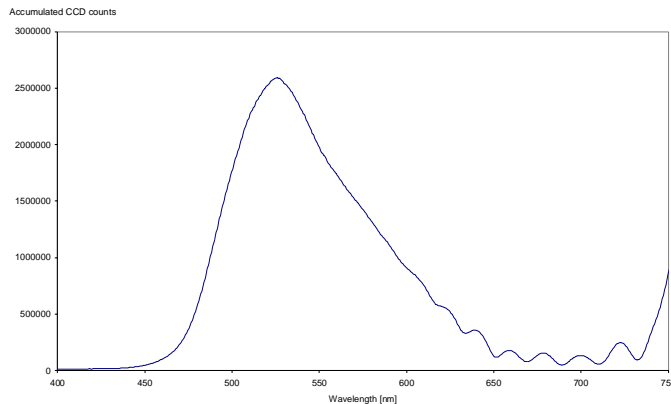


Figure 32: Femtosecond Continuum

This spectral distribution is obtained when focusing a 100 fs pulse of 800 nm in a 2-mm thick sapphire crystal.

the central part of the pulse where the intensity is highest, the refractive index is higher. Thus, the central part is retarded relative to the leading and trailing edge of the pulse. So the leading part is compressed and raised in frequency and the trailing part is expanded and lowered in frequency. Stimulated Raman scattering means that photon energy is partially transferred to high frequency lattice vibrations. Those, once excited, can then transfer energy back to other photons creating a blue-shifted continuum.

Continuum generation is a physical process, which is not yet completely understood. It is probably a combination of self-phase modulation and stimulated Raman scattering. Self-phase modulation is caused by the non-linearity of the refractive index. In the central part of the pulse where the intensity is highest, the refractive index is higher. Thus, the central part is retarded relative

The non-linearity of the refractive index leads to self-focusing of the beam at the focal point. It contracts to a filament with a diameter of the order of the wavelength which does not diverge as long as the intensity is high enough and the pulse is not stretched in length. A filament can contain a certain amount of energy. If the laser power is increased beyond a certain threshold, a second filament will be formed, grow in intensity to a limit then a third one will appear and so on.

A single-filament continuum is nearly a diffraction-limited source, which can be focused to a very small sample area. A variable attenuator adjusts the incident laser power to give a maximum of intensity and avoid multi-filament formation.

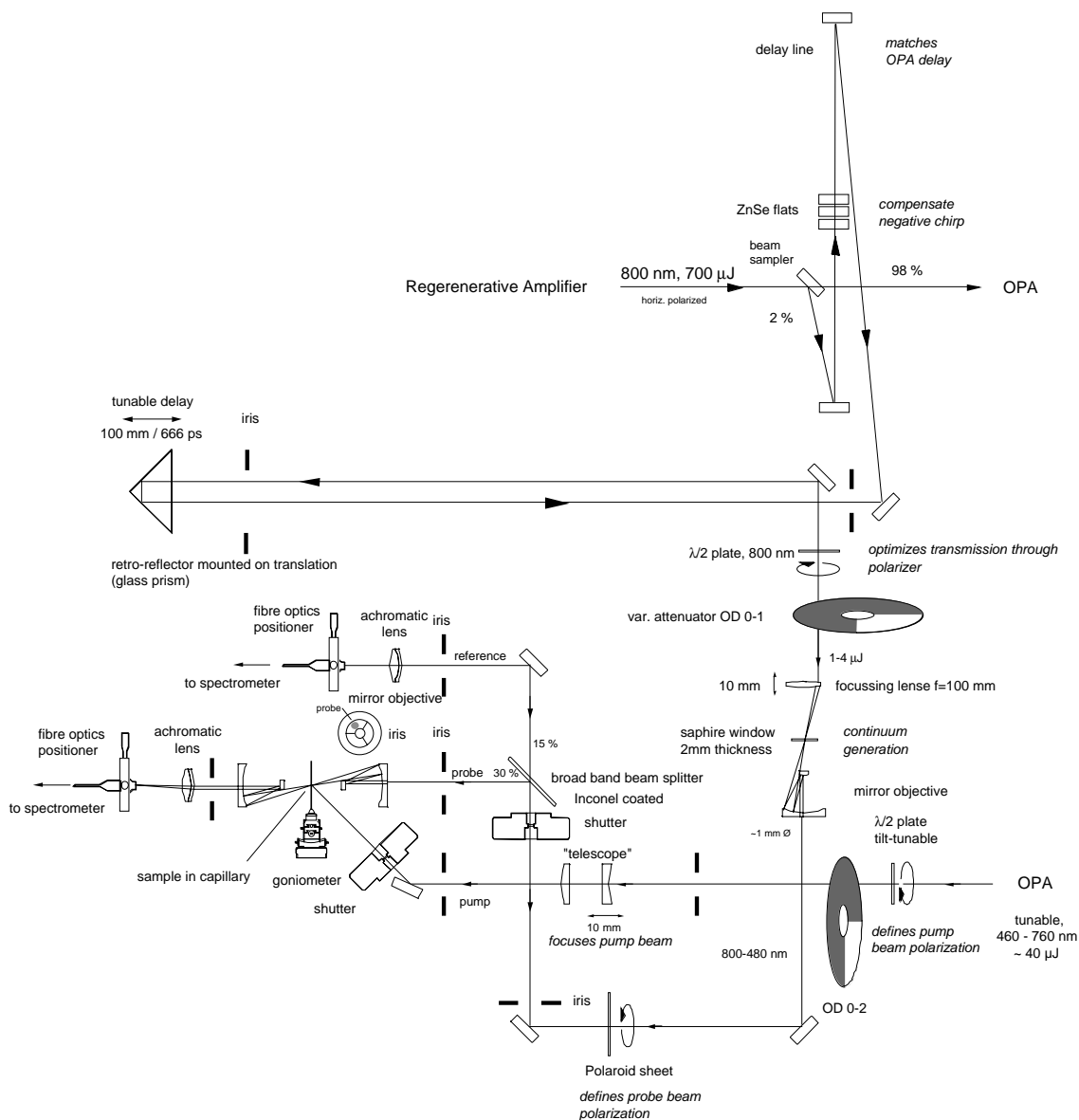


Figure 33: Layout of the femtosecond spectrometer

A Sapphire crystal was chosen because of its high damage threshold and the stability of the continuum. Continuum generation would also work in glass but it is much easier to damage. Even if the intensity stays below the damage threshold the focussed laser beam could locally alter the properties of the glass and make the continuum unstable or move the source point.

The continuum is imaged 1:1 to the sample by all-reflective optics so there is no chromatic aberration. The focusing optics is a “reflective microscope objective” made by

Ealing. Although it is made of two spherical mirrors it has no spherical aberration. The ratio of the two focal lengths and their distance are chosen so the spherical aberration cancels out.

Before the beam is sent to the sample a beam splitter sends half of it directly to the spectrometer. In this way transmission and a reference continuum spectrum can always be measured simultaneously. This is necessary because the unavoidable shot-to-shot fluctuations of the laser output not only alter the intensity but also the spectral distribution of the continuum. Both beams are focused into a 200- μm optical fiber cable and guided to a spectrograph installed off the optical table. At this point the pulse broadening by the fiber is not a problem because it happens after the sample.

The light is fed into the spectrograph by a multi-track fiber cable. It images the two fiber exits as separated traces on to a CCD chip.

Computer-controlled shutters block the pump or the probe beam selectively. The data acquisition program uses them to make reference measurements automatically, to eliminate systematic errors. For each transient spectrum three additional measurements are made: pump beam blocked, probe beam blocked and both beams blocked.

This work has been done in collaboration with Prof. Philip Anfinrud from Harvard University, starting in July 1997. He designed the general layout, the delay line, the continuum generation, the beam steering optics and the pump beam focussing. My contribution was the micro-focussing optics, the sample stage, the fiber optics, the spectrometer, the pump-probe shutters and the data acquisition software.

Table 2: Characteristics of Spectrometer

| | |
|---------------------|--|
| Probe beam size | < 10 μm |
| Pump beam size | 200 μm |
| Polarization | linear or circular |
| Spectral range | 760-460 nm |
| Spectral resolution | 5 nm |
| Time resolution | 200 fs |
| Time range | 0-666 ps, $n \cdot 1.1 \text{ ms}$ ($n=1,2,\dots$) |

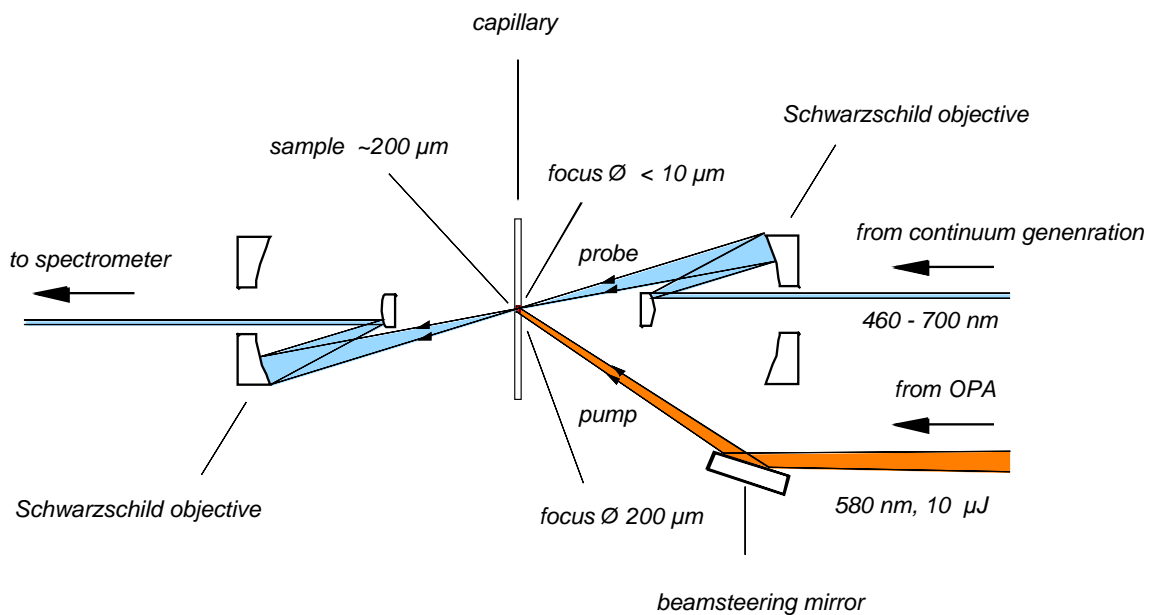


Figure 34: Sample environment in the femtosecond spectrometer

The pump beam overfloods the sample, a crystal of 100-200 μm size, whereas the probe is tightly focused. (Pump-probe setup as for MbCO, 22 Feb. 1998)

5.1.3 Laser to X-ray Timing Electronics

The time delay for laser-triggered X-ray experiments is continuously tunable from 100 ps to 45 s under software control.

The high precision is obtained by slaving the chopper and laser to the synchrotron *bunch clock* of 352.202 MHz. This is the radio frequency of the accelerating cavities of the ESRF storage ring. The actual round trip of the ring is by design 1/992 of this value.

The fs laser system is synchronized in two stages: The oscillator at 88 MHz and the amplifier at 897 Hz.

Most the timing control is built from modular radio frequency units, designed by Jean-Luc Revol for the needs of the ESRF machine group and maintained by Nicolas Michel [Michel 1996]. There are programmable divider units, programmable discrete phase shifter units and various interface cards. All these are Euro format cards that are inserted into a 19" rack with special back connectors. The power supply and an 8-bit address / 16-bit data bus for the programming of the cards on the backbone of the rack. The RF inputs and outputs on the front panel of the cards are interconnected by short 50 Ω coaxial cables with SMA connectors. The signal level used here is the standard for emitter coupled logic (ECL), -2V is defined a logical 0 and -1.2 V as logical 1. This standard is less common than TTL (0-5V) but has been chosen for best performance of transistors in switching time, because they can be operated at their highest sensitivity rather than in saturation. A peculiarity about the ECL level as these cards use it is that the ECL ground potential has been offset by -2V from the ground of the rest of the system and the mains. ECL outputs, when used with 50- Ω loads, need a termination voltage of -2V. Defining the ECL level of -2V as ground makes it easy to an oscilloscope where the shielding of the input is always grounded via the mains. So the actual levels you measure with a 50 Ω load by an oscilloscope are 0 and +0.8V [Blood 1988].

The programming of the units is done by an *S-Link* card installed in one of the slots of the rack, which receives commands from a serial line and sends address, data and handshake signals on the backbone. *Fast divider* and *fast delay* cards both use internally two 8-bit registers. However the actual division factor or delay is not a 16-bit value between 0 and 65535 but the product of two 8-bit values between 0 and 255 ranging from 0 to 64516. As an alternative to programming the boards via the backbone, they can

be configured by jumpers to fixed values. All the divider units are actually configured this way, because there is no need to change any frequencies during an experiment. The *fast delay* cards have an additional input for the clock rate, which is used as counting base for the programmed delay. Divider and delay units are usually arranged in pairs, so the clock rate before division is used as counting clock for the following delay unit.

The synchronization of the oscillator to an external clock is done by a computer-controlled system provided by *Coherent* called *Synchro-Lock 900* [Coherent 1996]. The *Mira 900* oscillator was designed for a pulse frequency of 76 MHz. However, at our request, Coherent modified it so we can use the 4th sub-harmonic of the bunch clock of 88.0504 MHz as a reference clock.

The oscillator is passively mode-locked. It does not have an acousto-optical modulator, which could be slaved to an external frequency source. The synchronization monitors the output pulse train with a photo diode, compares the signal with a reference clock and adjusts the cavity length. There are three active elements in the cavity which influence the round trip frequency and which are controlled by feedback loops with different time constants. At start-up a DC motor with 20-mm stroke translates one of the end mirrors until the difference between detected and reference frequencies is minimal. To compensate for slow thermal drifts there is a galvanometer with a mirror pair acting as a small optical delay line of 0.6 mm. To stabilize the cavity length against vibrations and mechanical resonances, another cavity mirror is mounted on a piezo-electric actuator with 8- μ m stroke, which can react to perturbations up to 5 kHz. The galvanometer is the same, as that used to initiate mode locking in the cavity when the laser starts up in cw mode. When the laser is synchronized to the 88 MHz clock, the electronics tries to switch to a feedback loop comparing the 9th harmonic of the laser repetition rate with the 9th harmonic of the reference clock to further reduce the phase jitter.

To obtain the reference clock, the 355 MHz sinusoidal RF signal is shaped into ECL pulses by a *distribution unit* and divided by 4 in a *fast divider* unit. The phase of this 88 MHz clock relative to the synchrotron can be adjusted over one period under computer control by an analog phase shifter. This module applies a variable phase shift to a sinusoidal input signal set by a 0 to 10V DC control voltage. It has been built by Nuclétudes in Paris to our specifications and contains 4 RC-filter units in series, each

containing a variable-capacity diode, which is biased by an external control voltage. The actual phase shift or time delay of the unit is a non-linear function of the control voltage. At 0 V the delay is maximal and decreases approximately linear with the voltage and goes into saturation at 10 V at a value of 12.7 ns. Since the output of the frequency divider unit is a (more or less) square pulse signal from 0 to 0.8 V, I inserted a 1:1 RF transformer between divider and phase shifter to remove the DC offset and filter the higher harmonics to get a sinusoidal signal. The unit is computer controlled by a 12-bit digital-to-analog converter (DAC) with 0 to 10 V output. The non-linearity is corrected by software. For five voltages between 0 and 10 V the delay between input and output is measured. From a calibration curve based on these support points the required control voltage for a given time delay is calculated by spline interpolation and programmed into the DAC.

The triggering of the regenerative amplifier was initially done at 898.47 Hz by a frequency divider built-in to the Pockels cell driver, which selects one out of 98000 pulses of the oscillator as seed pulse for amplification. I substituted this by the 98208 sub-harmonic of the oscillator, which falls together with the 396th sub-harmonic of the single bunch repetition rate of the synchrotron. This is the same frequency at which the X-ray chopper selects single bunches. This frequency is derived from the 88.0504 MHz reference clock by two division steps, 248 and 396. Two steps were required because the internal design of the *fast divider* unit does not allow a division by more than 64516. Because of the same limitation the programmable delay is implemented in two steps to cover the full range of 1.1 ms with 12.4 ns resolution.

The timing software decomposes a given delay into three ranges (0 to 1.1 ms in steps of 2.8 μ s, 0 to 2.8 μ s in steps of 12.4 ns and 0 to 12.4 ns) converts it to counts or volts and reprograms the appropriate hardware, analog or discrete phase shifters.

Table 3: Timing modules used at ID9

| | | | |
|-----------------------------------|---|---|---------------------------------------|
| Type | VPDU | Fast Delay Unit | Dephaseur D.88-360 |
| Design | ESRF, Thierry Le Caer, 1990 | ESRF, Jean-Luc Revol, 1992 | Nuclétudes, T. Francillon, 1998 |
| Resolution/ max. clock | 25 ns / 40 MHz | 1.8 ns / 540 MHz | ~5 ps |
| Range | 16.7 million clock cycles (0.524 ms @ 32 MHz) | 65276 clock cycles (185 μ s @ 355 MHz) | 13 ns |
| Control | VME bus | RS 232 serial line | analog voltage |

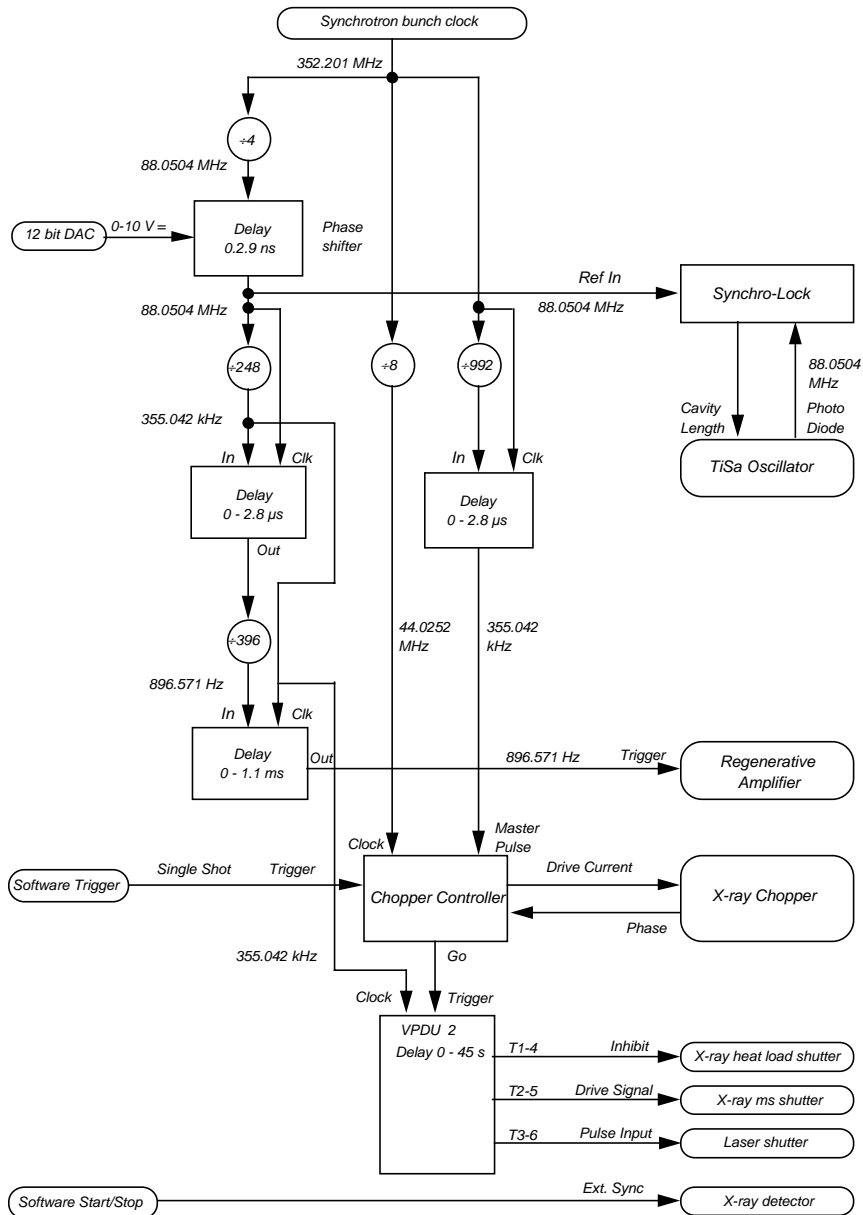


Figure 35: X-ray to Laser Synchronization

Schematic diagram of the clock signals (as of 4 Nov. 1998)

to within ± 700 ns precision to get any transmission, and should be precisely centered to optimize the transmission.

The phase tuning is done by applying a discrete electronic delay to the reference clock by a *fast delay* unit. Although the chopper controller has a built-in option for setting the phase, the *fast delay* unit has the advantage that the phase can be scanned in fine steps under software control. The controller detects the phase change of the external reference signal relative to the actual rotation phase of the chopper, and adjusts the latter within a delay of 1 to 20 seconds.

In practice, the phasing is done by programming a scan within *SPEC*, delaying the reference step by step by one more bunch clock cycle of 2.8 ns over the range of the 2.82- μ s single bunch round-trip time.

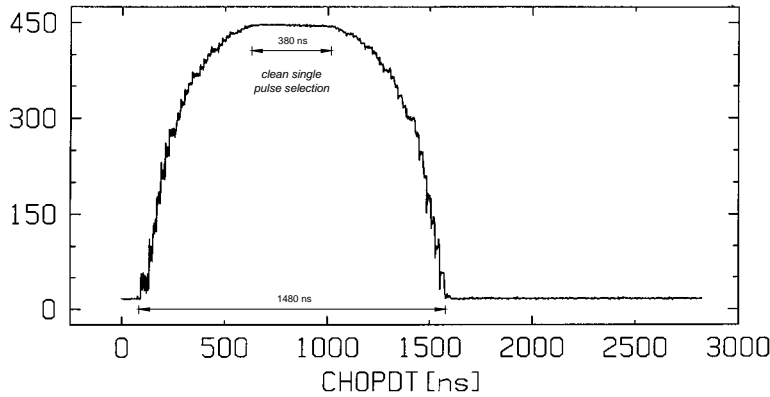


Figure 37: Chopper phasing in single bunch mode

X axis: phase of the chopper relative to the orbit clock, y axis: X-ray transmission of chopper (a.u.). The transmission was measured with an attenuated white beam of U26 (1 mm C + 0.5 mm Al), 13 mA, detector: Si PIN diode with current amplifier 10^4 V/A, 20 Jul 1998 (SPEC: "ascan chopdt 0 2816.57 991 0.1")

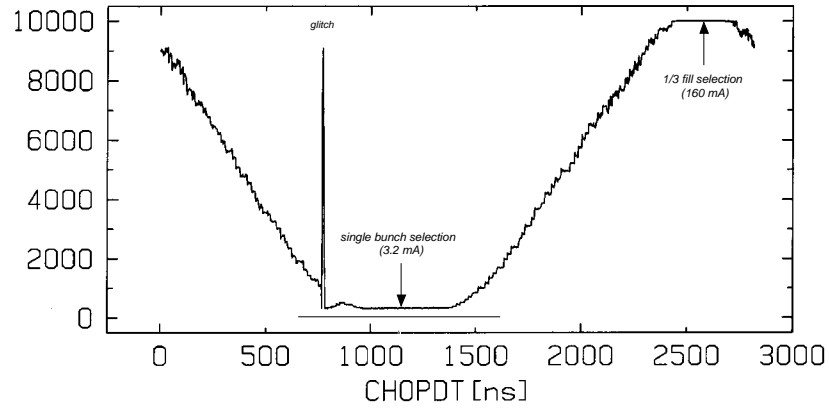


Figure 38: Chopper phasing in hybrid mode

The phase can alternatively be set to select a 100 ps single pulse or a 0.92 μ s square pulse. The glitch at 750 ns has nothing to do with the X-ray time structure. (1/3 fill current 160 mA, single bunch current 3.2 mA, 19 Jul 1998).

5.2 Experiments on Photosensitive Proteins

5.2.1 Myoglobin

Photolysis study

Ideally, before a time-resolved X-ray experiment with laser initiation is performed, it should be verified that the sample can be efficiently excited. This study was done actually after the first 100 ps Laue experiment on MbCO on 23 January 1999. The conditions were reproduced as accurately as possible in the offline microspectrometer. A 300- μm size myoglobin crystal mounted in an X-ray capillary was excited with 100 fs pulses of 10 μJ at a wavelength of 475 nm. The beam was circular polarized, focused to 200 μm diameter at an angle of 45° to the white probe beam. The polarization of the white probe beam was adjusted to find the minimum absorbance axis of the crystal. For this orientation, the peak absorbance of the sample was 0.7 at 540 nm and 0.3 at the photolysis wavelength of 475 nm. The spectra had to be averaged over hundreds of measurement for each time point to eliminate shot-to-shot fluctuations. After each time point the dial of the translation stage of the optical delay line was advanced to set a new time delay between pump and probe pulse.

Results

The series of transient absorption spectra in Figure 39 shows clearly the development of the characteristic difference features between deoxy and CO myoglobin shown in Figure 40. After 340 fs it is almost fully developed and changes further only slightly up to 10 ps. The transient spectra also reveal that there is no strong bleaching during the first 100 fs at any wavelength within accessible range. If such an effect existed, it would determine the optimal choice for the wavelength to maximize the penetration into the sample.

From the amplitude of the difference signal compared to the absolute absorbance of the sample, the excitation extent can be estimated to 16%. Another conclusion from this experiment is that even after the sample has received thousands of laser pulses, the

sample remains photoactive; there is no sign of irreversible damage nor of formation of met-myoglobin.

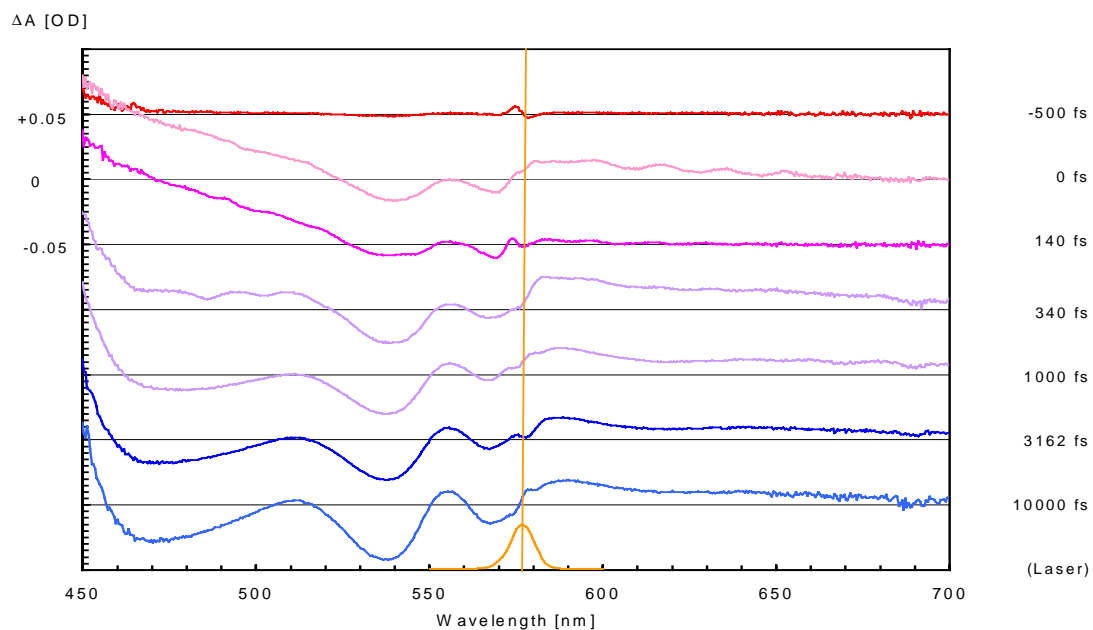


Figure 39: Evolution of the MbCO spectrum of after flash photolysis

These transient absorption spectra have been measured of a 300- μm size MbCO crystal (P2₁). Shown is the difference in absorbance relative to the spectrum of the unexcited sample. The top trace is shown as a reference only. Philip Anfinrud, ESRF, 23 Jan. 1998.

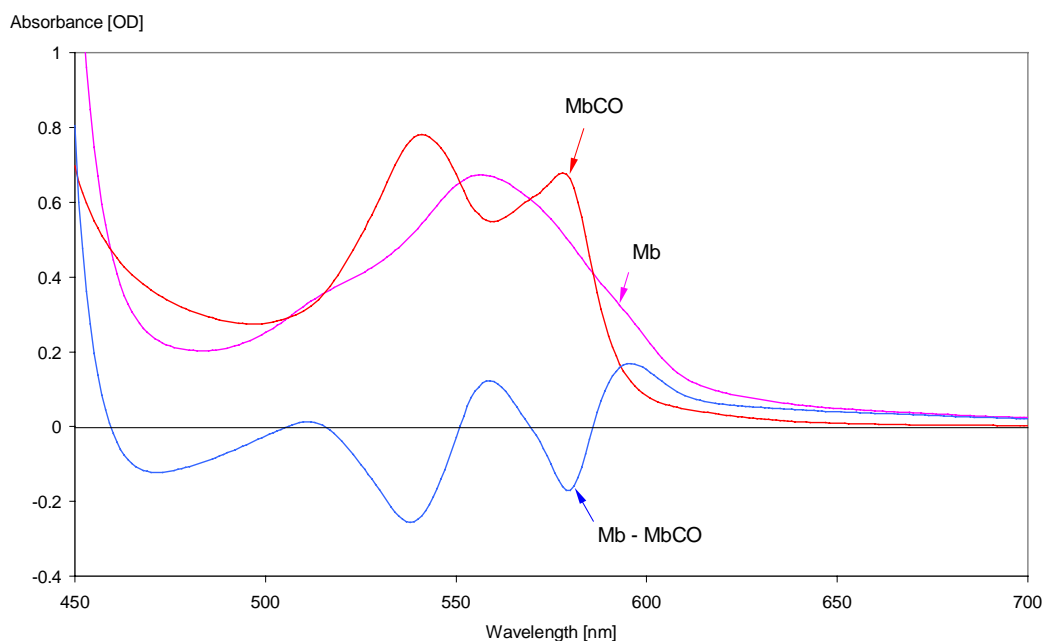


Figure 40: Difference between the MbCO and deoxy spectra in solution

The difference spectrum matches the signature observed in crystals 10 ps after ⁷³excitation. (Solution data provided by Philip Anfinrud, Harvard University, 1999)

Laue Diffraction

A series 100-ps time-resolved experiments were performed on myoglobin, starting on 14-22 Feb. 1998. The experiment was repeated on 3-6 Nov. 1998 and 17-22 Aug 1999 and finally succeeded on 12-16 Dec. 1999.

A small crystal of CO-ligated myoglobin is excited with a 100-fs laser pulse and a fraction of a nanosecond later its Laue diffraction pattern is recorded with a 100-ps long white X-ray pulse. To improve the photon statistics of the Laue image, this is repeated 64

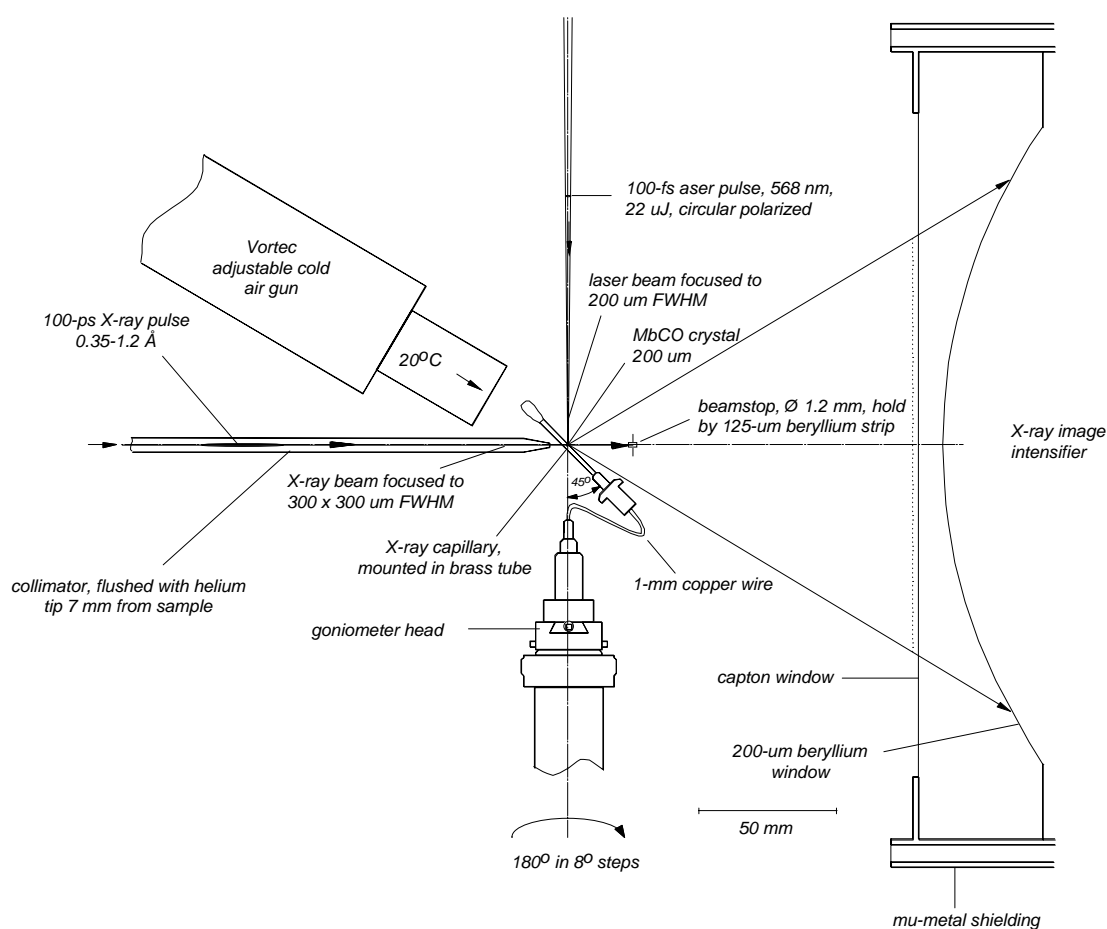


Figure 41: Single pulse Laue experiment on myoglobin

The exciting laser pulse arrives 500 ps ahead of the probing X-ray pulse. The laser excitation collinear to the rotation axis, together with the circular polarization, guarantees that the excitation degree is the same for all angular settings. Setup as of 5 Dec. 1999.

times before the X-ray detector is read out. To obtain a complete data set, it has to be repeated with different orientations of the crystal relative to the X-ray beam.

The sample was photolysed by a 100-fs pulse of 22 μJ energy and wavelength of 576 nm. This choice of wavelength is a compromise between uniform sample excitation and maximum absorbed energy. At longer wavelengths the beam would penetrate better into the sample and make the excitation more homogeneous. At shorter wavelength a larger fraction of the incident pulse energy would be absorbed. At 576 nm the optical density of the crystals used is about 1 (90 % absorption). This wavelength also takes advantage of the change in absorption caused by the photolysis to minimize the number of photons absorbed by already photolysed myoglobin. At 576 nm the absorption decrease has a local maximum of about 25 % (see Figure 40).

A pulse energy of 22 μJ was the maximum that could be obtained with the OPG/OPA system. Since there is only one photon per four myoglobin molecules for a 200- μm crystal, no further loss was tolerable by mismatch of beam and sample size. Thus the laser beam had to be focussed to 200 μm size and precisely centered on the sample.

For the sample excitation, a configuration was chosen, where the laser beam is perpendicular to the X-ray beam, collinear with the rotation axis of the diffractometer, and the capillary containing the sample is inclined by 45° against the axis. The advantage of this geometry is that the sample always exposes the same face towards the laser beam. So the penetration depth and sample excitation degree does not vary, when the sample is rotated during the X-ray data collection. The laser beam was circular polarized to ensure that the absorption is not affected by the dichroism of the crystal. To minimize reflection losses, the side of the crystal which sticks to the wall of the capillary was facing towards the laser beam. The fact that the capillary is inclined 45° against the laser beam does not significantly increase the reflection loss (2.8 % at normal incidence, 3.7 % at 45°).

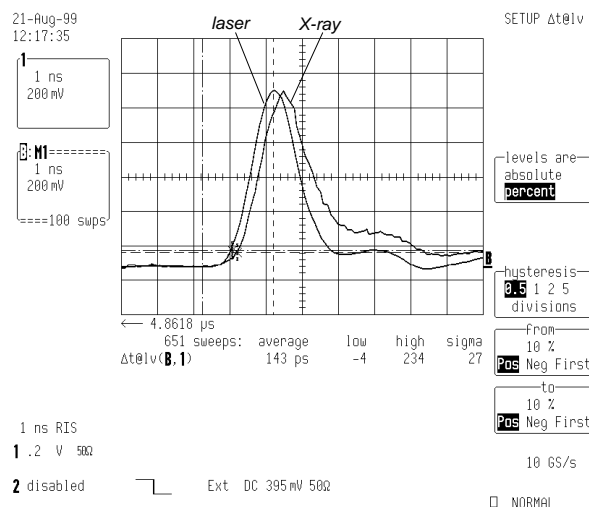


Figure 42: Laser to X-ray timing

Measurement of the relative timing of X-ray and laser pulse at the sample position with an avalanche diode detector. The laser pulse (stored in memory, trace B) arrives about 150 ps time ahead of the X-ray pulse (live signal, trace 1). The recorded signal shows the detector response rather than the true pulse shapes. The first signal has been recorded with the laser shutter open and the X-ray beam blocked the second one with the laser beam blacked and the X-ray shutter open.

A rather long focal length of 1.5 m was chosen for the laser beam to achieve a focal point of 200 μm diameter that is diffraction-limited. The advantage of using a diffraction-limited focus, rather than using a short focal length and placing the sample off focus, is that it is easier to obtain a smooth intensity distribution at the focal point. Inhomogeneties of the beam profile, introduced by optics upstream the sample, are washed out. The focal length of 1.5 m was obtained by a combination of a dispersing ($f = -175$ mm) and a focusing lens ($f = +240$ mm) in 85 mm distance. The beam diameter at the entry was about 8 mm and 12 mm at the exit, which would translate to a diffraction-limited focal spot diameter of 180 μm, if the beam quality is $M = 2$.

The experiment was performed with monoclinic crystals of CO-ligated myoglobin, prepared by Vukica Srajer at the University of Chicago. These crystals have a unit cell size of $a = 64.18$ Å, $b = 30.79$ Å, $c = 34.73$, $\alpha = \gamma = 90^\circ$, $\beta = 105.13^\circ$ and the space group

symmetry $P2_1$. Relatively small crystals of about 200 μm diameter were used, which have an absorption of around OD 1 at 576 nm.

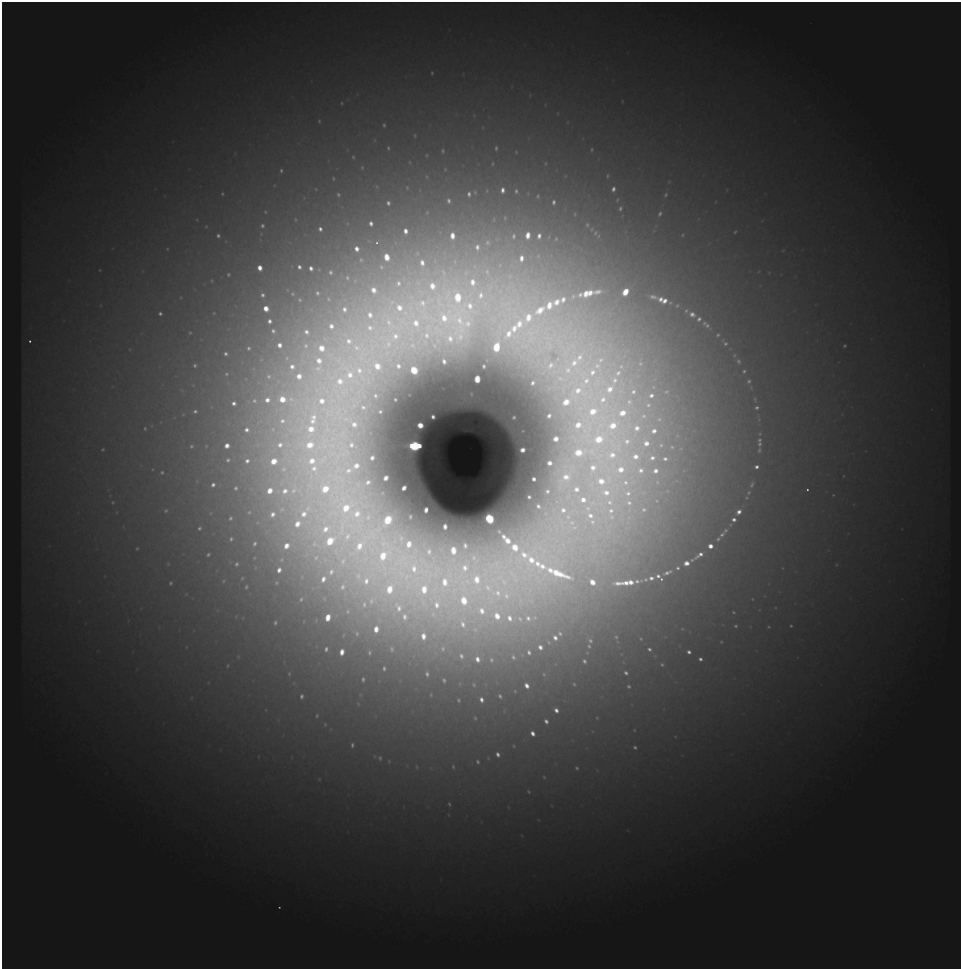


Figure 43: Laue diffraction pattern of a myoglobin crystal

64 single X-ray pulses with 500-ps time delay to the laser pulse are accumulated by detector at a repetition rate of 0.5 Hz. Detector: liquid-nitrogen cooled CCD with X-ray image intensifier, 125 mm distance, X-ray source: U46 and W70, image mb24_000_light.mar (16 Dec 1999, 21:56)

The X-ray diffraction data was collected over a range of 180° at 8° spacing. The 64 single X-ray pulses per image were accumulated on the detector at 0.5 Hz repetition rate to avoid heatload by the laser beam on the sample. For each crystal orientation a reference image was recorded beforehand without any laser excitation with the same number of X-ray pulses. This data collection strategy is advantageous for the calculation

of difference maps, because an isomorphous ground state data set from the same sample is available. Any radiation damage that builds up in the sample in the course of the data collection would not show up in the difference map, because its progress is the same in the photo-excited and the dark data set.

To maximize the X-ray flux, two insertion devices of the beamline were used in series, Wiggler W70 at 20.6 mm gap and Undulator U46 at 16.3 mm gap, which gives a broad spectrum ranging from 0.35 to 1.5 Å (8 to 35 keV) (see p. 30). To obtain a smoother spectrum, both insertion devices were used with a taper of 1 mm of the magnetic gap.

Results

The diffraction data were processed in Chicago by Vukica Srajer, using the *LaueView* software [Ren & Moffat 1995]. Only one out of five data sets recorded with 150 ps to

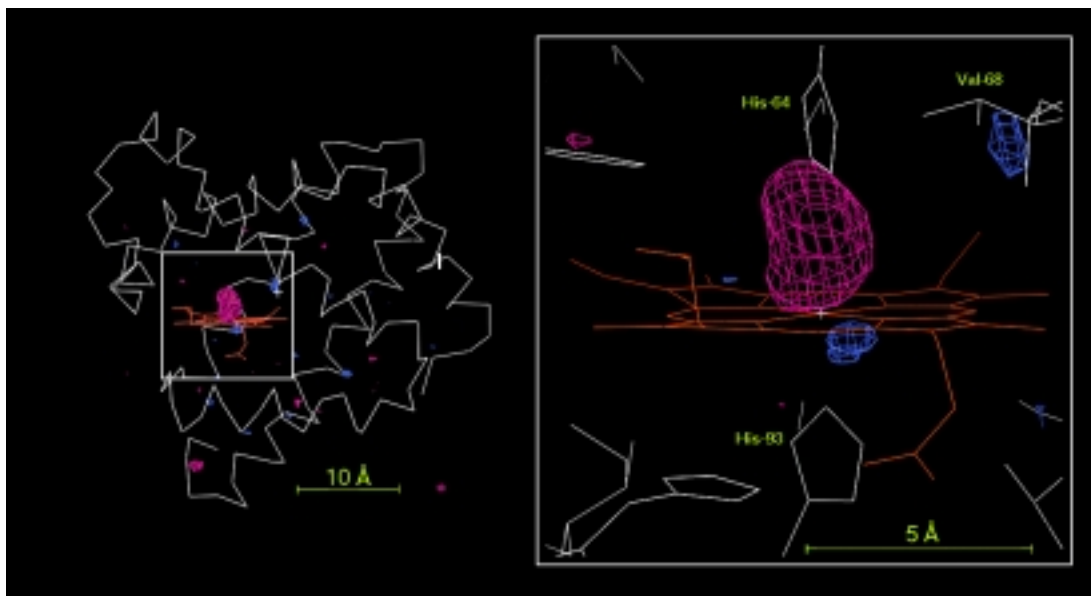


Figure 44: MbCO difference maps

500 ps time delay; weighted map, $Mb^* - MbCO$ contoured at -3.5σ (red) and $+3.5 \sigma$ (blue), 1.8 Å resolution, by Vukica Srajer, 2 Nov. 1999 (data set mb24, 16 Dec 1999, 21:50 - 0:30, Graphics by XtalView 3.2 © Duncan McRee)

500 ps time delay show significant features in the electron density map.

The difference map was calculated from about 10000 structure factor pairs up to 1.8 Å resolution, which were measured on average with 5-fold redundancy. The electron difference maps is calculated using a weighting scheme, which scales down structure factor differences based on error estimates [Srajer *et al.* 1996] [Ursby & Bourgeois 1997]. It uses experimental errors provided by the integration software for the photo-excited and ground state structure factors and assigns the difference structure factors a low weight if its error is large compared the average difference for a resolution shell of a certain width.

The map (Figure 44) shows the difference in electron density of the MbCO molecule 500 ps after the photolysis of the Fe-C bond relative to the state before photolysis. Inside the red regions the number of electrons decreases and inside the blue region it increases. The density is not given in absolute units as electrons / Å³, but in multiples of the standard derivation σ of the density map. The standard deviation is a measure for the experimental noise of map. I chose a level of 3.5 σ as significant in this case because there are only very few features at this level, which are randomly distributed over the map.

The dominant feature is the hole left by the CO at the binding site, with an amplitude of -8.9 σ . The positive peak below (-4.3 σ) can be interpreted as a movement of the iron atom out of the heme plane caused by the change of the coordination number from six to five when the Fe-C bond is broken. If there is a "docking site" for the CO inside the heme pocket where it stays for some time after the photolysis, one would expect a positive peak of similar amplitude and size as the negative peak at the CO binding site. The peak at the Valin-68 residue in 4.5-Å distance is probably too close to the protein backbone to be a docking site. The absence of a CO docking site feature can be interpreted in two ways. Either the CO has left the binding pocket or it is too delocalized in the docking to show up at the experimental noise level.

From the difference map the photolysis was estimated to be between 15 and 25 %. This estimation is based on the amplitude of the negative feature at the CO binding site. The number of electrons in the CO hole is compared with a theoretical difference map between the MbCO structure and the MbCO structure with the CO molecule removed. In order to make the two maps comparable, first two sets of theoretical structure factors are calculated, then truncated to the completeness of the experimental data set and scaled to

the experimental data set. Then the theoretical difference map is calculated using the same phases as for the experimental map for both sets of theoretical structure factors. Finally, the amplitude of the negative peak at the CO is measured in the two density maps (without scaling to σ) and their ratio is an estimate of the photolysis degree.

5.2.2 Photoactive Yellow Protein

Nanosecond Laue Diffraction

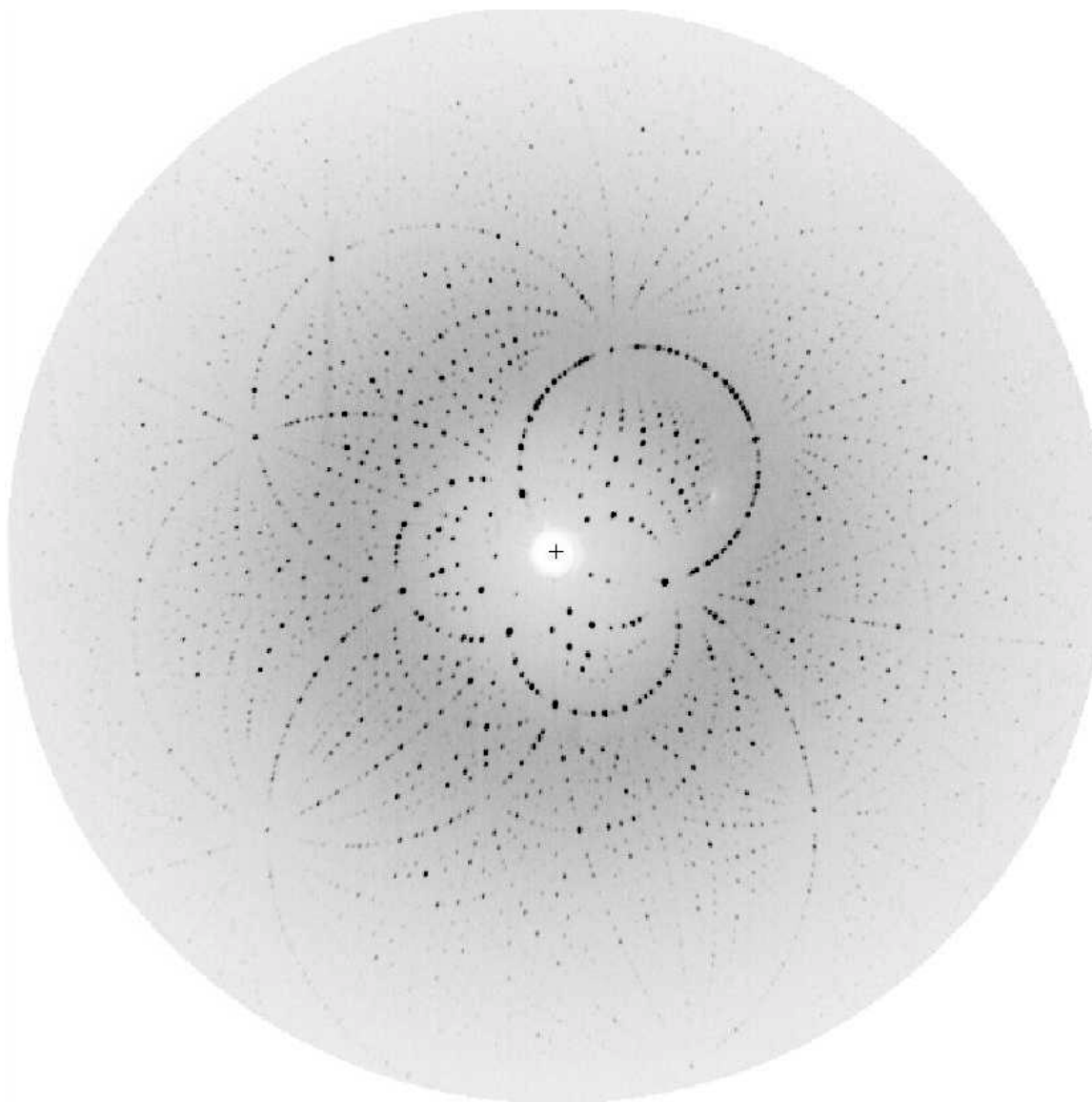


Figure 45: PYP pulsed Laue image

100x100x200 μm^3 crystal by Benjamin Perman, University of Chicago

Source W70, 20 mm gap, detector XR11 / CCD, 150 mm distance. For this image, 10 single pulses of 100 ps have been accumulated over 46 s. The X-ray pulse arrived 1 ns after the peak of the stimulating laser pulse of 7 ns. This image contains about 3700 useful reflections. (image pypb35_017, 27 Nov 1996 14:58).

This experiment was carried as collaboration between the group of Keith Moffat (University of Chicago) and the ESRF during a single day of single bunch beam time, 27 November 1996 (Experiment LS-540).

The PYP crystals were excited at a wavelength of 495 nm with laser pulses of 7 ns FWHM. These pulses were made by a Nd:YAG pumped dye laser. For this experiment the laser dye Coumarin 500 was pumped by the third harmonic of the Nd:YAG laser, 355 nm. The output of the dye laser, 11 mJ per pulse, was injected into an optical fiber of 1 mm diameter and guided to the diffractometer over 6 m distance. At the output of the fiber the light was refocused to the sample by a lens into a spot of about 1.5 mm in diameter, which contained a pulse energy of 4 mJ.

The crystals were mounted in sealed X-ray capillaries. During the experiment the sample was in a cooled air stream of 8 °C in the X-ray diffractometer.

To isolate single X-ray pulses, the prototype X-ray chopper by Wilfried Schildkamp (see p. 40) was used. The timing between the exciting laser and probing X-ray pulse was verified by an avalanche diode (Hamamatsu S2384) placed at the sample position. Data sets at time delays 1 ns, 5 ns, 10 ns, 59 ns and 422 ns were collected in single bunch mode with 100 ps X-ray pulses; and at time delays of 1.5 μ s, 8 μ s, 50 μ s and 350 μ s in 1/3 filling mode on 24 November with 0.9 μ s X-ray pulses. The data was collected with laser excitation alternating on and off, recording two images at the same orientation of the goniometer spindle. For each image 10 pulses were accumulated before the detector was read out.

The crystals were grown by Benjamin Perman at the University of Chicago from material provided by Klaas Hellingwerf, University of Amsterdam. The crystals are hexagonal, have a unit cell of $a = b = 66.9 \text{ \AA}$, $c = 40.8 \text{ \AA}$, $\alpha = \beta = 90^\circ$ and $\gamma = 120^\circ$ and space group $P6_3$.

Results

The data have been processed by Ben Perman at the University of Chicago, using the *LaueView* software by Zhong Ren. The electron difference maps were calculated using the experimentally measured Laue structure amplitudes of the ground state as reference.

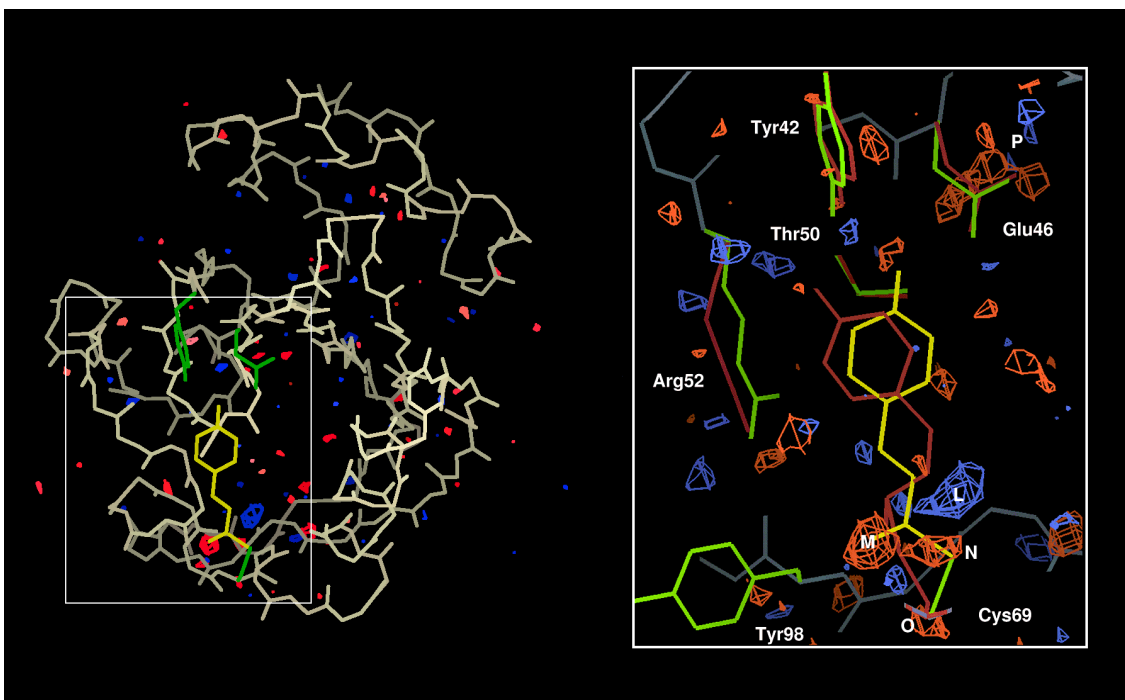


Figure 46: 1-ns difference map of PYP

In blue regions the electrons density electron density increases relative to the ground state, in red regions it decreases. Contoured at 2.6σ . Right: Modeling of excited state, by Benjamin Perman, PDB 2PYR [Perman et al. 1998]. (Graphics by XtalView 3.2 © Duncan McRee)

The phases for the structure factors were taken from the ground state model, omitting the chromophore.

The electron difference map, contoured at 4σ , is empty for most of the protein and shows strong features only close to the chromophore. Of the chromophore, the aromatic head group does not show strong displacement. There is a negative hole (feature *M*) at the place of the carbonyl oxygen of the thioester bond and a positive peak (feature *L*) at the opposite side of the chain.

Picosecond Laue Diffraction

On PYP a series of three 100-ps time resolved experiment was performed in collaboration with the groups of Keith Moffat and Elizabeth Getzoff and Philip Anfinrud

(9-21 July 1998, 3-6 Nov. 1998, 29 June - 2 July 1999). The experimental setup was very similar to the one for myoglobin (see p. 74).

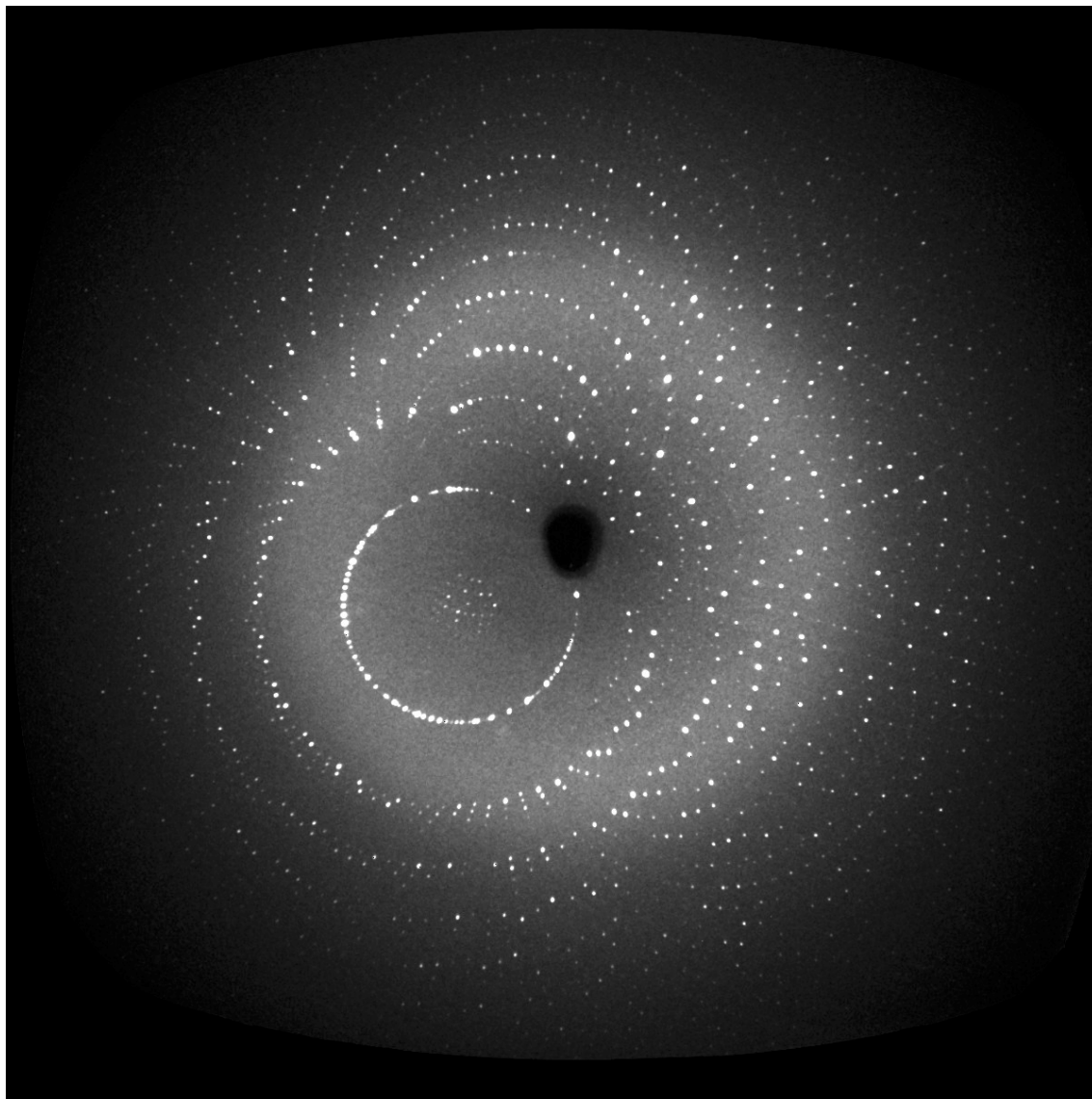


Figure 47: Laue diffraction of a PYP crystal 100 ps after laser excitation

Source Undulator-26, ID09, 23 Nov. 1998, File: pyp123_001.mar

For the sample excitation 100-fs pulses of 400 nm wavelength with 50 μ J were used. Although this experiment was repeated several times, the electron density maps never showed any significant difference before and after laser excitation.

5.2.3 Bacteriorhodopsin Purple Membrane

In the absence of suitable crystals for Laue diffraction, time-resolved studies on bacteriorhodopsin were done on purple membrane samples. From these samples, powder diffraction images can be recorded with a monochromatic X-ray beam. From the intensity change of powder diffraction rings after photo-excitation, low-resolution electron density difference maps can be calculated.

This experiment was performed, like the Laue experiments, in a stroboscopic way. The time-resolution is given by the X-ray pulse duration used and does not depend on the response time and read-out speed of the detector. The readout time for the XRII/CCD detector is 9.2 s, but the time-resolution is 2 ms. For this experiment a chopped X-ray beam was used. The arrival of the 2-ms X-ray pulses was timed to the flash excitation of the sample. In this way 500 pulsed powder diffraction images were accumulated at a 1 Hz repetition rate on the detector.

Sample Preparation

The sample was prepared from purple membrane solution with a concentration of 13.7 mg/ml, (obtained from Anne Cousin, Forschungszentrum Jülich, sample S9). 50 μ l of this solution was distributed over an area of 15 mm diameter on a mica sample carrier and dried for 10 minutes under a stream of dry nitrogen. Then it was moistened with water vapor and covered with a second piece of mica with vacuum grease applied at the border. It was pressed on to the sample with a minimum amount of air included, the grease forming a watertight seal around the sample. The optical density at 570 nm of the samples obtained this way lay between 1.7 and 2.

Thin mica was chosen as a sample carrier, because it is transparent to X-rays and light, and not permeable to water vapor. It does not show X-ray small angle scattering nor diffuse diffraction rings, because it is a crystalline material. The mica carriers used are disks of 30-mm diameter with a thickness of 12-15 μ m, made by Möricke, Berlin.

It is important that the sample cannot dry out during the experiment, because dehydrated bacteriorhodopsin does not retain the natural photocycle [Thiedemann 1994]. An

indication for too dry samples would be a prolonged M state, with a lifetime up to 100 ms or even 1 s. Kinetic absorption measurements made on the sealed samples (Figure 48) show the normal decay time of 5 ms of the M state, so it can be concluded that the purple membrane is fully hydrated.

Excitation

The sample was excited by 0.7-ms yellow light flashes from a Xenon flash made by Gerd Rapp in Hamburg. This device was designed for flash photolysis of caged-compounds by UV light. It has a slot for inserting optical filters, normally used for a solar-blind filter. I inserted a yellow filter instead to remove the blue and UV part of the white Xenon flash. The light was injected into a fiber optical cable, guided to the X-ray diffractometer focused onto 2-mm spot of the sample and with a lens at the end of the fiber. A preparation experiment showed that a small fraction of the available flash power is sufficient to saturate the excitation of the sample. For this experiment, the flash lamp power supply was set to the minimum capacity of $C_1 = 1470 \mu\text{F}$, charged to 220 V.

The use of yellow light and the length of the pulse help to efficiently synchronize the sample in the M state. Because the color turns to yellow in the M state, the sample gets more transparent for the excitation light and light driven back-reactions from the M state to the ground state, which would shortcut the normal photocycle, do not play any role. Since the flash duration is significantly longer than the lifetime of all the earlier intermediates, those molecules, which fall back to the ground state, can be excited again.

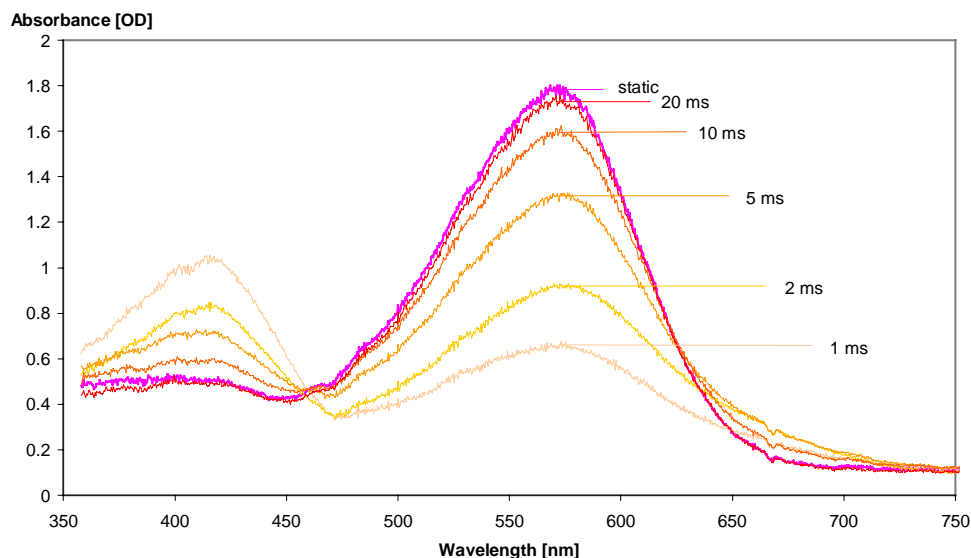


Figure 48: Offline measurement of the sample excitation

The 5 ms decay of the M state shows that the sample is fully hydrated and performs its normal photocycle (30 Sep 1998, 21:35-22:06).

These measurements were done offline before the X-ray experiment. A 1.4- μ s flash lamp (see chapter 5.1.1) was used as light source, which was synchronized to the excitation flash lamp by variable a delay generator (Philips PM 5785). No time points earlier than 1 ms can be measured, because of the duration of the excitation pulse. The stray light of latter would eclipse the measurement flash. Also, the CCD of the spectrograph has to be timed carefully so that charges generated by the stay light of the excitation flash are cleaned off the chip before the measurement pulse is recorded.

X-ray data collection

For the X-ray experiment a mechanical shutter generated 2-ms X-ray pulses. This device is a modified laser beam shutter made by *NM Laser Products*, California [Woodruff 1991]. It contains a lightweight magnetic blade, absorbing the beam at shallow angle of 11° . It can be actuated

into a horizontal position by an electromagnet within less than a millisecond, letting the beam pass through a 2.3 mm high aperture. In pulsed operation an opening time as short as 1.4 ms can be achieved. The modification for X-ray usage consists of adding a 0.5-mm tungsten coating to the blade and adding apertures made of lead.

The X-ray shutter and the excitation flash lamp were synchronized using a VME programmable delay unit (VPDU), generating a synchronized sequence of TTL trigger pulses. Although the photocycle of bacteriorhodopsin would allow a repetition rate of 10 Hz without problem, data was accumulated at 1 Hz. At higher frequencies the power supply of the flash lamp would overheat and shut down.

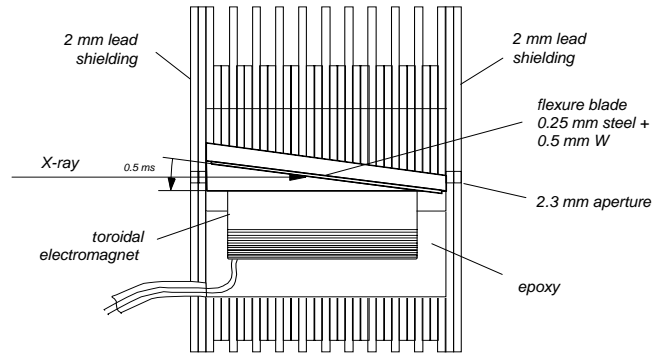


Figure 49: Millisecond X-ray shutter

Modified laser shutter by NM Laser Products, California, model LZ33ANC

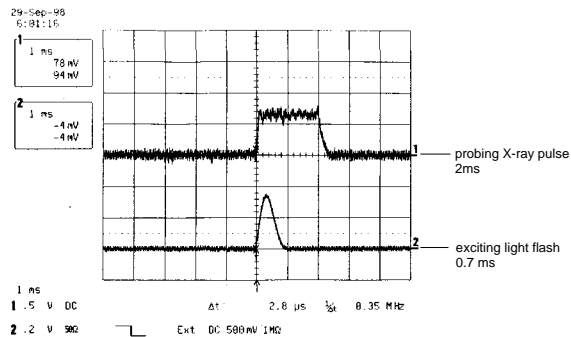


Figure 50: Timing of light flash and X-rays

X-ray recorded with S-PIN diode, current amplifier 10^3 V/A,

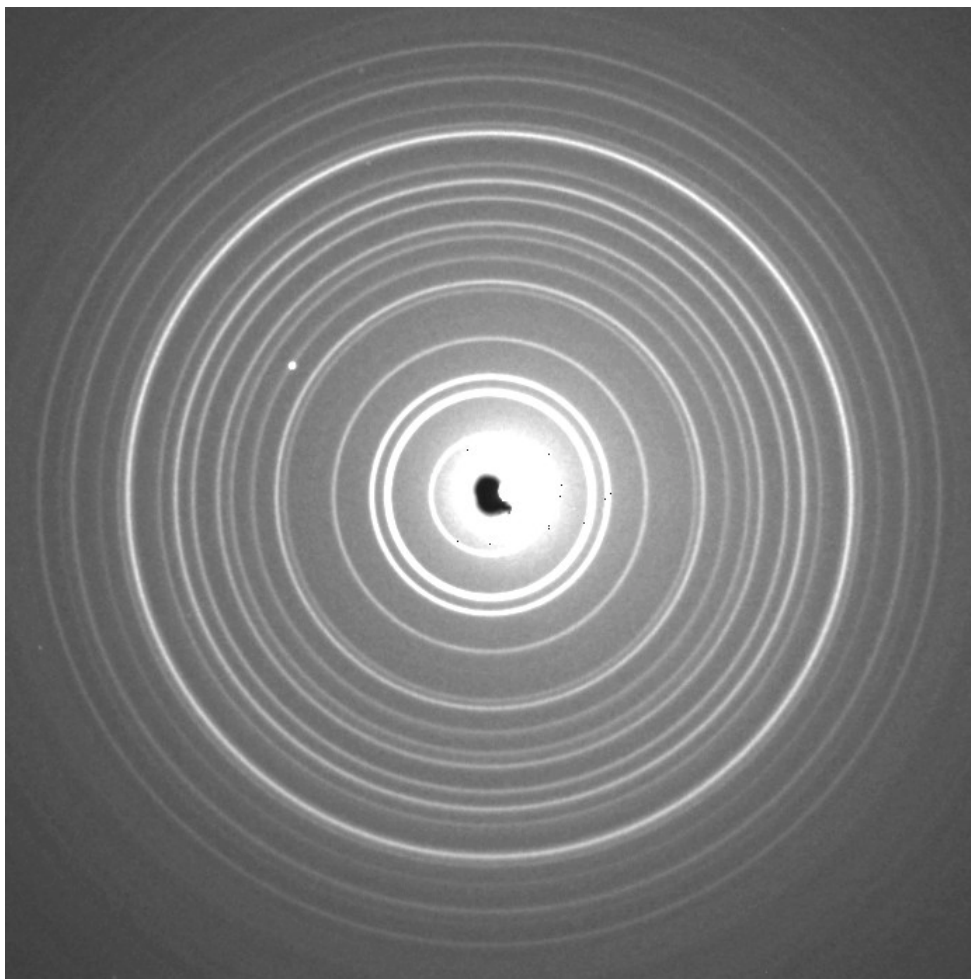


Figure 51: Diffraction pattern of purple membrane

This image was obtained by accumulating 500 X-ray pulses of 2 ms duration at 1 Hz repetition rate on the CCD detector. Each X-ray pulse was preceded by a 0.7 ms yellow flash. 500 seconds were needed to obtain this image. File: br3_0-2ms.mar, 1 Oct. 98, detector: X-ray image intensifier with liquid-nitrogen cooled CCD.

The insertion device used for this experiment was the undulator U26 with the gap set to 20 mm. The monochromator was set to the peak spectral brilliance at 12.0 keV (1.033 Å wavelength). With a synchrotron current of 75 mA in 16-bunch mode, a monochromatic photon flux of $1.5 \cdot 10^{12}$ photons/s could be obtained, focused to $0.5 \times 0.5 \text{ mm}^2$ FWHM at the sample. The undulator actually had its highest brilliance at its minimum gap of 16.9

mm at 11.5 keV. However, there would not have been any gain; the heatload on the monochromator would have been too high. The reflectivity loss by the heat-induced strain is stronger than the gain in spectral brilliance. Each 2-ms opening of the shutter sends a pulse of $3 \cdot 10^9$ photons to the sample. Then the diffraction pattern is accumulated for 500 pulses, so the number of photons used for one image is $1.5 \cdot 10^{12}$, equivalent to 1 s of continuous exposure.

For each image, a reference image without flash excitation was recorded with a chopped X-ray beam and the same number of pulses. This was repeated six times, also with different time windows of 0-0.5 ms and 2-4 ms. This showed that the observed changes in the diffraction ring intensities are reproducible and there is no long term change that would indicate sample degradation. Although 14 measurements were made on the same spot of the sample there was no sign of degradation, no color change and no decay of the diffraction pattern. Once when the X-ray shutter was left open accidentally for 10 minutes a white spot was created where the sample was exposed to the beam.

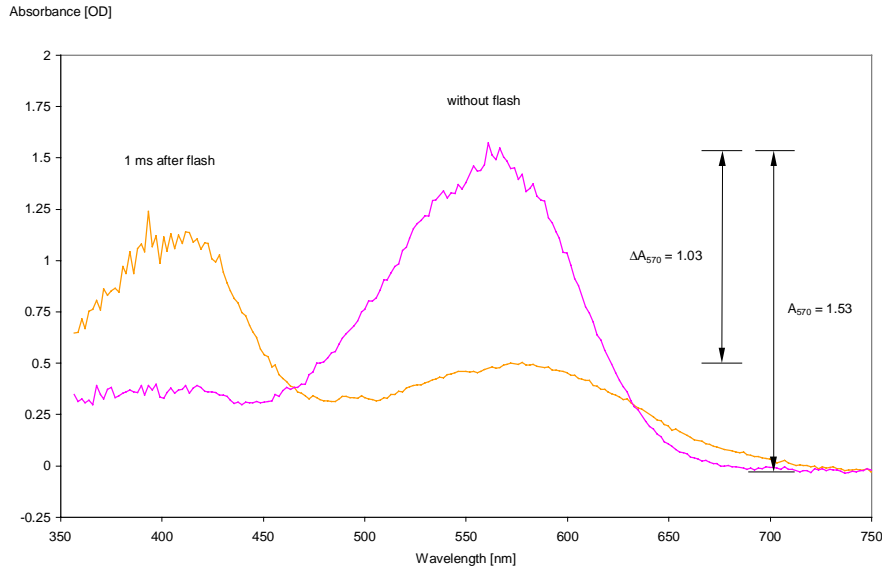


Figure 52: Online measurement of the sample excitation

These spectra were measured with the online spectrometer mounted on the X-ray diffractometer. The 1-ms spectrum is a single shot measurement during X-ray data collection, The excitation degree is $\Delta A_{570}/A_{570} = 1.03/1.53 = 0.67$. (files: online.dat, static.dat, 14 Oct 1998, 8:34).

To verify the sample excitation, the transient absorption spectrum was measured online with the spectrometer mounted on the X-ray diffractometer. From the spectrum shown in Figure 52 the excitation degree can be estimated. Based on the assumption that the peak at 570 nm would completely disappear if the sample were completely converted to the M state, and on the observed drop of the absorbance at this wavelength of 67%, the excitation degree is 67%. The measurement occurred in the middle of the 2 ms X-ray exposure time.

Data Processing

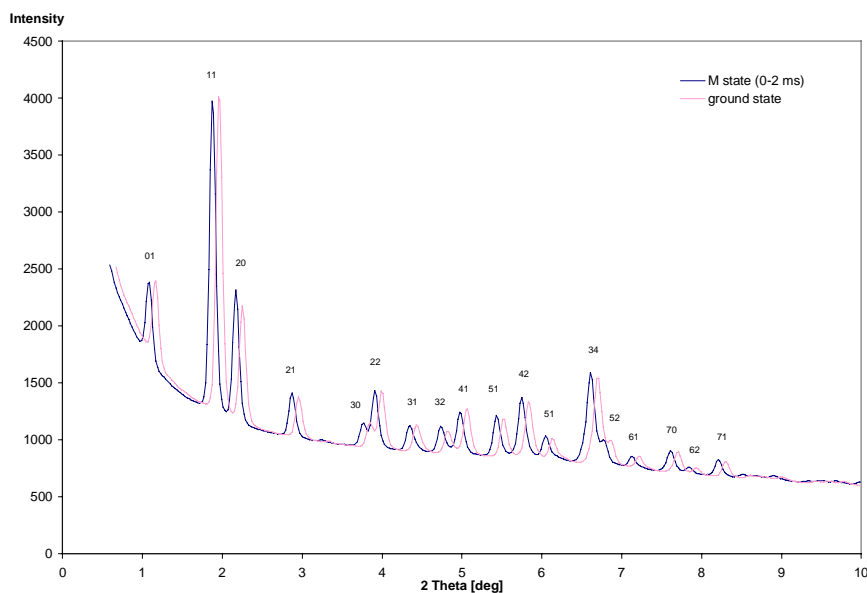


Figure 53: Circular integrated diffraction patterns

The ground state data is plotted with a small 2 Theta offset so the difference in peak height is easier to see. (Data files: br3_0-2ms.mar, br_3_0-2ms_ref.mar, 1 Oct 98)

The image read out from the CCD was corrected online for the distortion and non-uniformity of the X-ray image intensifier (see p. 51). The powder diffraction pattern was circular integrated using the software FIT2D by Andy Hammersley. The resulting radial profile was normalized to be equivalent to a 2θ -scan with a point detector.

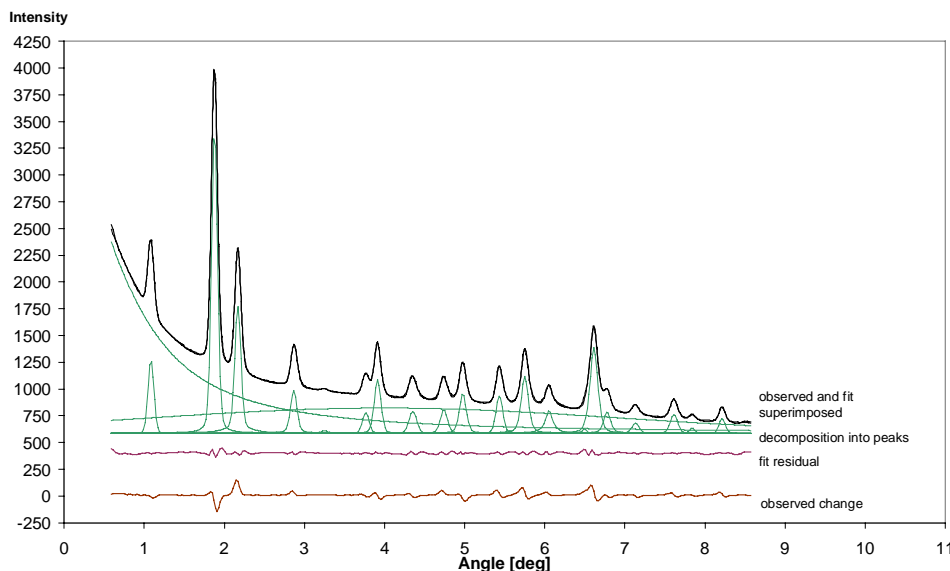


Figure 54: Decomposition of the diffraction pattern

Profile fit based on asymmetric pseudo-Voigt profiles.

From the experimental profile the powder ring intensities were extracted by profile fitting. The observed peak height changes only 6% on average. Standard powder diffraction programs, such as GSAS or FullProf, did not give good fits for the bacteriorhodopsin powder diffraction pattern. These programs assume that there is a systematic variation of the peak shape parameters with the diffraction angle. Although the peak width does increase with increasing diffraction angle, there are individual variations from peak to peak, which GSAS and FullProf cannot model. Finally, the data was processed with a general data analysis program, *Microcal Origin* (version 5). It has a built-in non-linear least square fitter (NLSQ), which can decompose 1D-data on the base of a large library of peak functions. The shape parameters for individual peaks do not have to be coupled but can be refined individually. The profile function I used was not part of the *Origin* library. I provided it as external code library written in C programming language. It is a combination of a Gaussian and Lorentzian profile (a pseudo-Voigt profile) which is allowed a different width parameter for the left and right side, in order to model the asymmetry of the observed peaks. The measure for the intensity is the peak area. Table 4 summarizes the result of the fit for a light-excited and a static powder pattern.

Table 4: Integrated ring intensities from purple membrane

| h | k | Mult. | I (0-2ms) | I (ref) | ΔI | $\Delta I/I$ |
|---|---|-------|---------------------|---------------------|-------------------------|--------------------------------------|
| 1 | 0 | 1 | 64.6 \pm 0.5 | 67.9 \pm 0.6 | -3.3 \pm 0.8 | -0.05 |
| 1 | 1 | 1 | 295.7 \pm 0.5 | 315.3 \pm 0.6 | -19.5 \pm 0.8 | -0.06 |
| 2 | 0 | 1 | 143.9 \pm 0.6 | 131.6 \pm 0.7 | 12.2 \pm 0.9 | 0.09 |
| 2 | 1 | 2 | 46.8 \pm 0.6 | 44.1 \pm 0.7 | 2.7 \pm 0.9 | 0.06 |
| 3 | 0 | 1 | 2.1 \pm 0.5 | 0.5 \pm 0.6 | 1.6 \pm 0.8 | 2.90 |
| 2 | 2 | 1 | 19.6 \pm 0.5 | 20.6 \pm 0.6 | -0.9 \pm 0.8 | -0.05 |
| 3 | 1 | 2 | 56.2 \pm 0.5 | 58.0 \pm 0.7 | -1.8 \pm 0.9 | -0.03 |
| 4 | 0 | 1 | 24.5 \pm 0.5 | 25.4 \pm 0.7 | -0.9 \pm 0.9 | -0.04 |
| 3 | 2 | 2 | 25.4 \pm 0.5 | 21.2 \pm 0.7 | 4.2 \pm 0.9 | 0.20 |
| 4 | 1 | 2 | 44.8 \pm 0.6 | 50.0 \pm 0.7 | -5.1 \pm 0.9 | -0.10 |
| 5 | 0 | 1 | 38.4 \pm 0.5 | 36.9 \pm 0.7 | 1.5 \pm 0.8 | 0.04 |
| 4 | 2 | 2 | 71.6 \pm 0.6 | 69.1 \pm 0.8 | 2.5 \pm 1.0 | 0.04 |
| 5 | 1 | 2 | 34.9 \pm 0.8 | 31.2 \pm 0.9 | 3.7 \pm 1.2 | 0.12 |
| 4 | 3 | 3 | 113.9 \pm 0.6 | 113.0 \pm 0.8 | 1.0 \pm 1.0 | 0.01 |
| 5 | 2 | 2 | 26.5 \pm 0.6 | 26.5 \pm 0.8 | -0.1 \pm 1.0 | 0.00 |
| 6 | 1 | 2 | 11.3 \pm 0.6 | 11.8 \pm 0.7 | -0.4 \pm 0.9 | -0.04 |
| 7 | 0 | 1 | 21.4 \pm 0.6 | 20.5 \pm 0.8 | 0.9 \pm 1.0 | 0.04 |
| 6 | 2 | 2 | 3.6 \pm 0.4 | 3.2 \pm 0.5 | 0.4 \pm 0.7 | 0.13 |
| 7 | 1 | 2 | 13.0 \pm 0.5 | 11.6 \pm 0.6 | 1.5 \pm 0.8 | 0.13 |
| | | | $\Sigma I = 1058.4$ | $\Sigma I = 1058.4$ | $\Sigma \Delta I = 0.0$ | $\langle \Delta I/I \rangle = 0.064$ |

The two data sets "0-2ms" (excited) and "ref" (static) are scaled so that the sum of intensities is the same. The diffraction intensities change on average by 6.4%. Error estimates are derived from the residual of the peak fit, not from photon statistics.

The ground state data set was scaled to the M state data set so the sum of all the peak intensities has the same value.

11 of the 19 measured powder rings contain two structure factors, the ring (43) even three, because it is very close to (60), so the experimental changes cannot be unambiguously assigned to individual structure factors. A commonly used approach is to split the observed change in the same ratio as the ground state structure factors [Plöhn & Büldt 1986]. These structure factors are not available from X-ray powder diffraction, so the structure factors from electron diffraction [Henderson *et al.* 1986] are used instead to calculate the ratio. The phases for the calculation of the Fourier map are also taken from electron microscopy. Electron and X-ray scattering densities are not strictly equivalent, because the electron scattering arises from the electrostatic potential and the X-ray

scattering from the electron density. But at low resolution the approximation that the densities are identical is good.

The density maps were calculated by the CCP4 software *fft*, *extend* and *pluto*.

Results

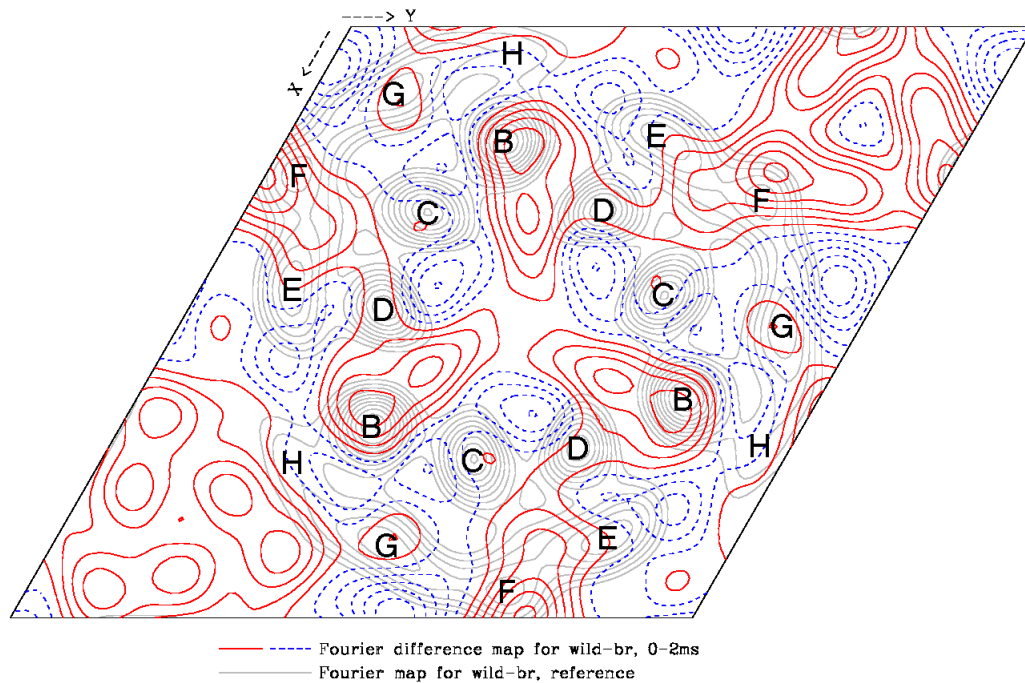


Figure 55: Difference electron density map for the M state of wild-type bR

This image shows projected electron density in the membrane plane. The underlying gray map represents the static structure of the bR trimer. In the regions contoured by red solid lines the density increases ($0, +0.5\sigma, \dots +2.5\sigma$); blue dashed lines indicate decrease ($-0.5\sigma, -1\sigma, \dots -2.5\sigma$). The difference map represents an average from 0 to 2 ms after flash excitation. The resolution is 7 Å (contour plot by N_PLUTO 3.4).

The 2-D electron difference map shows its strongest feature with an amplitude of $+2.5\sigma$ at the outside of the F helix. The next strongest feature is at the B helix. If those peaks are interpreted as arising from displacement of the helices, the displacements would be of 2.7 Å and 2.0 Å, respectively. At 7-Å resolution no trace of the retinal can be seen. The G helix, where the retinal is bound to the protein, does not show significant features. This

has to be compared with earlier maps of the long-lived M state of the Asp96Asn bR mutant [Koch *et al.* 1991] [Subramaniam *et al.* 1993]. These show two positive peaks at the F and the G helix.

6 Discussion

6.1 Instrumentation

This thesis shows that it is technologically feasible to perform Laue diffraction experiments of photosensitive macromolecules down to the 100-ps resolution limit of a third generation synchrotron.

6.2 Experiments on Photosensitive Proteins

6.2.1 Myoglobin

The transient absorption measurements on myoglobin crystals show that photolysis is achievable using non-destructive 100 fs optical excitation.

The experiments performed on myoglobin show that sub-nanosecond Laue diffraction works in principle. There is no clear indication for a "docking site" the CO molecule takes up after photolysis. According to Philip Anfinrud [Lim *et al.* 1997], the CO should be oriented parallel to the *heme* plane. It should take up this site within less than 1 ps and stay there for 200 ns. A possible explanation is that the potential minimum of the docking site could be too flat, to localize the CO at room temperature. However, at low temperatures it would take up a well-defined site, which has been observed by cryogenic crystallography [Schlichting *et al.* 1994] [Teng *et al.* 1994]. A broad distribution of the CO would result in a low amplitude in the difference map that can be lost in the noise floor.

The weakness of the experiment is the low pulse energy of the femtosecond laser. The successful 10-ns time-resolved Laue experiments in 1995 were done with a much more powerful Nd:YAG-dye laser, which could deliver up to 50 mJ per pulse. At the sample 10 mJ where focused to a spot of 1 mm diameter. So the precision of alignment required was less critical. Lack of fine control of the focal point position and size might be an explanation for the failure of the first experiment with the fs laser. The alignment cannot be done with the full laser beam the sample receives because it would destroy the pinhole. So the laser beam has to be attenuated a position far from the sample where it is

not focused. If that attenuator slightly deviates the beam, the focus of the full beam is off the sample position. Already an offset of 100 μm compromises the photolysis degree of the sample. At an excitation level of 10 %, a CO molecule shows up only as 1.4 electrons in the electron density. Such a signal level is close to that of a hydrogen atom, which is normally neglected in protein crystallography.

Another conclusion is that femtosecond laser pulses are not more damaging to myoglobin crystals than nanosecond laser pulses at comparable levels of pulse energy per surface, although their power density is 100000 times higher and their electrical field 300 times higher. This points forward to applications of the next generation synchrotron radiation sources, the hard X-ray free-electron laser, which is expected to produce 100-fs X-ray pulses. The stability of the crystals against laser excitation also makes it possible to use the narrow bandwidth approach for Laue data collection, using a single-line undulator. This requires a higher number of X-ray exposures in exchange for recording a smaller number of reflection per image with improved signal to background.

6.2.2 Photoactive Yellow Protein

With nanosecond laser excitation, non-destructive, reversible excitation to a degree of 15% could be achieved. Photo-isomerization of the chromophore could be seen completed after 1 ns, although there might be still open questions about the precise geometry of the chromophore. The amplitude of the difference peaks in the electron density map is only of the order of 2 electrons, due to the low extent of excitation and the low atomic number of the atoms involved.

Why the experiments with femtosecond laser excitation failed is still an open question. These experiments were technically more difficult, because of the lower pulse energy of the laser system and the higher precision required for the laser focusing and timing. Also, it has not been proven yet by optical spectroscopy that 400 nm is a suitable wavelength for exciting PYP crystals efficiently.

When the electron difference map of the 1-ns time point obtained by Laue diffraction is compared with the earlier millisecond time-resolved data (Figure 9, p.16), it is striking that the changes are smaller and more localized to the chromophore. This is consistent with the expectation that after the photocycle is triggered by an ultrafast isomerization

the protein takes microseconds to millisecond to react to this changed conformation and

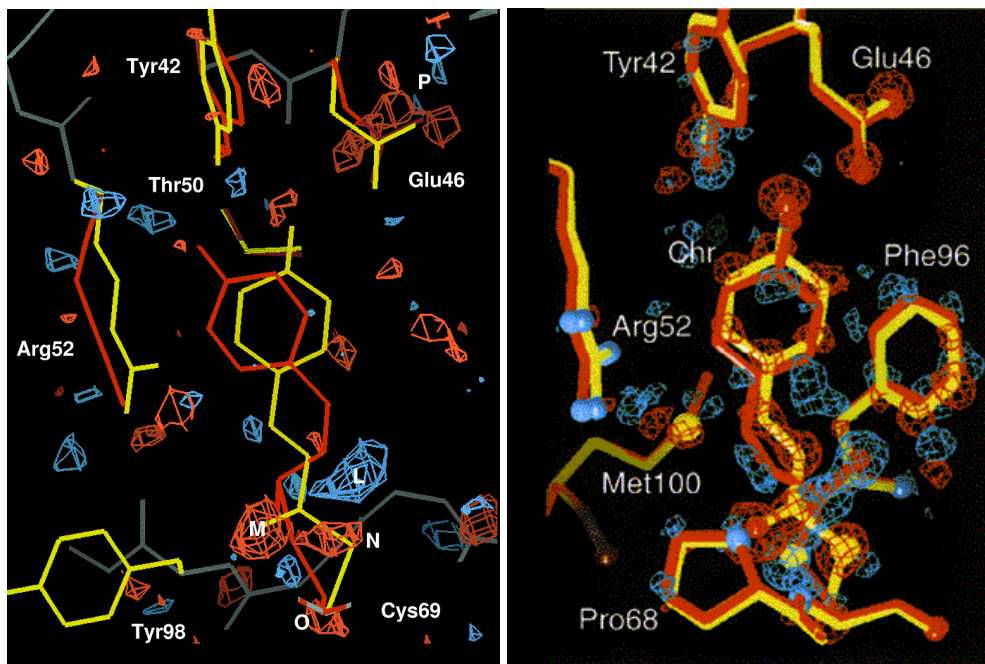


Figure 56: Laue and cryo-trapped X-ray structure of a PYP photocycle intermediate

Left: 281 K, 1-ns time delay, pulsed Laue diffraction, ESRF, 1996 (PDB entry 2PYR) [Perman *et al.* 1998], Right: cryo-trapped light-activated state at 170 K, monochromatic data collection, Stanford Synchrotron Radiation Lab, 1997 (PDB entry 3PYR) [Genick *et al.* 1998]. The photocycle intermediate (orange) is superimposed to the ground state structure (yellow) in both images. Electron density differences of the intermediate relative to the ground state are in red (negative) and blue (positive) at 2.6σ (left) and 4σ (right).

enter its signaling state.

The 1-ns difference map can be compared with a low-temperature difference map of a cryo-trapped photocycle intermediate obtained by Ulrich Genick one year later [Genick *et al.* 1998] (Figure 56). He exposed a frozen PYP crystal was to bright blue light, while collecting monochromatic data at a synchrotron.

Although the Laue map show less features, its strong features are seen in the monochromatic map as well. Both maps show a negative peak on the carbonyl-oxygen of

the thioester bond accompanied by a positive peak on the opposite side of the carbon chain and a negative peak on the sulfur atom of the thioester linkage.

However, the model of the I_2 state Ben Perman built based on the Laue data [Perman *et al.* 1998] differs significantly from Genick's model based on monochromatic data. In Perman's model the aromatic ring of the chromophore performs a 180° rotation about the photo-isomerizable C-C double bond. The carbonyl group of the thioester linkage rotates only by 90° to a position stabilized by a hydrogen-bond with the amide group of cysteine-69. He came to the conclusion that the carbonyl oxygen cannot rotate 180° , as the positive density peak would suggest, because of energetic penalties due to steric hindrance between the oxygen and the hydrogen atoms of the aromatic ring. In Genick's model, a part of the chromophore rotates about the photo-isomerizable C-C double bond, but the aromatic ring stays more or less in place. The rotation around the double bond is not 180° as one would expect for an isomerization reaction, but only 100° . Thus the chromophore is in a "chemically forbidden" conformation, which a free molecule without external constraints could not maintain. In his model, the carbonyl group of the thioester linkage is nearly in the plane of the chromophore after rotating by 166° .

One would expect that the cryo-trapped intermediate represents an early photocycle intermediate, because the primary photochemical reaction can still take place at low temperature, but that the protein is too rigid to perform the following series of relaxations that lead to the other photocycle states. On the other hand it can be questioned that Genick's structure represents the I_1 intermediate, because the absorption spectrum of light-activated PYP at 170 K (PYP_{BL} state) differs significantly from the I_1 spectrum [Imamoto *et al.* 1996]. Its absorption maximum is blue shifted with respect to the ground state, whereas the I_1 state has got a red-shifted absorption band (see Figure 8, p.15). The intermediates earlier than I_1 have got red-shifted absorption bands as well.

It is clear that the monochromatic map shows more details because of the higher resolution (0.85 \AA), compared to the Laue map (1.6 \AA). A weak point in the Laue based model might be that, due to the limited quantity of experimental, data chemical constraints have been overrated during the refinement, for example the planarity of the C-C double bond. The absorption of a photon introduces 2 eV of excess energy into the

molecule. This energy has to be stored somewhere to drive the PYP to the rest of its photocycle.

6.2.3 Bacteriorhodopsin

The increased time resolution at the ESRF has made it possible for the first time to study wild-type bacteriorhodopsin at physiological temperatures. Earlier diffraction studies have given M state data with comparable or higher resolution. However, those studies either used mutant-bR with a slower photocycle, slowed down the photocycle by chemical treatment with guanidinium hydrochloride at high pH, or frozen, cryo-trapped samples. The proof still had to be supplied that these difference maps do not show artifacts arising from the sample treatment, or artificial intermediates which are not part of the natural photocycle. It had to be proven that they indeed show structural dynamics, which are relevant for the function of the wild-type protein.

Although high-resolution X-ray structures of photocycle intermediates K, L and M are published in the meanwhile [Edman *et al.* 1999] [Luecke *et al.* 1999] [Sass *et al.* 2000], these are trapped intermediates. It will be still necessary to conduct real-time experiments at room temperature.

7 Outlook

7.1 Future Experiments

The kinetic studies on bacteriorhodopsin, especially on crystals, will be continued as part of international collaboration funded by the *Biotechnology* program of the European Commission. The EU project *Structural dynamics on ion pumps* involves the laboratories of Ehud Landau in Basel, Dieter Oesterhelt in Martinsried, Georg Büldt in Jülich and Janos Hajdu in Uppsala. As part of this project I have received a two-year grant to continue my work at the ESRF ID9 beamline. The future work at ID9 station will focus on fast kinetic studies of the bR photocycle, whereas freeze-trapping studies on intermediates can be carried out at other synchrotron beamlines as well.

7.2 X-ray Free Electron Lasers

The next generation of synchrotron radiation sources will probably be based on linear accelerators rather than circular synchrotrons. Such projects are under consideration at the DESY site in Hamburg [Åberg *et al.* 1997] and the SLAC site in Stanford, California for year 2004 [Cornacchia *et al.* 1998].

Such sources would deliver a pulsed photon flux comparable to or one order of magnitude higher than a wiggler at the ESRF in single bunch mode, 10^{12} - 10^{13} photons per pulse. The time resolution would be improved by 3 orders of magnitude from 100 ps to 100 fs. Thus structural dynamics at any chemically-relevant time scale could be studied, starting with the photocycle primary events such as ultra-fast photo-isomerization or photo-dissociation. Such an X-ray source would be quasi-monochromatic with a bandwidth of 10^{-3} at a wavelength of 1 Å or 1.5 Å. This would eliminate many problematic aspects of the Laue technique caused by the large bandwidth such as harmonic overlaps, the need for wavelength normalization, crowded diffraction patterns and high background. With an X-FEL source an experiment would resemble monochromatic data collection, where a large number of images are recorded with a minimal number of reflections per image, rotating the sample in small angular steps. A

data set would be a series of quasi-monochromatic still images with the necessary rotational spacing determined by the source bandwidth and sample mosaicity.

An experimental facility will consist of very long undulators grouped at the end of a multi-GeV linac with switchyard of kicker magnets to distribute the accelerated electron packets to the individual beamlines. This design will greatly simplify the design for a time-resolved beamline. Because individual electron bunches can be injected on demand into an end-station of choice, there will not be any need for high-performance mechanical X-ray shutters with sophisticated synchronization electronics. The tight collimation, e.g. 0.1 mm at 100 m distance, and the natural monochromaticity might even make X-ray optics, such as focussing mirrors and monochromators, superfluous. With the flexible packet switching scheme and user-selectable time-structure, scheduling problems, such as waiting for months for a few days of single-bunch beam time at the ESRF, will also be a problem of the past.

8 Acknowledgements

This work would not have been possible without **Michael Wulff**, who invested ten years in the construction and instrumentation of a unique facility for time-resolved X-ray diffraction, the ID9 beamline of the ESRF. Thanks to his enthusiasm he established fruitful collaborations, which lead to the successful projects, the results of which are presented here.

I have to thank **Georg Büldt** for supervising this of this thesis and his continuous support. I was able to my thesis thanks to a two-year grant he allocate to me from the EU project *Structural dynamics of ion pumps*.

Philip Anfinrud played a leading role in the construction of the femtosecond microspectrophotometer, spending more than two months at the ESRF in summer 1997. He also performed the first measurement on a MbCO crystal with this instrument and was a key player in the 100 ps experiments on myoglobin and PYP. Philip Anfinrud is not only a skilled experimentalist and very knowledgeable, he also is a gifted teacher and takes time to explain thing on a basic, didactical level. So, within the two months I spent with him, I learned more about lasers, spectroscopy and electronics than in four years at the university.

I am greatly indebted to **Janos Hajdu** for his help with the microspectrophotometer. He came from Oxford to the ESRF, to demonstrate his microspectrophotometer, and lent it to me for two weeks for an experiment on bR purple membrane.

I have to thank **Keith Moffat** for allowing me to make use of the prototype X-ray chopper for experiments on Bacteriorhodopsin.

Michel Roth generously allocated much of the equipment used for the time-resolved experiments, bought by the IBS Grenoble, as a loan to the ID9 beamline. This includes

the nanosecond Nd:YAG / dye laser system with its accessories, power meter, optical fiber and cleaving tool and the Huber two-circle diffractometer.

Richard Neutze assisted at the stroboscopic experiments on purple membrane in February and August 1996.

Thanks to **Christian Rischel** I got access to a powerful femtosecond laser system at the *Laboratoire d'Optique Appliqué* in Paris to do damage threshold studies on myoglobin crystals.

9 Appendix

9.1 Calorimetric Power Measurements

For a beamline used for flux-limited experiments it is important to make sure that the X-ray optical components are optimized for transmission and to track down eventual losses. The power of an insertion device and its spectral and angular distribution can be calculated accurately from its magnetic field, period, length and beam current. The comparison with experimental values gives valuable information about the overall transmission of the beamline and allows estimation of the number of photons per pulse available for single pulse Laue experiments.

The measurement is performed by sending the focused white beam in the experimental hutch into a copper block (Figure 57), which fully absorbs it. Then the temperature rise of the absorber is measured as a function of time.

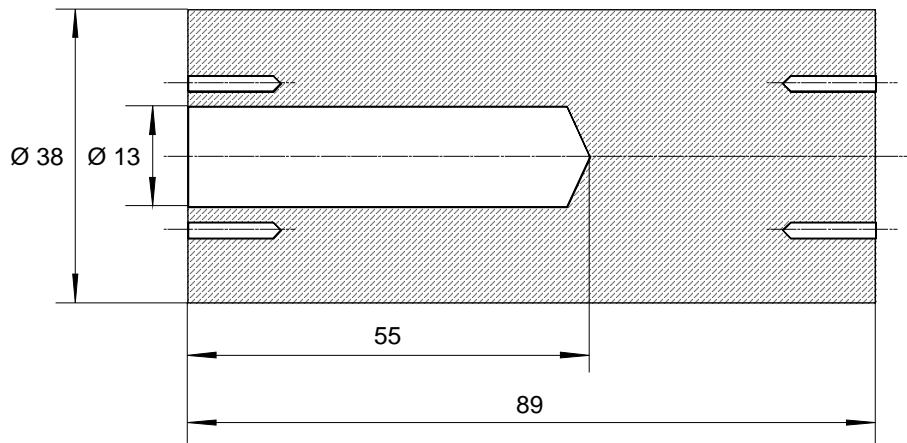


Figure 57: Copper block used as X-ray absorber for power measurements

Mass $m = 837.0$ g, specific heat 0.385 J/gK, heat capacity 322 J/K

From the known mass, specific heat and heat capacity, the total power can be calculated. Ideally, the absorber should be thermally isolated. In this case, it was mounted in air on a thin stainless steel pin to minimize thermal conduction losses.

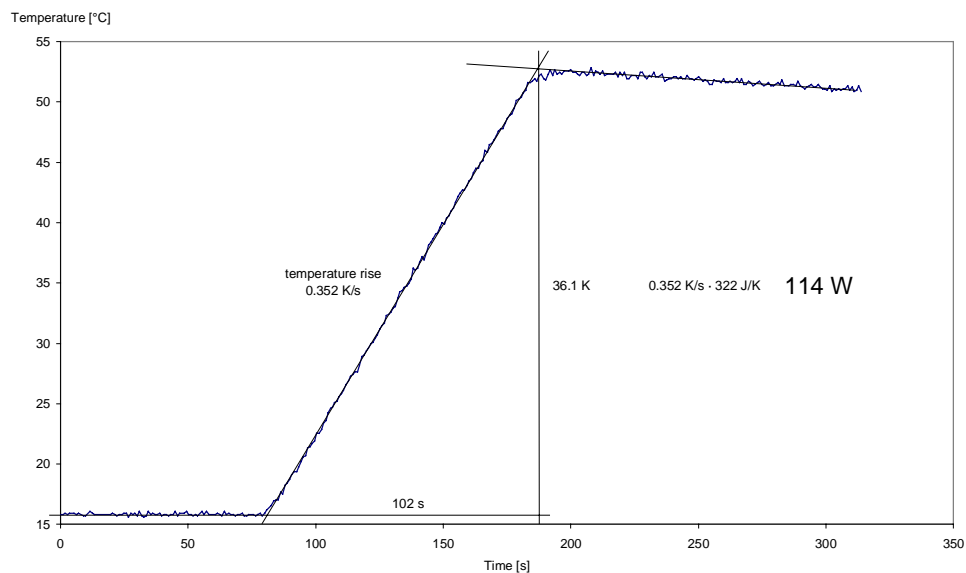


Figure 58: Power measurement for the Wiggler-70

Insertion device gap 20.2 mm, beam current 57.5 mA, aperture of primary slits 20 mm horizontal, 3 mm vertical, 18 Aug. 1996 11:10. The measure power corresponds to 199 W at 100 mA beam current.

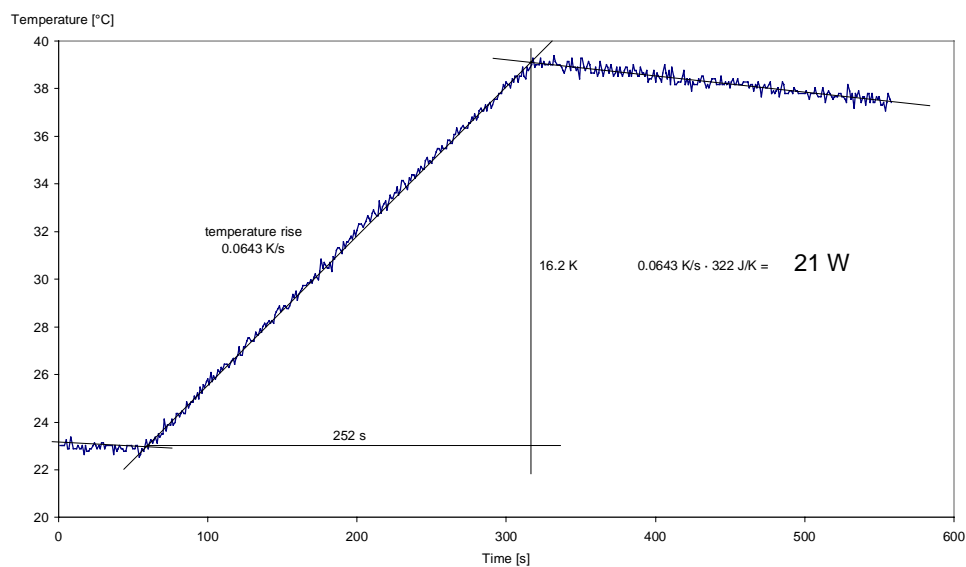


Figure 59: Power measurement for the Undulator-26

Insertion device gap 17.0 mm, beam current 54.8 mA, 17 Aug 1996, 23:45. The measure power corresponds to 37 W at 100 mA beam current.

9.2 Glossary

Bacteriorhodopsin

A rhodopsin-like pigment found in the microorganism *halobacterium salinarium*. (Greek *bacterion* = rod, rod-shaped microorganism, *rhodos* = rose, *opsis* = sight)

Geminate recombination

Geminate recombination refers to high probability for a photo-deligated CO molecule to return to its original iron binding site rather than escape.

Myoglobin

Red, globular shaped protein found in muscles storing oxygen, analog to hemoglobin in the blood (Greek *myon* = muscle, from *mys* = mouse, latin *globus* = ball)

Touschek Effect

The Touschek Effect limits the lifetime and current of the storage ring filling in single bunch mode. The limitation at the ESRF is 6-hour lifetime with 15-mA ring current.

Normally at the ESRF the beam lifetime is limited by collision with rest gas atoms. The current decay is then exponential, $I = I_0 \cdot e^{-t/\tau}$, where the lifetime τ is in the order of 50 hours. In single bunch mode, where all the charge, which is normally distributed over 664 bunches, is concentrated in one bunch, intra-bunch scattering of the electrons becomes the dominant loss process. Inside a bunch, the individual electrons tend to oscillate about the bunch center in the horizontal plane in the transverse and longitudinal directions because of a positive feedback between the acceleration gradient, electron energy and orbit radius. At high density, electrons will be scattered into the vertical plane where acceptance of the storage ring is much smaller and thus will be lost. How this effect depends on the beam parameters is expressed by the following formula:

$$\tau_p = E^2 (\delta p/p)^3 \sigma_x \sigma_y \sigma_z / I$$

where τ_p is the life-time, E the electron energy, $\delta p/p$ the energy bandwidth $\sigma_x \sigma_y \sigma_z$ the packet size and I the ring current.

Undulator

An undulator is a permanent magnet structure installed in a straight section of the electron storage ring, parallel to the electron beam. The electrons pass through an alternating transverse magnetic field forcing them on a sinusoidal undulated trajectory. Thus, a small fraction of their kinetic energy is converted into X-rays, emitted strongly collimated in forward direction. In contrast to a wiggler, the angular deviation of the electron beam for the straight line is small compared to the collimation angle of the X-rays. The emitted X-ray spectrum is spiky and shows peaks a regular uniformly spaced in energy, called *harmonics*, with high spectral brilliance.

Wiggler

A wiggler is an X-ray source, like the undulator, a permanent magnet structure, forcing the electron beam into a sinusoidal, wiggled trajectory. However, in contrast to the undulator the deviation of the electron beam from the forward direction is larger than the collimation angle of the emitted X-rays. The emitted X-rays spectrum is broad and smooth, but may have a slight periodic modulation of a few percent of the intensity.

9.3 List of publications

1. Michael Wulff, Thomas Ursby, Dominique Bourgeois, Friedrich Schotte, Federico Zontone & Maren Lorenzen, *New opportunities for time resolved x-ray scattering at the ESRF*. Journal de Chimie Physique, 1996. 93: p. 1915-1937.
2. Michael Wulff, Friedrich Schotte, Graham Naylor, Dominique Bourgeois, Keith Moffat & Gerard Mourou, *Time-resolved structures of macromolecules at the ESRF: single-pulse Laue diffraction, stroboscopic data collection and femtosecond flash photolysis*. Nuclear Instruments and Methods in Physics Research A, 1997. 398: p. 69-84.
3. Benjamin Perman, Vukica Srajer, Zhong Ren, Tsu-Yi Teng, Claude Pradervand, Thomas Ursby, Dominique Bourgeois, Friedrich Schotte, Michael Wulff, Remco Kort, Klaas Hellingwerf & Keith Moffat, *Energy transduction on the nanosecond time scale: early structural events in a xanthopsin photocycle*. Science, 1998, 279(5358): p. 1946-50.
4. Y. P. Nieh, J. Raftery, S. Weisgerber, J. Habash, Friedrich Schotte, Thomas Ursby, Michael Wulff, Alfons Hädener, J. W. Campbell, Hao Quan, M. M. Harding & John R. Helliwell, *Accurate and highly complete synchrotron protein Laue data using the ESRF CCD and the Daresbury software*. Journal of Synchrotron Radiation, 1999, 6: p. 995-1006.
5. Vukica Srajer, Sean Crosson, Marius Schmidt, Jason Key, Friedrich Schotte, Spencer Anderson, Benjamin Perman, Zhong Ren, Tsu-Yi Teng, Dominique Bourgeois, Michael Wulff & Keith Moffat, *Extraction of accurate structure factors amplitudes from Laue data: wavelength normalisation with wiggler and undulator X-ray sources*, Journal of Synchrotron Radiation, Volume 7, Part 4, p. 236-244.
6. Friedrich Schotte, Simone Techert, Philip Anfinrud, Vukica Srajer, Keith Moffat & Michael Wulff, *Recent Advances in the Generation of Pulsed Synchrotron Radiation Suitable for Picosecond Time-Resolved X-ray Studies*, to appear in: Handbook of Synchrotron Radiation, Vol. 5, 2000, edited by Dennis Mills.

7. Simone Techert, Friedrich Schotte & Michael Wulff, *Picosecond X-ray Diffraction from transient structural changes in organic solids*, manuscript to be submitted to Journal of Chemical Physics.

9.4 Conference Contributions

1. ESRF Users Meeting *Science at the ESRF*, Workshop *Challenging Biological Structures*, Grenoble, 18-20 Nov. 1996, *Stroboscopic determination of the photo-excited states in Bacteriorhodopsin with 100 μ s time-resolution*
2. 17th European crystallographic meeting, Lisbon, 24-28 Aug. 1997, *Stroboscopic X-ray diffraction studies of photo-excited transient states of bacteriorhodopsin*, Conference proceedings, MS4.1-4
3. Workshop on Electronic and structural dynamics of light-induced processes in bacteriorhodopsin, Université de Lausanne, 9-10 Apr. 1999, *Stroboscopic X-ray diffraction on Purple Membrane*, Programme abstracts, p. 10

10 Index

- Anfinrud, Philip, 57
- Bacteriorhodopsin: function, 18
- bearing, magnetic, 40
- bunches, electron, 24
- calibration, XRII, 48
- CCD camera: description, 46
- chopper: X-ray, 39
- cinnamic acid, hydroxy-, 13
- continuum generation, 54
- cryo-trapping: myoglobin, 9; PYP, 15
- dark current: CCD, 46
- distortion, XRII, 48
- docking site: CO in myoglobin, 9
- Dominique Bourgeois: X-ray chopper, 39
- Ectothiorhodospira halophila, 12
- excitation: bacteriorhodopsin, 76; myoglobin, 67; PYP, 72
- FIT2D, 48
- flash lamp: millisecond, 76
- flash lamp, microsecond: bacteriorhodopsin, 77
- Forschungszentrum Jülich: X-ray chopper, 39
- gain factor: XRII, 47
- grid image, XRII, 48
- halobacterium halobium*, 17
- halobacterium salinarium*, 17
- Halorhodospira halophila, 12
- heatload: X-ray chopper, 43
- heatload shutter, 33
- hemoglobin: vs. myoglobin, 7
- High-pressure experiments at ID9, 26
- Institut-Laue-Langevin: Neutron chopper, 39
- Janos Hajdu: Microspectrophotometer, 51
- laser, dye: PYP, 72
- mica: sample carriers, 75
- Michael Wulff: ID9 beamline, 26
- microscope objectives, reflecting, 52
- neutron chopper, 39
- NSLS: Laue diffraction, 15
- oxygen storage, myoglobin, 7
- p, 14
- phase shifter, 60
- phase-locking: X-ray chopper, 43
- photocycle: Bacteriorhodopsin, 19; PYP, 14
- photo-isomerization: Bacteriorhodopsin, 19; PYP, 14
- phototaxis: PYP, 13
- point-spread function: XRII, 47
- purple membrane, 18

quantum efficiency: CCD, 46; XRII, 47

reflective microscope: reflective, 57

reflectivity: X-ray mirror, 35

regenerative amplifier: timing, 61

Rhodobacter sphaeroides, 13

rhodopsin: vs. bacteriorhodopsin, 17

Schildkamp, Wilfried: X-ray chopper, 38

Schwartzschild objective. *See* microscope
objective, reflective

Schwarzschild objective, 52

shielding: anti-magnetic, 47

single crystal: spectrometry, 54

single pulse: separation, 38

spectrograph, 57

spectrometer: femtosecond, 54

strontium glass, XRII calibration, 48

Synchro-Lock, 60

synchrotron radiation: introduction, 21; time
structure, 23

timing: software, 61; X-ray to laser, 38, 59

uniformity, XRII, 48

University of Chicago: X-ray chopper, 38, 39

Xantopsin, 12

X-ray chopper: Forschungszentrum Jülich, 39;
overview, 37; University of Chicago, 38

X-ray image intensifier: description, 45

Zeiss: X-ray mirror, 34

11 References

- Åberg, T., B. Adams, H. Bartunik & H. Dosch T. Brückel, R. Feidenhans'l, J. Feldhaus, R. Frahm, R. Gehrke, E. Gerdau, W. Graeff, G. Grübel, P. Gürtler, J. Härtwig, R. L. Johnson, A. Kaprolat, M. Koch, O. Leupold, P.A. Lindgård, G. Materlik, J. Neuefeind, D. Norman, J. Pflüger, A. Schenzle, G. Schmahl, W. Schül, *A Superbrilliant X-ray Laser Facility*, in *Conceptual Design Report of a 500 GeV $e+e-$ Linear Collider with Integrated X-ray Laser Facility*, G. Materlik, Editor. 1997, DESY: Hamburg.
- Anfinrud, Philip A., *Ligand migration in a protein from femtosecond to microseconds. Time-resolved mid-IR spectroscopy of photolyzed carbon monoxy myoglobin*. [in preparation], 2000.
- Belrhali, H., P. Nollert, A. Royant, C. Menzel, J. P. Rosenbusch, E. M. Landau & E. Pebay-Peyroula, *Protein, lipid and water organization in bacteriorhodopsin crystals: a molecular view of the purple membrane at 1.9 Å resolution*. Structure Fold Des, 1999. **7**(8): p. 909-17.
- Blood, William R., *Motorola MECL System Design Handbook*, . 1988. p. 4, 38-39.
- Borgstahl, Gloria E., D.R. Williams & Elizabeth D. Getzoff, *1.4 Å structure of photoactive yellow protein, a cytosolic photoreceptor: unusual fold, active site, and chromophore*. Biochemistry, 1995. **34**(19): p. 6278-87.
- Bourgeois, Dominique, Jean-Pierre Moy, S. Olof Svensson & Ake Kvik, *The Point-Spread function of X-ray Image-Intensifier/CCD-Camera and Imaging-Plate Systems in Crystallography: Assessment and Consequences for the Dynamic Range*. Journal of Applied Crystallography, 1994. **27**: p. 868-877.
- Bourgeois, Dominique, Thomas Ursby, Michael Wulff, Claude Pradervand, Vukica Srajer, Alan LeGrand, Wilfried Schildkamp, Silvain Labouré, Christophe Rubin, Tsu-Yi Teng, Michel Roth & Keith Moffat, *Feasibility and Realization of Single-Pulse Laue Diffraction on Macromolecular Crystals*. Journal of Synchrotron Radiation, 1996. **3**: p. 65-74.
- Chizhov, I., D. S. Chernavskii, M. Engelhard, K.-H. Mueller, B. V. Zubov & B. Hess, *Spectrally silent transitions in the bacteriorhodopsin photocycle*. Biophysical Journal, 1996. **71**: p. 2329-2345.
- Coherent, *Synchro-Lock Operators Manual, Version 1.1*, . 1996, Coherent.
- Cornacchia, M., J. Arthur, K. Bane & G. Bowden V. Bharadwaj, R. Boyce, R. Carr, J. Clendenin, W. Corbett, T. Cremer, P. Emma, A. Fassio, C. Field, A. Fisher, R. Gould, R. Hettel, J. Humphrey, K. Ko, T. Kotseroglou, Z. Li, D. Martin, B. McSwain, R. Miller, C. Ng, H.-D. Nuhn, D. Palmer, M. Pietryka, S. Rokni, R. Rulan, *Linac Coherent Light Source (LCLS) Design Study Report*, . 1998, Stanford Linear Accelerator Center, Stanford University: Stanford.

- Ebrey, Thomas G., *Light Energy Transduction in Bacteriorhodopsin*, in *Thermodynamics of Surface Cell Receptors*, M. Jackson, Editor. 1992, CRC Press.
- Edman, Karl, Peter Nollert, Antoine Royant, Hassan Belrhali, Eva Pebay-Peyroula, Janos Hajdu, Richard Neutze & Ehud M. Landau, *High-resolution X-ray structure of an early intermediate in the bacteriorhodopsin photocycle*. *Nature*, 1999. **401**(6755): p. 822-826.
- Genick, U. K., G. E. Borgstahl, K. Ng, Z. Ren, C. Pradervand, P. M. Burke, V. Srajer, T. Y. Teng, W. Schildkamp, D. E. McRee, K. Moffat & E. D. Getzoff, *Structure of a protein photocycle intermediate by millisecond time- resolved crystallography*. *Science*, 1997. **275**(5305): p. 1471-5.
- Genick, Ulrich K., S. Michael Soltis, Peter Kuhn, Ilona L. Canestrelli & Elizabeth D. Getzoff, *Structure at 0.85 Å resolution of an early protein photocycle intermediate*. *Nature*, 1998. **392**: p. 206-209.
- Hadfield, Andrea & Janos Hajdu, *A fast and portable microspectrophotometer for protein crystallography*. *Journal of Applied Crystallography*, 1993. **26**: p. 839-842.
- Halbach, Klaus, *Physical and optical properties of rare earth cobalt magnets*. *Nuclear Instruments and Methods*, 1981. **187**: p. 109-117.
- Henderson, Richard, J.M. Baldwin, K.H. Downing, J. Leault & Fritz Zemlin, *Structure of Purple membrane from Halobacterium halobium: recording, Measurement and Evaluation of Electron Micrographs at 3.5 Å Resolution*. *Ultramicroscopy*, 1986. **19**: p. 127-148.
- Hoff, W. D., I. H. van Stokkum, H. J. van Ramesdonk, M. E. van Brederode, A. M. Brouwer, J. C. Fitch, T. E. Meyer, R. van Grondelle & K. J. Hellingwerf, *Measurement and global analysis of the absorbance changes in the photocycle of the photoactive yellow protein from Ectothiorhodospira halophila*. *Biophys J*, 1994. **67**(4): p. 1691-705.
- Imamoto, Y., M. Kataoka & F. Tokunaga, *Photoreaction cycle of photoactive yellow protein from Ectothiorhodospira halophila studied by low-temperature spectroscopy*. *Biochemistry*, 1996. **35**(45): p. 14047-53.
- Koch, Ernst-Eckehard, ed. *Handbook of Synchrotron Radiation*. . Vol. I. 1983, North Holland: Amsterdam, New York & Oxford. 27.
- Koch, M. H., N. A. Dencher, D. Oesterhelt, H. J. Plohn, G. Rapp & G. Buldt, *Time-resolved X-ray diffraction study of structural changes associated with the photocycle of bacteriorhodopsin*. *Embo J*, 1991. **10**(3): p. 521-6.
- Kort, Remco, *Studies of a bacterial photosensor*, in *BioCentrum*. 1999, University of Amsterdam: Amsterdam. p. 113.
- Kort, Remco, W. D. Hoff, M. Van West, A. R. Kroon, S. M. Hoffer, K. H. Vlieg, W. Crieland, J. J. Van Beeumen & Klaas J. Hellingwerf, *The xantopsins: a new family of eubacterial blue-light photosensors*. *EMBO Journal*, 1996. **15**: p. 3209-18.

- Landau, Ehud M. & Jörg Rosenbusch, *Lipidic cubic phases: A novel concept for the crystallization of membrane proteins*. Proceedings of the National Academy of Science, USA, 1996. **93**: p. 14532-14535.
- LeGrand, Alan D., Wilfried Schildkamp & Basil Blank, *An Ultrafast Mechanical Shutter for X-rays*. Nuclear Instruments and Methods A, 1989. **275**: p. 422.
- Lim, Manho, Timothy A. Jackson & Philip A. Anfinrud, *Ultrafast rotation and trapping of carbon monoxide dissociated from myoglobin*. Nature Structural Biology, 1997. **4**(3).
- Luecke, Hartmut, Brigitte Schobert, Hans-Thomas Richter, Jean-Philippe Cartailier & Janos K. Lanyi, *Structural changes in bacteriorhodopsin during ion transport at 2 angstrom resolution*. Science, 1999. **286**(5438): p. 255-61.
- Meyer, T. E., *Isolation and characterization of soluble cytochromes, ferredoxins and other chromophoric proteins from the halophilic phototrophic bacterium Ectothiorhodospira halophila*. Biochim. Biophys. Acta, 1985. **1016**: p. 364-370.
- Michel, Nicolas, *Programming the Delay and Divider unit*, . 1996, ESRF.
- Mills, Dennis M., *Time-resolved studies*, in *Handbook of Synchrotron Radiation*, G.S. Brown and D.E. Moncton, Editors. 1983, North-Holland: Amsterdam, New York & Oxford.
- Moy, Jean-Pierre, *A 200 mm input field, 5-80 keV detector based on an X-ray image intensifier and CCD camera*. Nuclear Instruments & Methods in Physics Research A, 1994. **348**: p. 641-644.
- Oesterhelt, Dieter & Walter Stoeckenius, *Rhodopsin-like protein from the purple membrane of Halobacterium halobium*. Nature New Biology, 1971. **223**: p. 149-152.
- Pebay-Peyroula, Eva, G. Rummel, Jürg P. Rosenbusch & Ehud M. Landau, *X-ray Structure of Bacteriorhodopsin at 2.5 Angstroms from Microcrystals Grown in Lipidic Cubic Phases*. Science, 1997. **27**: p. 1676.
- Perman, Benjamin, Vukica Srajer, Zhong Ren, Tsu-Yi Teng, Claude Pradervand, Thomas Ursby, Dominique Bourgeois, Friedrich Schotte, Michael Wulff, Remco Kort, Klaas Hellingwerf & Keith Moffat, *Energy transduction on the nanosecond time scale: early structural events in a xanthopsin photocycle*. Science, 1998. **279**(5358): p. 1946-50.
- Plöhn, Hans-Jürgen & Georg Büldt, *The Determination of Label Positions in Membrane Proteins by Neutron and Anomalous X-ray Diffraction of Powder Samples*. Journal of Applied Crystallography, 1986. **19**: p. 255-261.
- Princeton-Instruments, *High Performance CCD Cameras*. 1994.
- Raymond, J.C. & W. R. Sistrom, *The isolation and preliminary characterization of a halophilic photosynthetic bacterium*. Arch. Microbiol., 1967. **59**: p. 255-268.
- Ren, Zhong & Keith Moffat, *Quantitative Analysis of Synchrotron Laue Diffraction Patterns in Macromolecular Crystallography*. Journal of Applied Crystallography, 1995. **28**: p. 461-481.

- Sass, Hans Jürgen, Joel Berendzen, Dirk Neff, Ralf Gessenich, P. Ormos & Georg Bueldt, *The M Intermediate Structure of Bacteriorhodopsin at 2.2 Å Resolution*. Nature, 2000. [**submitted, PDB entry 1CWQ**].
- Schertler, G. F., H. D. Bartunik, H. Michel & D. Oesterhelt, *Orthorhombic crystal form of bacteriorhodopsin nucleated on benzamidine diffracting to 3.6 Å resolution*. J Mol Biol, 1993. **234**(1): p. 156-64.
- Schlichting, Ilme, Joel Berendzen, George N. Phillips, Jr. & Robert M. Sweet, *Crystal structure of photolysed carbonmonoxy-myoglobin*. Nature, 1994. **371**(6500): p. 808-12.
- Sprenger, W. W., W. D. Hoff, J. P. Armitage & Klaas J. Hellingwerf, *The eubacterium Ectothiorhodospira is negatively phototactic, with a wavelength dependence that fits the absorption spectrum of the photoactive yellow protein*. Journal of Bacteriology, 1993(175): p. 3096-104.
- Springer, Barry L., Stephen G. Sligar, John S. Olson & Jr. George N. Phillips, *Mechanisms of Ligand Recognition in Myoglobin*. Chem. Rev., 1994. **94**: p. 600-714.
- Srajer, V., T. Teng, T. Ursby, C. Pradervand, Z. Ren, S. Adachi, W. Schildkamp, D. Bourgeois, M. Wulff & K. Moffat, *Photolysis of the carbon monoxide complex of myoglobin: nanosecond time-resolved crystallography*. Science, 1996. **274**(5293): p. 1726-9.
- Subramaniam, S., M. Gerstein, Dieter Oesterhelt & Richard Henderson, *Electron diffraction analysis of structural changes in the photocycle of bacteriorhodopsin*. Embo J, 1993. **12**(1): p. 1-8.
- Teng, Tsu-Yi, Vukica Srajer & Keith Moffat, *Photolysis-induced structural changes in single crystals of carbonmonoxy myoglobin at 40 K*. Nature Structural Biology, 1994. **1**(10): p. 701-5.
- Thiedemann, *Zeitaufgelöste optische Spektroskopie an Bacteriorhodopsin: Photozyklusintermediate, Einfluss von Wasser*, in *Fachbereich Physik*. 1994, Freie Universität Berlin: Berlin. p. 134.
- Ujj, L., S. Devanathan, T. E. Meyer, M. A. Cusanovich, G. Tollin & G. H. Atkinson, *New Photocycle Intermediates in the Photoactive Yellow Protein from Ectothiorhodospira halophila: Picosecond Transient Absorption Spectroscopy*. Biophysical Journal, 1998. **75**: p. 406-412.
- Ursby, Thomas & Dominique Bourgeois, *Improved Estimation of Structure-Factor Difference Amplitudes from Poorly Accurate Data*. Acta Crystallographica A, 1997. **53**(5): p. 564-575.
- Vitkup, D., G. A. Petsko & M. Karplus, *A comparison between molecular dynamics and X-ray results for dissociated CO in myoglobin*. Nat Struct Biol, 1997. **4**(3): p. 202-8.
- West, J. B. & H. A. Padmore, *Optical Engineering*, in *Handbook of Synchrotron Radiation*, G.V. Marr, Editor. 1983, North-Holland: Amsterdam, New York & Oxford.
- Woodruff, David C., *New shutter designs meet challenge of laser systems*. Laser Focus World, 1991. **September 1991**.

Wulff, Michael, *The Optimization of Mirror Focusing of Synchrotron X-ray Sources: a Test Case at the ESRF*. SPIE, 1992. **1739 High Flux Engineering**: p. 576-591.

Curriculum vitae

Surname: Schotte
First name: Friedrich
Born: 27 May 1968 in Köln
Parents: Dr. Klaus-Dieter Schotte, Professor for theoretical physics at the
Freie Universität Berlin
Dr. Ursula Schotte, Physicist, retired

School education

1974-78 Elementary school in Berlin-Zehlendorf
1978-87 Gymnasium in Berlin-Steglitz
1987 Abitur, grade 1.7 (good)

University education

1987-89 Study of Physics at the Technische Universität Berlin
1989 Vordiplom (intermediate examination), grade "good"
1989-94 Study of Physics
1994 Diploma of Physics, grade "good"
Subject of Diploma thesis: *Development of an evaluation method
for LIDAR data and control of a LIDAR instrument*
Supervisor: Prof. Ludger Wöste
Oct. 1994 - Jan 1995 Assistant at the Universität Frankfurt, group of Prof. Lüthi
Feb. 1995 - June 1995 Trainee at the ESRF, ID9 beamline
June 1995 - June 2000 Thesis student at the ESRF
Supervisor at the ESRF: Dr. Michael Wulff
Formal supervisor: Prof. Georg Büldt